NASA Technical Memorandum 88311

Computation of Transonic Separated Wing Flows Using an Euler/Navier-Stokes Zonal Approach

Ünver Kaynak, Terry L. Holst, and Brian J. Cantwell

July 1986

National Aeronautics and Space Administration

NASA Technical Memorandum 88311

Computation of Transonic Separated Wing Flows Using an Euler/Navier-Stokes Zonal Approach

Ünver Kaynak, Sterling Software, Palo Alto, California
Terry L. Holst, Ames Research Center, Moffett Field, California
Brian J. Cantwell, Stanford University, Stanford, California

July 1986

National Aeronautics and
Space Administration

Ames Research Center
Moffett Field, California 94035

Computation of Transonic Separated Wing Flows Using an Euler/Navier-Stokes Zonal Approach

by

Ünver Kaynak
Sterling Software, Palo Alto, CA

Terry L. Holst
NASA Ames Research Center, Moffett Field, CA

Brian J. Cantwell
Stanford University, Stanford, CA

A computer program called Transonic Navier Stokes (TNS) has been developed which solves the Euler/Navier-Stokes equations around wings using a zonal grid approach. In the present zonal scheme, the physical domain of interest is divided into several subdomains called "zones" and the governing equations are solved interactively. The advantages of the Zonal Grid approach are as follows: 1) the grid for any subdomain can be generated easily, 2) grids can be, in a sense, adapted to the solution, 3) different equation sets can be used in different zones, and 4) this approach allows for a convenient data base organization scheme. Using this code, separated flows on a NACA 0012 section wing and on the NASA Ames WING C have been computed. First, the effects of turbulence and artificial dissipation models incorporated into the code are assessed by comparing the TNS results with other CFD codes and experiments. Then a series of flow cases are described where data are available. The computed results, including cases with shock-induced separation, are in good agreement with experimental data. Finally, some "futüristic" cases are presented to demonstrate the abilities of the code for massively separated cases which do not have experimental data.

TABLE OF CONTENTS

CHAPTER 1

INTRODUCTION

1.1 Background

Ever since the introduction of the Navier-Stokes equations in the early 1800's by Navier [1] and Stokes [2], we have been confronted with a very challenging situation. Because of the nonlinear and complex nature of these equations, the number of closed form analytical solutions has been extremely limited. Hence, the Navier-Stokes equations were largely unused for several decades, and did not contribute to the early development of airplanes.

The first major breakthrough in the solution of these equations was introduced by Ludwig Prandtl [3] in 1904. Prandtl brilliantly reasoned that for high Reynolds number flows, viscous effects would be confined to a thin layer along a solid surface, called the "Boundary Layer." We owe much of our understanding of the viscous flow phenomenon to this concept. Although this region occupies only a small portion of a total flow field, all momentum, heat and mass transfer to or from the surface must take place through this layer. Outside the boundary layer, fluid behaves like an inviscid flow. This leads us to a very important conclusion that separate equation sets can be solved in separate domains. Therefore, aeronautical problems can be approached from different avenues; i.e., using different equation sets, provided that limitations are kept in proper perspective. The aforementioned "different equation sets" are subsets of the Navier-Stokes equations. If the viscous terms are neglected, the resulting equations describe the motion of an inviscid but nonlinear, compressible and rotational fluid: the so-called "Euler equations." If the rotationality is ignored, we get nonlinear, compressible and irrotational flow; i.e., the full potential equation which can support only weak shocks. Further simplification leads to Laplace's equation which describes an incompressible, inviscid, irrotational and steady flow.

Introduction of digital computers brought a great change to the aeronautical sciences. They opened new avenues and enabled researchers to tackle the problem of solving the above equation sets. With the advent of computers, a new discipline of aerodynamics was born, i.e., Computational Fluid Dynamics (CFD), and researchers attacked problems which were previously unsolvable. But it was soon realized that compromises had to be made because computer time and memory limit the range of physical and geometrical scales that can be resolved. The more complex the geometry, the less physics we can extract. In

terms of numerical techniques, the choice between a complicated set of equations with simple geometry and a sophisticated geometry with simpler equations had to be made.

Basically there are three compelling motivations for vigorously developing Computational Aerodynamics (Chapman [4]). The first one is to provide new technological capabilities which the wind tunnels cannot offer. For example, the Reynolds number associated with aircraft flight, the flowfield temperatures around atmospheric entry vehicles like the space shuttle, hot jet plumes, or store ejections cannot be easily simulated by wind-tunnels. A second compelling motivation concerns energy conservation. Wind tunnels consume large amounts of energy with increasing unit costs every year, whereas computers do not consume as much energy. The third motivation can be explained in terms of economics. Chapman [4] indicated that the net cost to conduct a given numerical simulation with a fixed algorithm has decreased ten times every eight years because computer speed has increased at a much greater rate than computer cost.

Developments of computational aerodynamics have been paced by computer memory and speed. Naturally, work started with the most simplified equation sets and configurations and has progressed to more sophisticated geometries with better approximation of the flow physics. Chapman [4] presents the historical progress of Computational Aerodynamics in four stages, each of which is a successively more refined approximation to the full Navier-Stokes equations. Stage I is the linearized inviscid approximation or Laplace's equation. Computational methods which solve this governing equation are called "Panel Methods" and have been very useful in the design process. The linearized inviscid approximation contains only 3 terms; whereas the full Navier-Stokes equations representing conservation of mass, momentum and energy contain altogether 60 partial-derivative terms when written out in three Cartesian coordinates. Panel methods provide realistic determinations of pressure distribution, of lift and side forces in attached subsonic and supersonic flow using small disturbance theory. For an extensive list of references and survey articles the reader is referred to [4],[5].

The second stage of approximation is called "nonlinear inviscid" and here only the viscous terms are neglected, but in its most complex form, 27 out of 60 partial derivative terms are retained from the full Navier-Stokes equations. The transonic small-disturbance equation, the full potential equation and the Euler equations fall into this category. Nonlinear inviscid computations for transonic flow are extensive design tools for the aircraft industry today. For more information please refer to [4].

The third and fourth stage of Computational Aerodynamics involve the Reynolds-averaged Navier-Stokes equations and the Large Eddy Simulation(LES)

respectively. The Reynolds-averaged Navier-Stokes equations are obtained by replacing the dependent variables in the original Navier-Stokes equations by the mean and fluctuating parts and then time-averaging the equations. This time interval must be long compared to the characteristic time of turbulent eddy fluctuations and short compared to the characteristic time of the, perhaps, unsteady main flow. The resulting equations describe the time-dependent flow field but are not capable of capturing fluctuating turbulent eddies of any length scale; i.e., all turbulent eddies must be modeled. In large eddy simulation, the small scale eddies are modeled while the large eddies are computed. Solving the full Navier-Stokes equations about a complex geometry at high Reynolds number without any averaging is yet beyond the reach of present day and the near future supercomputers. For this reason, the "Reynolds-averaged Navier-Stokes" equations in the "thin-layer" form are used in this project. Therefore, it is necessary to cite some of the significant steps taken in this relatively new area.

Early work started with the computation of laminar flow which is governed by the steady Navier-Stokes equations. Although a good survey on laminar flow research has been done by Peyret and Viviand [6], certain notable efforts are listed below: The shock wave laminar boundary layer interaction by Mac Cormack [7], the computation of laminar flow over a compression corner by Carter [8], and hypersonic flow over blunt bodies by Jain and Adimurty [9]; also, incompressible flow over bluff bodies and airfoils by Thompson et al. [10] and Hodge and Stone [11], and supersonic two-dimensional flow over a blunt body with impinging shock wave by Tannehill et al. [12]. In three-dimensional laminar flow simulation, we can mention the computation of the flow over an inclined body of revolution by Li [13], and the laminar flow over three-dimensional compression corners by Shang and Hankey [14] and Hung and Mac Cormack [15].

Since most aerodynamic flows encountered in actual flight conditions are turbulent, the Reynolds-averaged Navier-Stokes formulation draws much of the attention from engineers and scientists. Early turbulent flow simulations started with two-dimensional flows and include the shock wave/turbulent boundary layer interaction study by Wilcox [16] and Baldwin and MacCormack [17], and the high Reynolds number transonic flow computation over airfoils by Deiwert [18]. Some numerical computations were also carried out for supersonic flow over compression corners by Wilcox [19], Shang and Hankey [20], and Hung and MacCormack [21] and axisymmetric afterbody computations were carried out by Holst [22]. Some of the turbulent simulations yielded very interesting results which closely modeled the actual physical phenomena: For instance, the unsteady buffeting of a thick circular arc airfoil in transonic flow was simulated by Levy [23], the transonic drag polar and lift curve for a supercritical airfoil with buffeting forces were reported by Deiwert and Bailey [24], and the simulation of transonic aileron buzz was achieved by Steger and Bailey [25].

Three-dimensional solutions of turbulent flows with the Reynolds-averaged equations are relatively few. The first simulations were the flows around relatively simple geometries; for example the three-dimensional swept shock wave/turbulent boundary layer interaction by Hung and MacCormack [26], and the flow along a corner for both transitional and fully turbulent flow by Shang et al. [27]. Another notable work was the simulation of a separated flow over a hemisphere-cylinder body at an angle of attack by Pulliam and Steger [28]. In most of these simulations, the "thin-layer" approximation to the Reynolds-averaged Navier-Stokes equations devised by Baldwin and Lomax [29] has been utilized. Very recently, computation of more complex geometries involving more sophisticated flow physics has been attacked. Work in this area includes the transonic fuselage and forebody flows of Cosner [30], the hypersonic wing/fuselage interaction of Shang [31], the supersonic blunt-fin/wall interaction of Hung and Kordulla [32], the high-subsonic turret flow simulation of Purohit et al. [33], the transonic wing flow of Mansour [34], the transonic afterbody flows of Deiwert and Rothmund [35] and Deiwert et al. [36], the transonic wing flows of Agarwal and Deese [37], the transonic forward-fuselage flow of Chaussee et al. [38], and the high-subsonic delta wing and low supersonic, shuttle-like flows of Fujii and Kutler [39].

1.2 Motivation

In the previous section, the role of Computational Fluid Dynamics as a research and design tool in aeronautical sciences has been introduced. It was also stated that there emerged numerous pioneering works in computational Navier-Stokes technology. Some of the reasons for this movement are explained as follows: First, the computer hardware(memory and speed) have dramatically improved by the introduction of the so-called supercomputers such as the Cray 1, Cray XMP, CDC Cyber 205 [4]. Second, there is an increasing demand from the aircraft industry to utilize more realistic approximations in design problems. For instance, modern military aircraft must be able to fly in the transonic regime at high angles of attack with significant regions of separated flow, and the full Navier-Stokes equations are the proper model equations for this purpose. These reasons have given a tremendous impetus to viscous transonic flow research, especially focused on flow separation and shock/boundary-layer interaction. In an excellent survey about transonic Navier-Stokes technology, Mehta and Lomax [40] list the flow conditions for which the Navier-Stokes equations appear to be required: 1) Shock/boundary layer interaction with no separation, 2) shock-induced turbulent separation with immediate reattachment(shock-induced separation bubble), and 3) shock-induced separation without reattachment. The proper treatment of shock/boundary layer interaction, at least locally, necessitates the use of the Navier-Stokes equations [41]. There are primarily two motivations for understanding separated flows [40]. Since uncontrolled separation causes stall, controlling and minimizing the effects of separation are desirable.

Separation can also be used to improve aerodynamic performance; for instance, the rolled up vortex sheet from the sharp leading edge of a delta wing or strake creates so-called "nonlinear lift" which can be intelligently exploited by fighter aircraft designers.

Viscous transonic research has been carried out by either viscous-inviscid interaction procedures or Navier-Stokes procedures. The viscous-inviscid interaction procedure is quite convenient for the study of separation because the thin shear layer approximation remains valid in mildly separated flows [3]. Computationally, interaction codes require significantly less computer time than Navier-Stokes codes for problems with small regions of separation. However, Navier-Stokes formulations are generally much easier to code [42]. Moreover, for strong viscous-inviscid interactions, the current boundary-layer based schemes tend to break down. The present state-of-the-art associated with three-dimensional interaction methods applied to separated flows is far from mature [42]. There is some progress on computation of turbulent flows over wings primarily using integral boundary layer schemes, but these schemes cannot easily compute separated flows. The interested reader is directed to Refs. [42],[43],[44] for more information.

The primary difficulties associated with Navier-Stokes procedures are now restated for emphasis: 1) computer speed and memory limitations, 2) difficulties in turbulence modeling, and 3) difficulties in geometry definition and grid generation around sophisticated geometries. The Navier-Stokes simulations cited in the previous section utilized relatively coarse grids and required large amounts of computer time even on the latest supercomputers. However, the idea of dividing the control volume around the geometry into different "blocks" or "zones" and solving the governing equations interactively seems very attractive, because this technique reduces the difficulties of the first and third items listed above. This idea may be elaborated on as follows: Instead of putting the complete data base into the main computer memory, only the data associated with one grid zone can be put into main memory while the data from the other zones reside on some other secondary storage device. This relaxes the computer main memory burden. Second, and more importantly, this scheme relieves the task of generating grids around geometrically complex domains such as complete aircraft configurations. In this fashion, the total flow domain can be divided into multiple zones each of which may be in a different form to respond to the geometry, boundary condition, and physical constraints.

In this work, the Euler/Navier-Stokes equations using a zonal grid technique are solved to study three-dimensional flow separation on wings. For this purpose a computer code called Transonic Navier Stokes (TNS) has been developed [45], which presently utilizes four grid zones for isolated wing geometries.

In this code, the "thin-layer" approximation to the Reynolds-averaged Navier-Stokes equations is solved by utilizing highly clustered grids near the body. Away from the body, the inviscid-rotational features of the flow are simulated utilizing the Euler equations. To the authors' knowledge, the TNS computer program represents the first three-dimensional Euler/Navier-Stokes zonal algorithm.

CHAPTER 2

DESCRIPTION OF THE ZONAL PHILOSOPHY

2.1 Introduction

Historically the zonal philosophy is not new. It was used implicitly in the introduction of Boundary Layer theory by Prandtl [3] where the flow was divided into two different regions, inviscid and viscous. There are numerous examples of viscous-inviscid interaction research which use a type of zonal approach. Also, the zonal philosophy finds an application in turbulence modeling. As described by Kline et al. [46], zonal turbulence modeling is an attractive alternative to universal turbulence models.

The extensive use and application of zonal schemes in different forms has gained popularity recently. Boppe [47] illustrated that using nested grid systems around complex geometries such as arbitrary wing-body configurations with winglets, pods, canards and tails makes it very practical to construct transonic codes. Also, Lee [48], Lee and Ruppert [49], Atta [50] and Atta and Vadyak [51] have used the block grid approach for transonic potential computations. Other zonal grid approaches for the Euler equations have been used by Benek et al. [52], Hessenius and Pulliam [53], Rai [54] and Hessenius and Rai [55].

Numerical grid generation in three dimensions is one of the biggest pacing items in Computational Fluid Dynamics. Numerically generated curvilinear coordinate systems are commonly used around arbitrary geometries. Body fitted systems are especially helpful for the treatment of boundary conditions. In general, numerical grid generation involves the transformation of a complex physical space into a geometrically simple computational domain. When the geometry of interest in the physical space is simple enough, the transformation can be achieved in a straightforward manner. But as the geometry becomes more complicated, such as the wing/body/strake/tail combination of a contemporary aircraft, the issue of grid generation becomes indeed challenging, and sometimes the domain cannot be mapped into a single block. The practical problems encountered in the generation of a single grid about a complex geometry are as follows: Often times, trying to generate a single grid results in a skewed grid which causes solution inaccuracies. Another difficulty is obtaining the proper level of grid refinement in regions of flow gradients, such as a shear layer, a shock wave or a vortex. Moreover, trying to configure an acceptable grid via tuning of existing grid generation schemes requires substantial amounts of time and effort.

One approach to this challenging issue is to divide the domain into a number of geometrically simple subdomains, called "blocks" or "zones." Fig. 1 illustrates the idea of zonal grids for a wing/body/tail combination of a fighter airplane. As demonstrated here, each component is mapped into a simple rectangular computational box. There are a number of ways to structure zonal grids. In general, it is quite difficult to classify zonal grid techniques in a clear and concise fashion. In Fig. 2, an approach to zonal grid classification is presented. As suggested, zonal schemes can be divided into two groups. The first group is composed of schemes with overlapping grid zones, and the second group with zones which do not overlap (interface schemes). In the first group (overlap schemes), the overlapping may be either "complex," i.e., the zonal boundaries don't match each other in any way, or "simple" where the zonal boundaries coincide. The Chimera grid scheme of Ref. [52] exploits the complex overlap zonal grid technique. The present TNS code, however, makes use of the "simple overlap" zonal grid technique. Also, it is possible to construct other overlap schemes which blend complex and simple overlap schemes.

The second group of zonal schemes consists of "patched" grids which interface each other at common boundaries. This group can be divided into two subsets according to whether the grid lines at the common surface are continuous or discontinuous. In the first scheme, no discontinuity in function, spacing, or slope is permitted. The second scheme consists of discontinuous grids. The discontinuity can be in the grid spacing, in the function values or in the slope of the grid lines. Also, combinations of different kinds of discontinuities can be used in the same grid. This generally occurs when the flow field is divided into different zones beforehand, and then the grid in each zone is generated independently (see Refs. [48],[49],[56]). The discontinuous grids in Fig. 2 are also "metric discontinuous" in the context of Rai's [54] definitions. Interface boundary conditions are implemented between zones by either interpolation or other special techniques. For example, a conservative zonal boundary treatment for discontinuous grids is given in Refs. [53],[54], and [55].

The advantages of zonal grid schemes are summarized as follows:

1) The grid for any subregion of the domain can be generated easily.

2) The grid can be adapted to the problem. This is achieved by placing refined zones in regions of high gradients such as shear layers, shock waves, jets and wakes, vortices, etc., whereas coarse zones are used in regions of small gradients.

3) Different equation sets can be used in different zones; for instance, the Navier-Stokes equations are used in regions where viscous and/or heat transfer

effects are important and the Euler equations are used where inviscid rotational effects are important.

4) With the use of grid zoning, an efficient mesh topology can be improved, or an inefficient topology can be made acceptable.

A measure of grid efficiency, the Mesh Efficiency Ratio (MER) was defined in Ref. [57]. It is the ratio of the number of grid points on the surface of interest to the number of grid points in an average two-dimensional surface of the same three-dimensional grid. The latter quantity is simply the two-thirds power of the total number of grid points. Larger values of MER, in general, indicate more efficient grid topologies as opposed to the smaller values of MER which represent less efficient topologies. MER values on the order of one for an inviscid grid and on the order of one-half for a viscous grid are about average. Of course, this number can be changed by up to a factor of two depending on grid clustering. Representative values of MER for a few well-known isolated-wing grid topologies are shown in Table 1 for both viscous and inviscid grids. This table was constructed with conservative stretching estimates for all directions. Thus, larger values of MER could be obtained with more rapid stretching. More on the efficiency of mesh topologies can be found in Refs. [57], and [58].

Table 1. Comparison of several isolated-wing mesh topologies using the MER efficiency parameter

Mesh topology	MER (inviscid)	MER (viscous)
H-H	0.38	0.24
C-H	0.50	0.32
C-O	0.79	0.50
O-H	0.79	0.50
O-O	1.26	0.79
H-H (zonal)	1.13	0.71

As seen from Table 1, it is difficult to advocate the H-H topology about a wing involving viscous flow calculations because the boundary layer clustering at the wing surface must be continued upstream and downstream of the wing as well as outboard of the wing tip. Thus, many points are wasted, and the MER is as low as 0.2-0.3. With a zonal grid approach applied to the inefficient H-H topology, much improved MER values can be obtained as seen by the last entry in Table 1. However, the complete aircraft configuration is the ultimate aim of CFD, not isolated wings! Generally, the Cartesian nature of the H-H topology is an appropriate topology for wing/fuselage geometries. This is because, as seen in Fig. 1, the H-H grid topology allows each fuselage cross-section to be fitted

with an efficient polar-like grid, whereas the wing cross-sectional grid retains the Cartesian-like topology. This is a very flexible topology and can be modified to handle more complicated configurations. For example, in addition to the wing, other lifting surfaces including canards, strakes and horizontal and vertical stabilizers can be handled in a straightforward manner.

2.2 Zonal Grid Generation

In TNS, grid generation starts with the generation of a global single-zone grid which includes the entire flow field. This grid contains no viscous clustering and has an H-mesh topology in both the spanwise and chordwise directions. The global grid can be generated from either of two approaches: the elliptic solver approach of Sorenson and Steger [59], or the parabolic solver approach of Edwards [60]. They have the capability of generating suitable grids about isolated-wing geometries with either free-air or wind-tunnel wall outer boundaries. For the most part, the elliptic solver approach of Sorenson, which generates finite-difference grids by solving a set of Poisson's equations, is used in the present study. This grid generation method allows control over both grid point spacing along, and normal to, the boundaries and angles with which the grid lines intersect the boundaries. This control is obtained by specification of the boundary conditions and the inhomogeneous terms contained within the Poisson's equation. Once the boundary definition and grid characterictics have been set, the three-dimensional elliptic code solves the governing equations using a successive over-relaxation (SOR) procedure.

Once the base grid is generated, it is divided into zones utilizing a "zoning" algorithm. In the present TNS code an isolated wing grid is configured with four zones. The first grid zone (Grid 1) is, by and large, the coarse base grid itself with a small three-dimensional domain left open into which the rest of the grids and the wing are placed. The second grid zone(Grid 2) fills this open domain, with a small overlap region in common with Grid 1 and also another small three-dimensional domain for the third and fourth grids. Grid 2 is constructed so as to contain twice as many grid points in each spatial direction as the original base grid. This refinement of Grid 2 relative to the base grid is accomplished via cubic-spline interpolation.

The final two grid zones (Grids 3 and 4) are designed to capture the upper and lower surface viscous effects of the wing, respectively. They occupy the space left open by the block of points removed from Grid 2, again with a small region of overlap included. Grids 3 and 4 are constructed so as to contain the same number of points in both the spanwise and chordwise directions as Grid 2. But since they are to capture the viscous effects of the wing, the grid points in the normal direction are highly clustered. This four-zone grid topology produces an

overall grid with a MER of about 0.8. The outer two grid zones are topologically represented in the computational domain as cubes with smaller cubes removed from the middle, but the third and fourth grids are represented as simple cubes.

In order to illustrate this zonal grid topology, a series of figures is presented. The wing configuration used here is the so-called "WING C" which is a research wing and was designed by a cooperative effort between NASA-Ames Research Center and Lockheed-Georgia. The planform view of the WING C grid is presented in Fig. 3. The wing has an aspect ratio of 2.6, leading edge sweep of 45 degrees, taper ratio of 0.3, and a twist angle of 8.17 degrees. Fig. 4 shows a perspective view of the grid with the symmetry plane highlighted. From this view, the wing surface grid resolution including the treatment of the wing tip can be seen. A cross-sectional view of the grid in the vicinity of the wing, showing details of grid zones 2, 3 and 4 at the symmetry plane, is displayed in Fig. 5. Note that the Navier-Stokes grid expands in thickness from the leading edge toward the trailing edge to better capture the growing boundary layer. In the same plane, an expanded view of the WING C leading edge grid detail is presented in Fig. 6. The spanwise cross-sectional view of the wing grid showing part of zones 2, 3 and 4 is given in Fig. 7. The elliptic grid generation scheme was used for the grid just presented in Figs. 3-7, and was designed for free-air computations.

As was mentioned earlier, the elliptic and parabolic grid generators are capable of generating grids suitable for use with either free-air or wind-tunnel wall boundaries. Fig. 8 shows a typical grid with outer boundary positions specified to coincide with the position of the wind tunnel walls from the NASA-Ames High Reynolds Number Channel I [61]. The grid is plotted in perspective so that details on the upper and lower wind tunnel surfaces, the inflow and outflow planes, and the wing-symmetry plane are all visible. This grid, which was generated by the parabolic grid generation approach [60], becomes the outer coarse grid zone (Grid 1). This grid detail near the wing/symmetry plane juncture has been removed. It is in this region that grid zones 2, 3 and 4 are located as described earlier. The wing geometry used in the wind-tunnel flow simulation of Fig. 8 is shown in Fig. 9. It is composed of NACA 0012 cross-sections and has a taper ratio of 1.0, a leading-edge sweep of 20 degrees, an aspect ratio of 3, and is rigged in the tunnel wall grid at 2 degrees angle of attack.

The total number of grid points associated with the WING C and NACA 0012 grids for free air simulations is 165,321. The individual grid point breakdown for each zone is as follows: Grid 1, 63 x 26 x 25 = 40,950; Grid 2, 69 x 29 x 21 = 42,021; Grid 3, 61 x 27 x 25 = 41,175; and Grid 4, 61 x 27 x 25 = 41,175. The wind-tunnel wall grid for the NACA 0012 configuration has fewer grid points; it is an exact subset of the NACA 0012 wing free-air grid and consists of 149,071 points (see Fig. 8).

2.3 Zonal Interface Scheme

The zonal approach introduces a new aspect associated with boundary conditions, namely the interface conditions between neighboring blocks. Whereas the interior points of each zone are updated using the standard integration scheme, the boundary points are updated via interpolation. It was pointed out earlier that the zonal scheme followed here is a "simple overlap" one, and owing to this feature, the interpolation procedure is greatly simplified. This is because the grid zones are carefully constructed from a base grid such that surfaces requiring interpolation are coincident. The most complicated zonal interface boundary condition involves only a series of one-dimensional linear interpolations. This situation is illustrated in Fig. 10. In this hypothetical case, grid Zone 1 is a coarse grid which interfaces with Zone 2 which is a fine grid. To facilitate the implicitness of the iteration algorithm in the present approach, the blocks are overlapped by one to several mesh-cell widths.

In the interface boundary condition scheme, the idea is to obtain flow field information from the interior of Zone 1 and to use it to satisfy the proper boundary conditions on the ABCD surface of Zone 2. Since the grids of Zone 1 and Zone 2 have been constructed to coincide with plane ABCD, the process is greatly simplified. The ABCD surface is shown in transformed space in Fig. 10b. The points from both grid zones are indicated. Note that the grid points from Zone 1 represent a subset of the Zone 2 points. Hence, the dependent variables at the points marked with plus symbols (Zone 2) are computed by a series of linear interpolations using the points marked with circular symbols (Zone 1). The process of interpolating information back from Zone 2 to Zone 1, which is required for the EFGH surface is even simpler than in the first case. This is because the interpolation simply becomes "injection." That is, even though interpolation is carried out, the end result of this operation is the straight transfer of values from Zone 2 to Zone 1 without interpolation errors. This is because every grid point in the Zone 1 boundary (EFGH), has an exactly matching point on the corresponding internal plane (EFGH) of Zone 2. This is readily seen by looking at Fig. 10b and noting that every Zone 1 point (circular symbols) has an exact matching point in Zone 2 (plus symbols).

The present interface scheme is organized such that only the two planes involved in the interpolation need to be defined: the base and target planes. These interface surfaces are referred to as "planes." However, this is true only in the computational domain. In the physical domain these "planes" are actually curved three-dimensional surfaces. Each boundary plane at a grid zone interface, which requires data for boundary conditions, is called a target plane; and each interior plane which supplies interpolation data to a target plane, is called a base plane. For instance in Fig. 10, when we want to obtain flow field information

from the interior of Zone 1 and to use it as the boundary condition for Zone 2, the ABCD plane becomes the base plane in Zone 1 and at the same time it becomes a target plane for Zone 2. These base and target planes are grouped into three categories : J planes, K planes and L planes. Each one is defined by six integers. For example, the J planes are defined by : 1) the grid zone number from which the base or target surface is obtained, 2) the J plane number in that particular zone, 3) the starting K index, 4) the ending K index, 5) the starting L index, and 6) the ending L index. For instance in Fig. 10, the ABCD and EFGH planes are typical J planes. The K and L planes are defined in a similar way.

Whereas the base and target plane arrays completely define the dependent variable values to be used in the interface interpolation process, the independent variable values (spatial coordinates) are obtained from the grid distribution which passes through the origin of the coordinate system (the point at the wing root leading edge). Obviously, these grid distributions do not uniquely represent all the possible grid distributions that may exist in a general three-dimensional mesh. However, they offer a very flexible and easy to implement interpolation scheme with a reasonably small error. Moreover, if the interpolation is, for example, a simple halving of the mesh which is the case for the most part of the TNS grid, it is not important to know precise grid coordinates.

At the beginning of each iteration for grid zone NZ, boundary values for all grid zone NZ interface planes are updated from a storage array called BCBUF which must be shuffled back and forth from the extended storage. After the interface planes and any other standard boundary conditions are updated, the interior solution is updated by using the standard integration algorithm. Then any base planes that reside in grid zone NZ are interpolated to produce the corresponding target planes for use in neighboring grid zone interface boundaries. These target planes are stored in the BCBUF array. This completes the iteration for grid zone NZ and the algorithm proceeds to grid zone NZ+1.

A zonal boundary scheme in an ideal sense should be conservative and should permit distortion-free movement of flow discontinuities such as shocks and slip surfaces across zonal interfaces. Let us investigate our zonal boundary scheme with regards to this condition. The upper and lower grid interfaces between the inner Euler (zone 2) and Navier-Stokes blocks (zones 3 and 4) are one-to-one in both the ξ and η directions (streamwise and spanwise directions for a wing topology), but in the ζ direction these planes involve a spacing discontinuity or "metric discontinuity." This feature can be seen most easily in the grid plots of the Figs. 4-7. This is important because the interpolation process utilized automatically becomes an "injection" for these interface boundaries and therefore is conservative. Thus, a strong shock wave crossing these boundaries, which is quite likely to occur, should do so with minimal numerical inaccuracies. The

other interface boundary planes are composed of discontinuous grids and, in general, are not conservative, but could be made conservative if necessary by using the approach of Rai [54], and Hessenius and Rai [55].

2.4 Data Management

Once the grid is generated and divided into the proper zones, the flow solver is initiated. The iteration procedure starts in the outer Euler blocks (first Grid 1, then Grid 2) and ends with the two Navier-Stokes blocks, first the upper Navier-Stokes block (Grid 3) and then the lower block (Grid 4). Only one iteration using a spatially varying time step is completed in each zone before passing to the next. However, many iteration and/or time-stepping strategies could be used to improve convergence. Only the flow field solution (Q arrays), transformation Jacobian (J), metric quantities, and the turbulence model arrays (when appropriate) associated with a single block reside in main memory of the Cray-XMP at a time. The information associated with the other blocks resides in extended storage. On the Cray XMP this device is called the Solid State Device or SSD. The SSD is utilized functionally in the same manner as standard rotating disk extended storage. However, the SSD extended storage is physically made up of semiconductor memory and therefore is much faster. Using the SSD instead of disk greatly reduces I/O wait time, and for jobs which are normally I/O bound this is a significant advantage.

In the present zonal approach, the use of the SSD allows a great deal of flexibility because a larger number of grid blocks can be supported without significant additions to main memory. Of course the limiting factor with regard to this point is the size of SSD. The SSD installed with the NASA Ames Cray XMP presently has 16 million 64-bit words of memory. This can easily be extended to 32 million words if half precision (32 bits) is used. The current version of the TNS code, with grid dimensions as outlined above in the grid generation section, requires 5.8 million words of SSD storage. All arrays on the SSD are stored in 64-bit precision with the exception of the metric arrays which are stored with 32-bit precision. A test was performed with 64-bit metric storage that produced results very close to the case with 32-bit metric storage.

To allow more space in main memory, the metrics are shuffled into main memory from the SSD in two-dimensional planes as needed. This allows the maximum grid size of each grid zone to be about 50,000 points. Because the flow solver algorithm used in TNS is an Alternating Direction Implicit (ADI) algorithm with implicit sweeps in all three directions, the metrics must be transferred into main memory with three different orientations, in x-y planes, x-z planes and y-z planes. Thus, there are three different metric orientations stored on the SSD. Because of the availability of so much storage on the SSD, this does not cause

any problem and makes overall memory management more efficient. In addition, each of the metric arrays is required in main memory several times for each grid zone during each iteration. This places extreme demands on the TNS I/O requirements. Nevertheless, with the efficiency level afforded by the SSD, these I/O requirements are handled without problem.

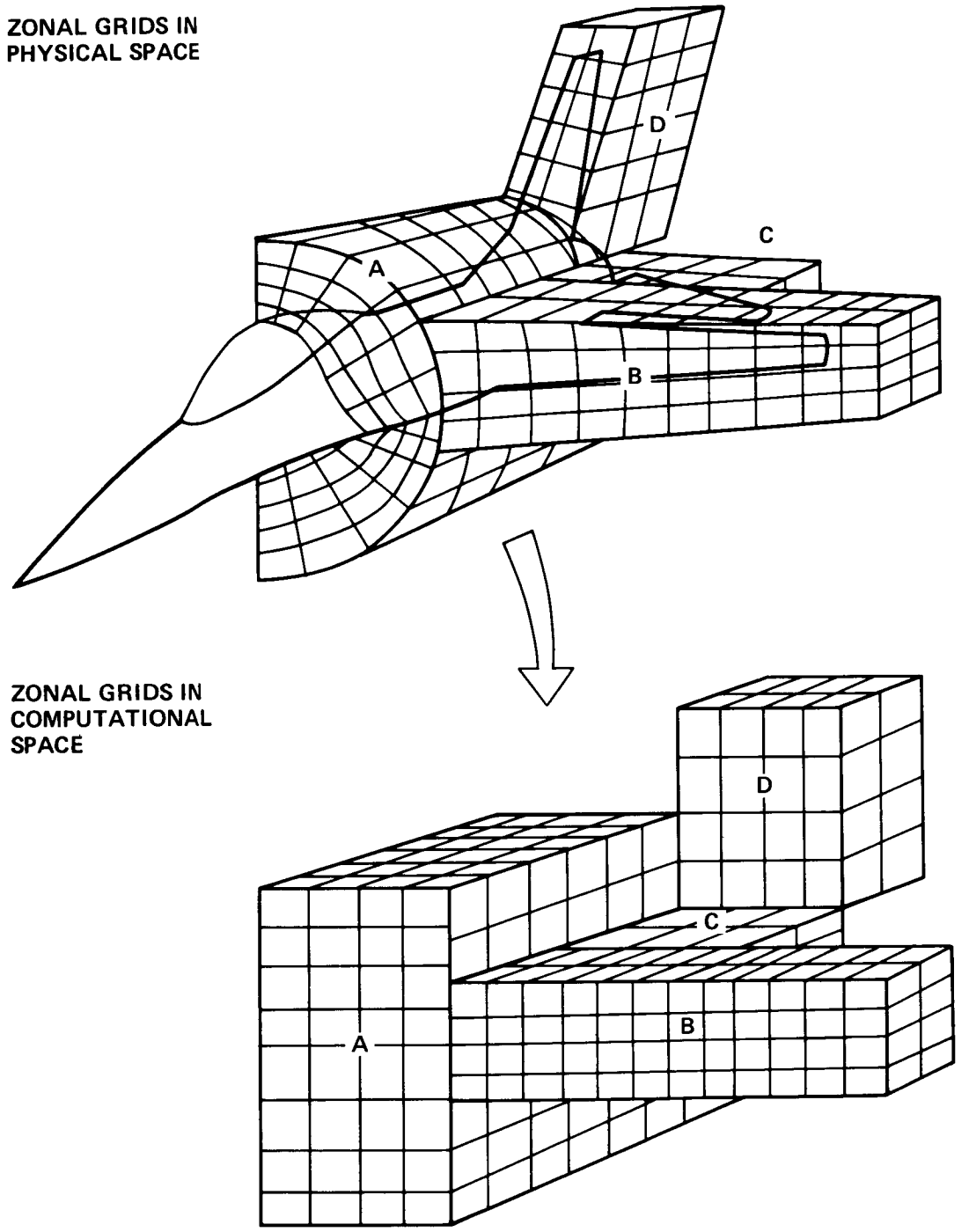

Fig. 1. Body-conforming zonal grids of a fighter aircraft configuration in the physical and computational spaces.

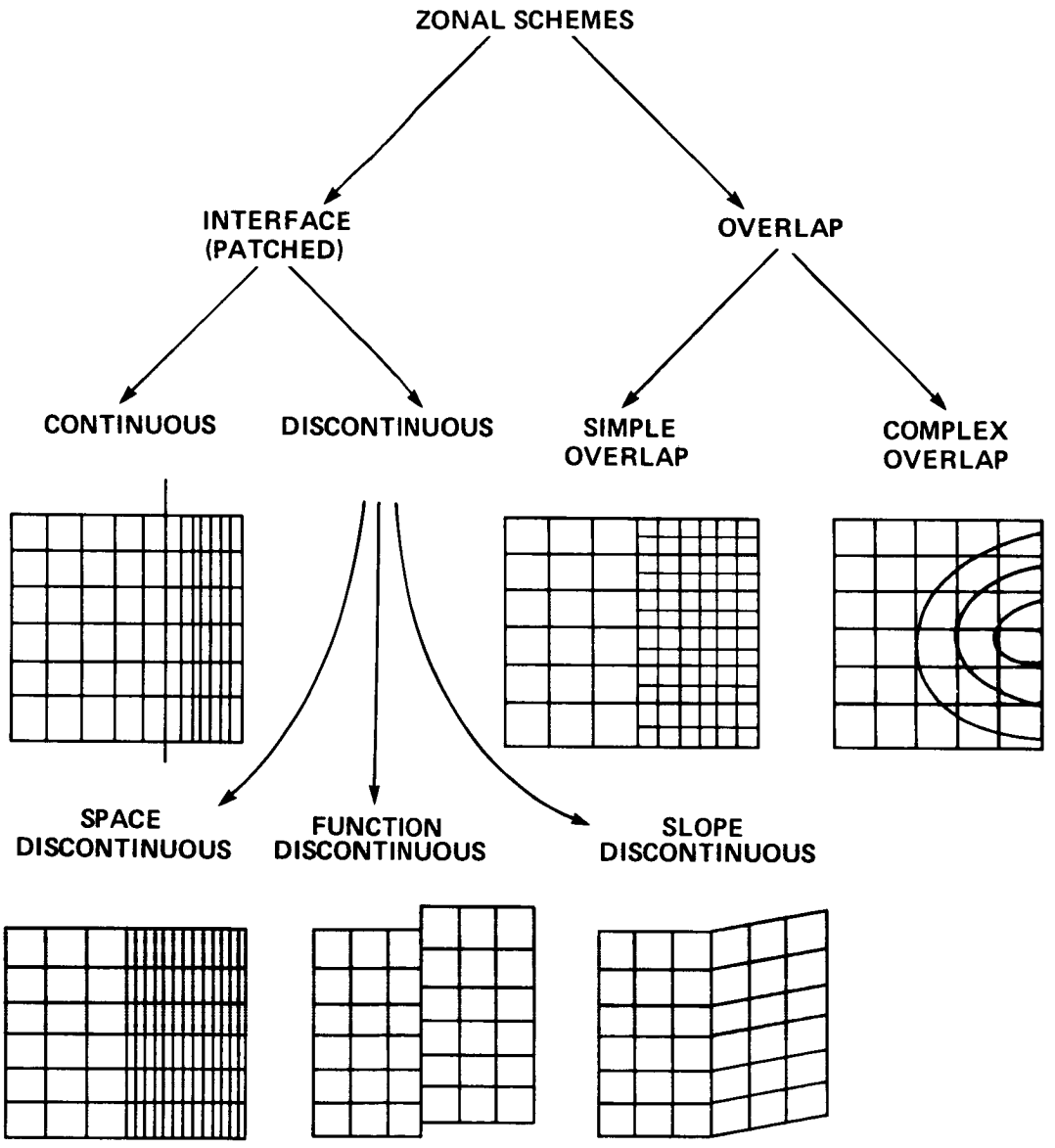

Fig. 2. An approach to the classification of the present zonal grid techniques.

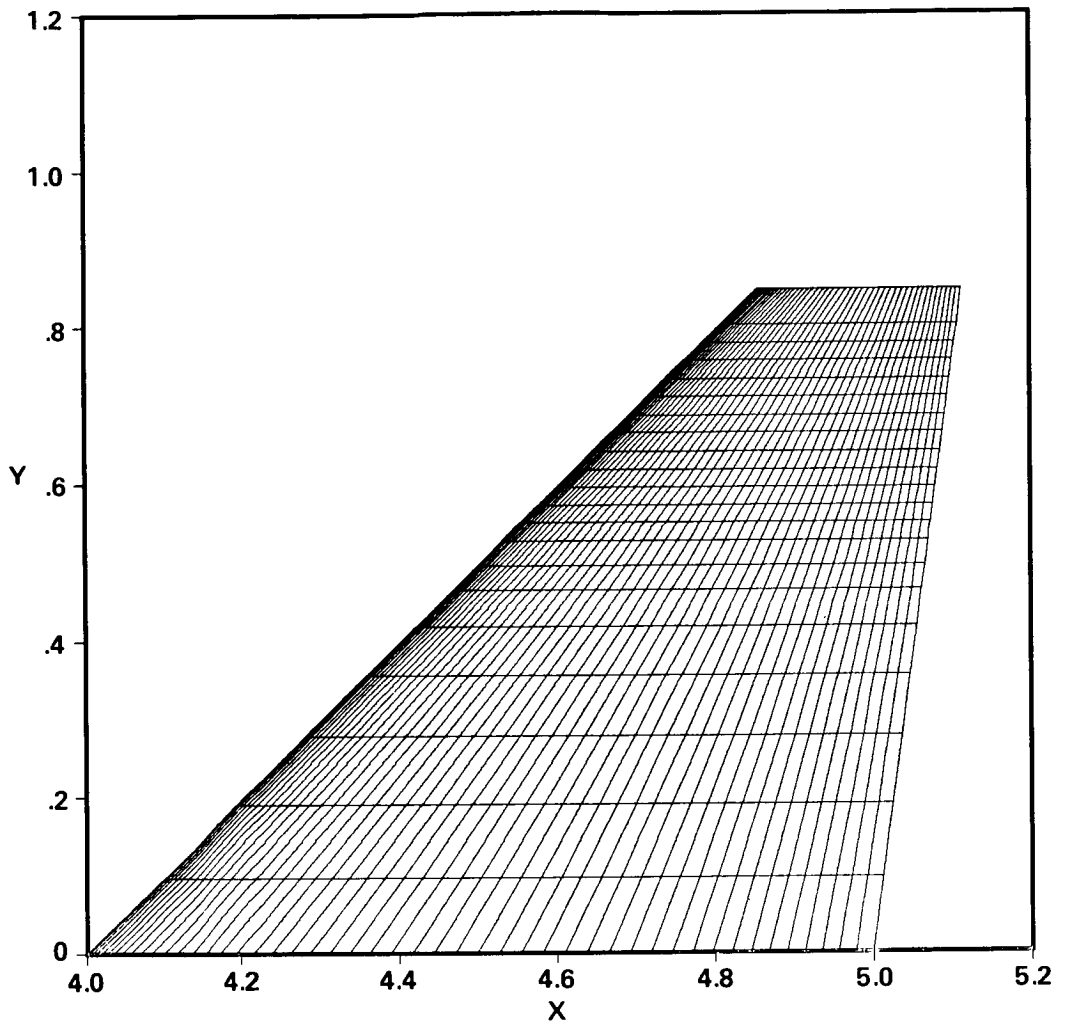

Fig. 3. Planform view of WING C: $AR = 2.6$, $\Lambda_{LE} = 45°$, $\alpha_{TWIST} = 8.17°$, $TR = 0.3$.

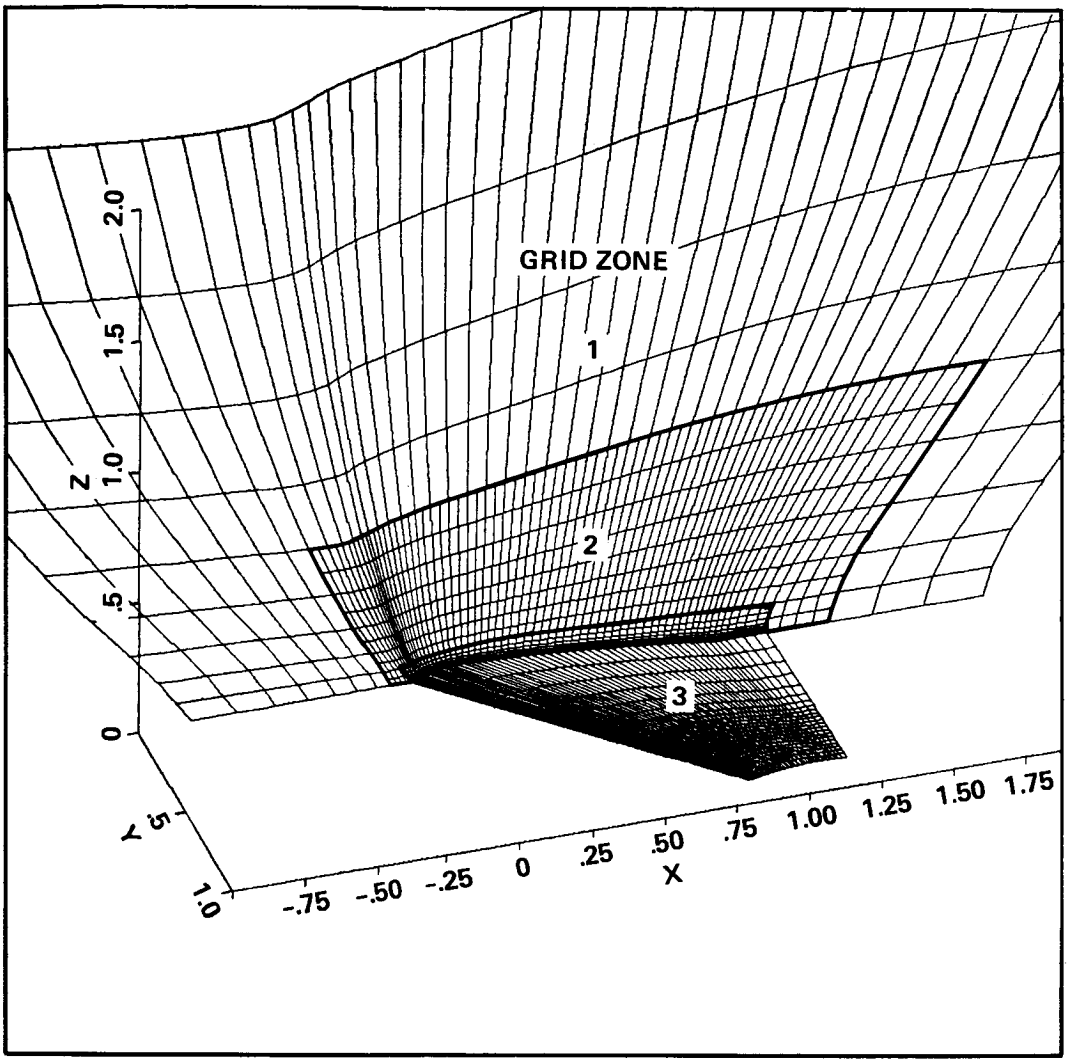

Fig. 4. Perspective view of embedded grid with upper symmetry plane ($y = 0, z \geq 0$) and wing surface highlighted.

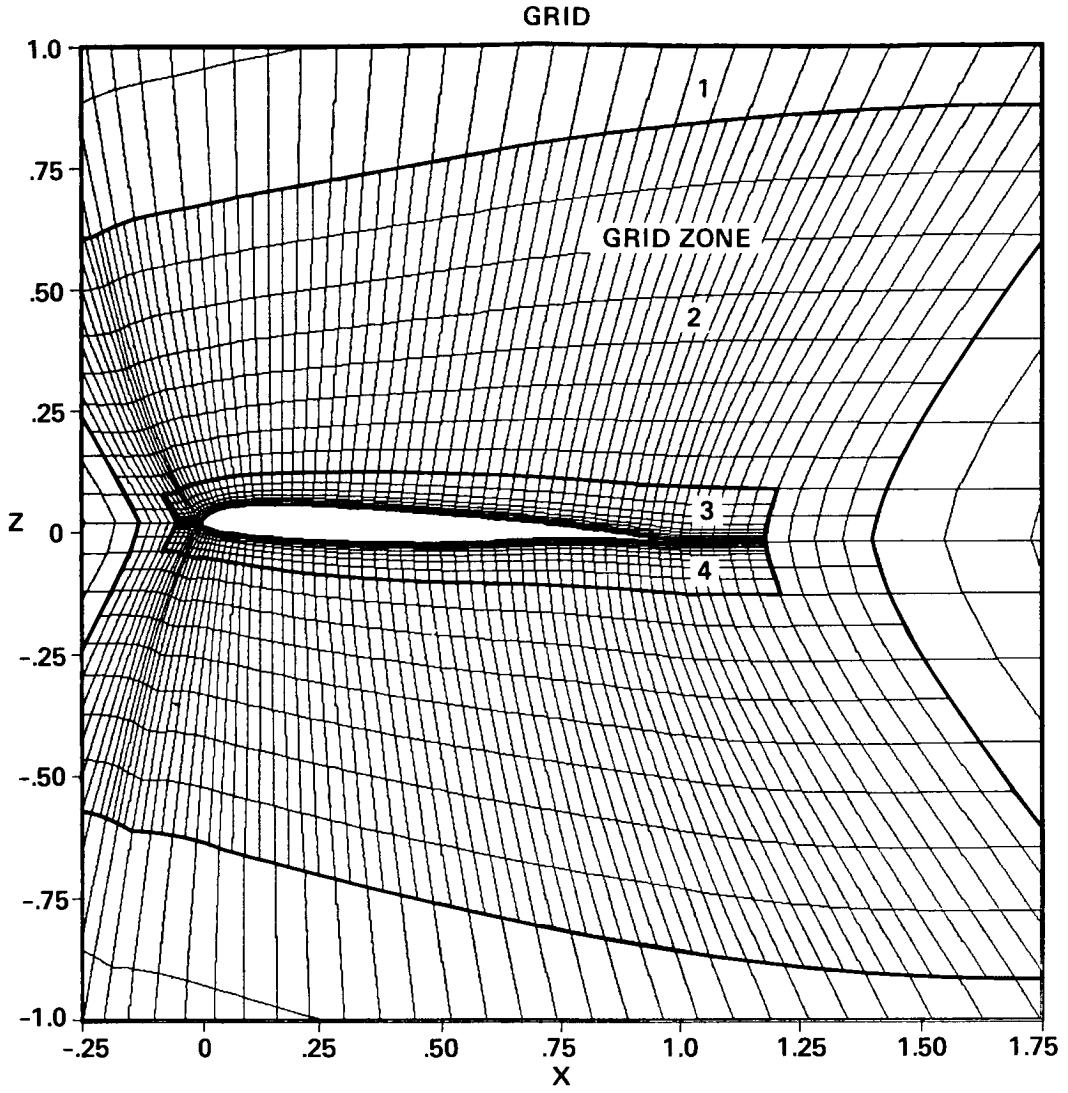

Fig. 5. Expanded view of the embedded grid near wing geometry showing four zones.

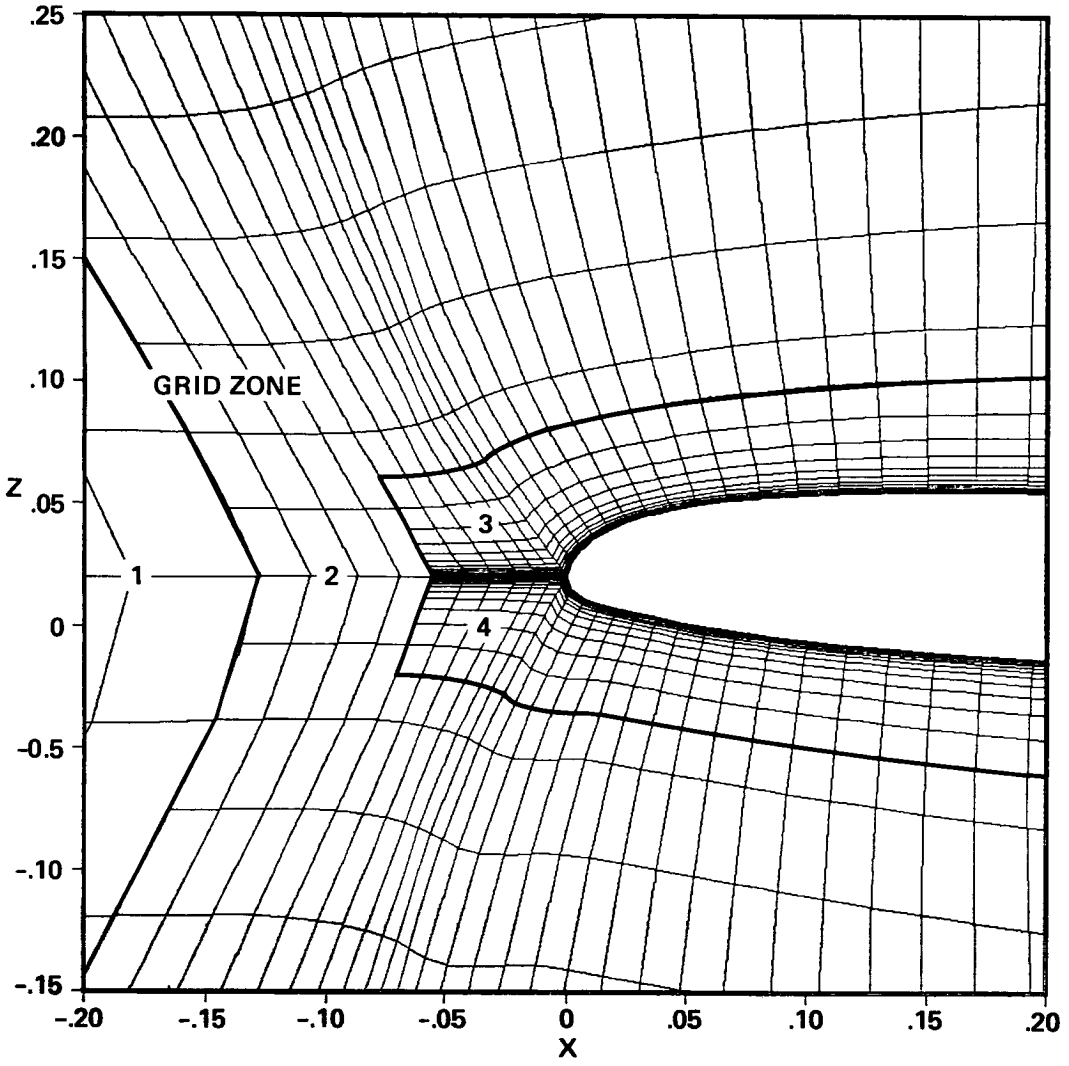

Fig. 6. Expanded view of the WING C leading edge grid details.

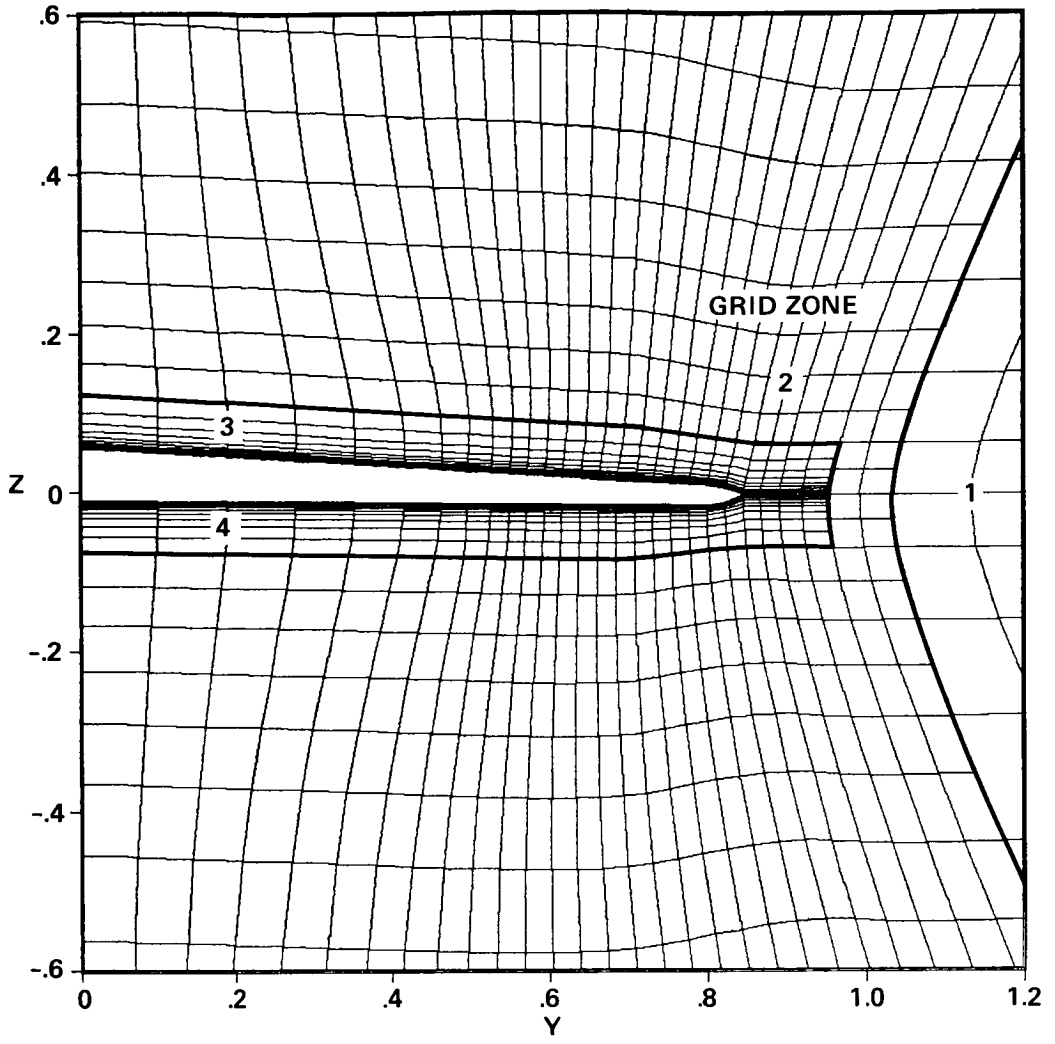

Fig. 7. Spanwise cross-sectional view of the wing grid showing parts of Zones 2, 3 and 4.

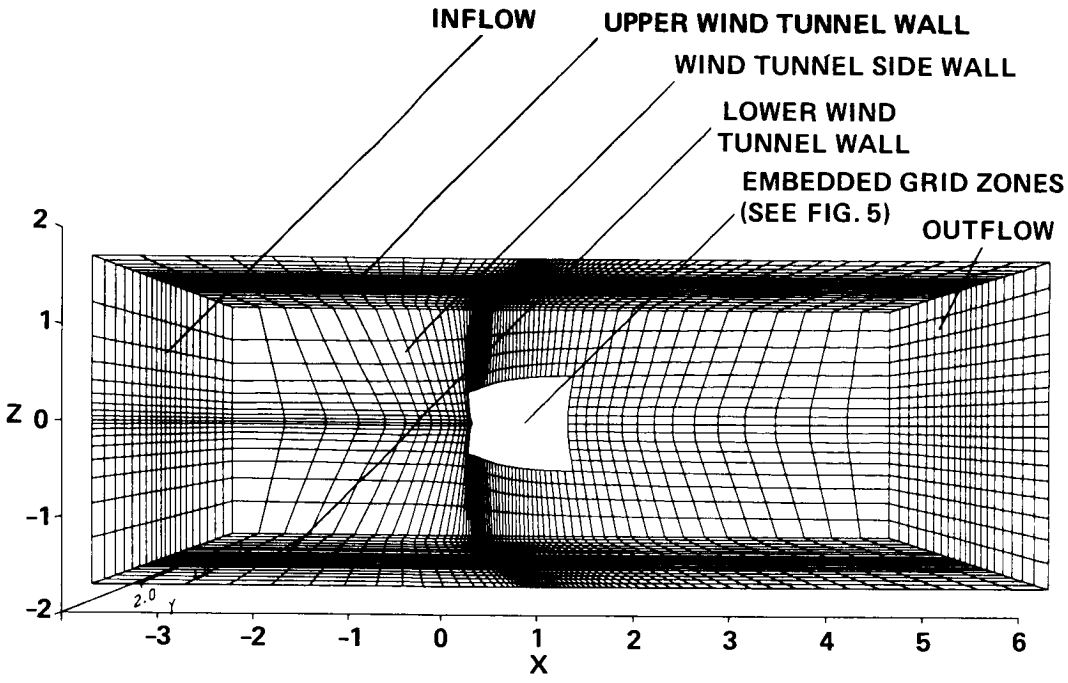

Fig. 8. Global finite-difference grid showing detail on wind tunnel walls.

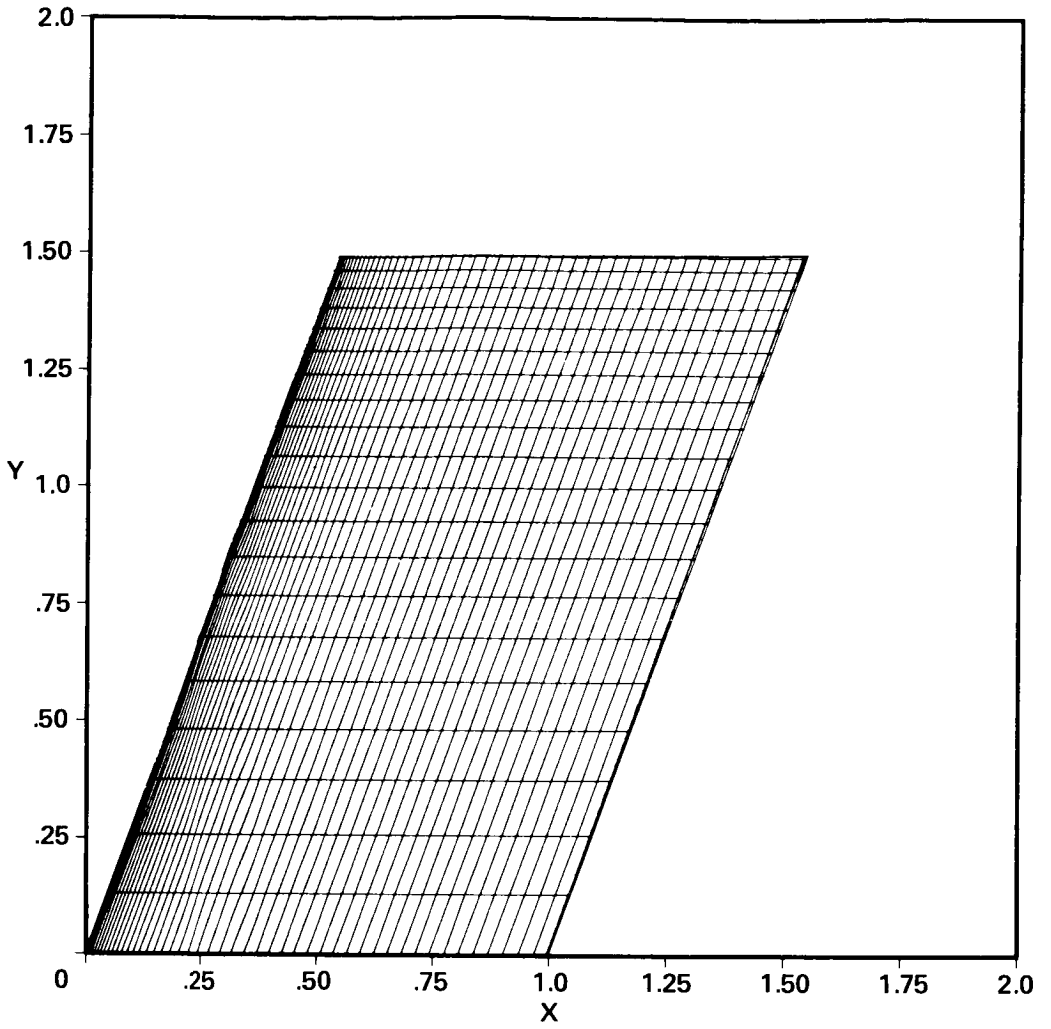

Fig. 9. Planform view of NACA 0012 wing: $AR = 3$, $\Lambda_{LE} = 20^{\circ}$, $\alpha_{TWIST} = 0^{\circ}$, $TR = 1$.

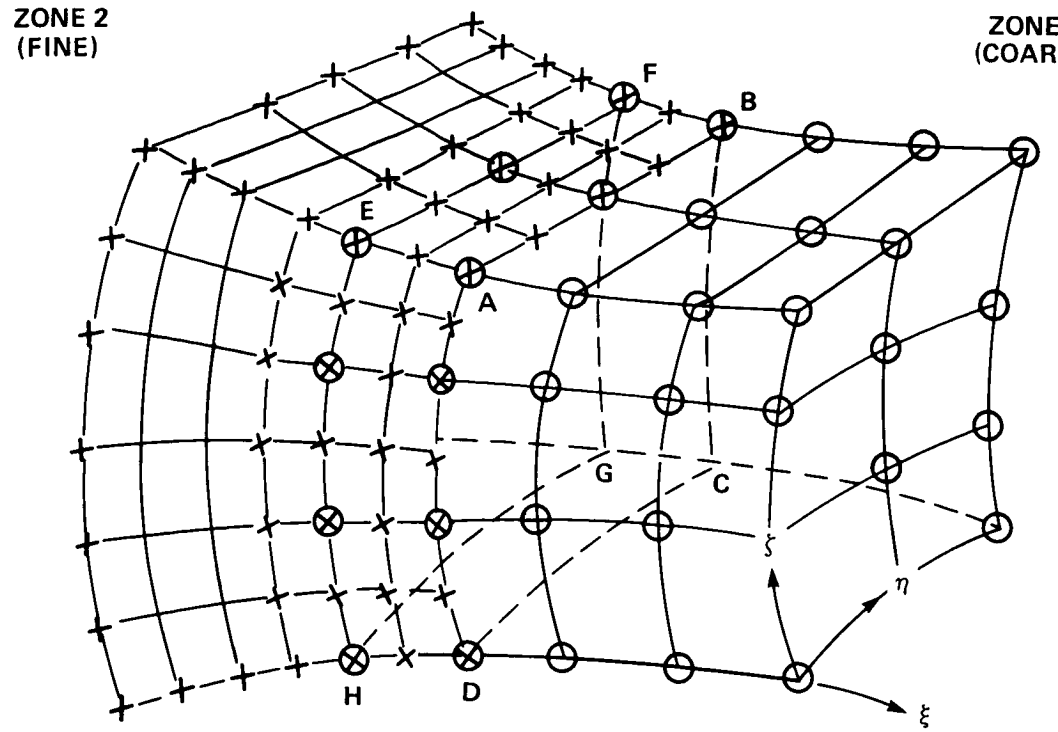

(a) TWO-ZONE GRID SHOWING OVERLAP AT ABCD AND EFGH PLANES IN PHYSICAL SPACE

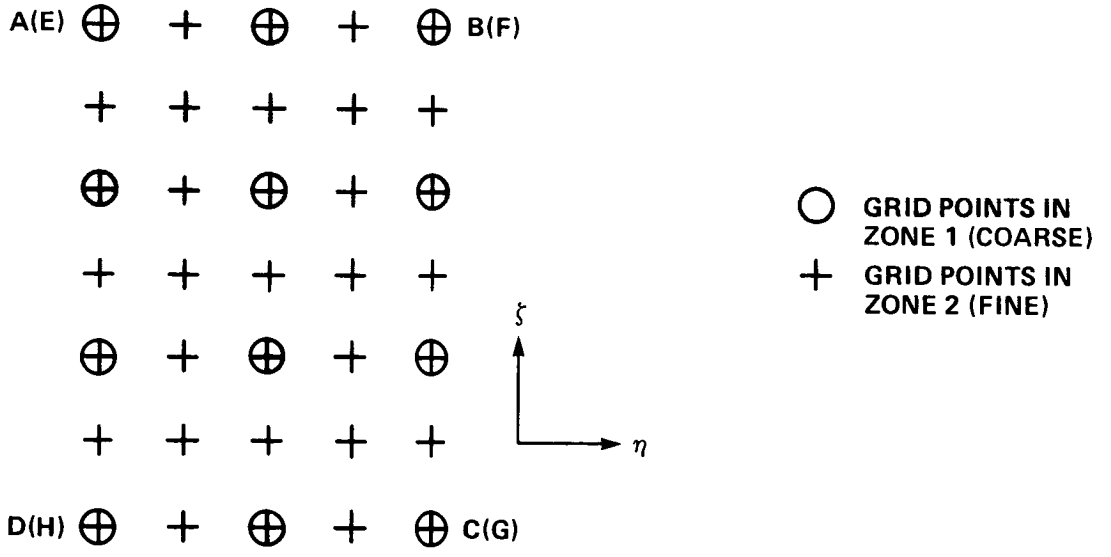

(b) GRID POINT DETAIL IN THE OVERLAP REGION IN TRANSFORMED SPACE.

Fig. 10. Interface procedure of the zonal grids.

CHAPTER 3

DESCRIPTION OF THE PHYSICAL EQUATIONS AND THE NUMERICAL METHODS

3.1 Introduction

The equations solved in this study are the Euler and Reynolds-averaged Navier-Stokes equations written in strong conservation form. The Reynolds-averaged equations are simplified by using the standard thin-layer approximation for the viscous terms. Once the zonal scheme is developed, any of the standard Navier-Stokes integration algorithms can be used. In this study, the basic governing equations and numerical algorithm including the turbulence model have been taken from the Pulliam-Steger ARC3D computer code [62]. To establish a basic level of understanding for the present approach, certain characteristics of the ARC3D computer code used within TNS are now briefly discussed.

The governing equations are generally nondimensionalized by free-stream quantities and are transformed to the computational domain (ξ, η, ς) so as to preserve the strong conservation form of the equations (see Sec. 3.2). The time-dependent metrics which occur in the most general form of the Euler/Navier-Stokes equations have been omitted. This was done to save computer memory. Thus, the present formulation is incapable of time varying grids but still has the capability of resolving time-dependent flow-field physics. However, adding the time-dependent grid capability back into the present code is not a difficult task.

Two numerical algorithms have been investigated within the TNS computer code, an ADI algorithm which solves block-tridiagonal matrices along each coordinate direction and a diagonalized algorithm which solves scalar pentadiagonal matrices along each coordinate direction (see Sec. 3.3). The first algorithm is a variation of the Beam-Warming ADI scheme [63], and the second is an extension of this scheme due to Pulliam and Chaussee [64]. Both schemes use the standard second-order-accurate central differencing of the governing equations to construct the appropriate spatial differencing scheme. The block scheme uses a fourth-order-accurate smoothing operator on the right-hand side of the iteration algorithm and a second-order-accurate smoothing operator on the left-hand side. The diagonal scheme uses a fourth-order-accurate smoothing operator on both the left- and right-hand sides.

The diagonal algorithm has been implemented with two spatially varying

time-step philosophies; one which scales the time step with the transformation Jacobian and the other with a combination Jacobian/local-solution variation. The block algorithm uses a time-step which is constant in a spatial sense as well as from grid zone to grid zone.

All of the results presented in this report have been computed using the diagonal algorithm with fourth-order implicit smoothing and the Jacobian-scaled time-step variation. This algorithm combination seemed to be the most computationally efficient of all the variations tested. More discussion of these aspects can be found in Flores [65] where a comparison of these algorithm variations in conjunction with zonal grid variations has been made. The turbulence model used in the TNS computer program was the Baldwin-Lomax algebraic model [29] because of the ease with which it can be implemented.

3.2 Governing Equations and Approximations

3.2.1 Equations in Non-Dimensional Form

The strong conservation law form of the Navier-Stokes equations are used for shock capturing purposes. The equations in Cartesian coordinates in non-dimensional form can be written as (cf. Peyret and Viviand [66])

$$\frac{\partial Q}{\partial t} + \frac{\partial E}{\partial x} + \frac{\partial F}{\partial y} + \frac{\partial G}{\partial z} = \frac{\partial E_\nu}{\partial x} + \frac{\partial F_\nu}{\partial y} + \frac{\partial G_\nu}{\partial z} \tag{3.1}$$

where

$$Q = \begin{bmatrix} \rho \\ \rho u \\ \rho v \\ \rho w \\ e \end{bmatrix},$$

$$E = \begin{bmatrix} \rho u \\ \rho u^2 + p \\ \rho uv \\ \rho uw \\ u(e+p) \end{bmatrix}, \quad F = \begin{bmatrix} \rho v \\ \rho uv \\ \rho v^2 + p \\ \rho vw \\ v(e+p) \end{bmatrix}, \quad G = \begin{bmatrix} \rho w \\ \rho uw \\ \rho vw \\ \rho w^2 + p \\ w(e+p) \end{bmatrix}, \tag{3.2}$$

$$E_\nu = Re^{-1} \begin{bmatrix} 0 \\ \tau_{xx} \\ \tau_{yx} \\ \tau_{zx} \\ \beta_x \end{bmatrix}, \quad F_\nu = Re^{-1} \begin{bmatrix} 0 \\ \tau_{xy} \\ \tau_{yy} \\ \tau_{zy} \\ \beta_y \end{bmatrix}, \quad G_\nu = Re^{-1} \begin{bmatrix} 0 \\ \tau_{xz} \\ \tau_{yz} \\ \tau_{zz} \\ \beta_z \end{bmatrix}.$$

with

$$
\begin{aligned}
\tau_{xx} &= \lambda(u_x + v_y + w_z) + 2\mu u_x \\
\tau_{yy} &= \lambda(u_x + v_y + w_z) + 2\mu v_y \\
\tau_{zz} &= \lambda(u_x + v_y + w_z) + 2\mu w_z \\
\tau_{xy} &= \tau_{yx} = \mu(u_y + v_x) \\
\tau_{xz} &= \tau_{zx} = \mu(u_z + w_x) \\
\tau_{yz} &= \tau_{zy} = \mu(v_z + w_y) \\
\beta_x &= \gamma\kappa Pr^{-1}\partial_x e_I + u\tau_{xx} + v\tau_{xy} + w\tau_{xz} \\
\beta_y &= \gamma\kappa Pr^{-1}\partial_y e_I + u\tau_{yx} + v\tau_{yy} + w\tau_{yz} \\
\beta_z &= \gamma\kappa Pr^{-1}\partial_z e_I + u\tau_{zx} + v\tau_{zy} + w\tau_{zz} \\
e_I &= e\rho^{-1} - 0.5(u^2 + v^2 + w^2)
\end{aligned}
\tag{3.3}
$$

The Cartesian velocity components u, v, and w are nondimensionalized by a_∞ (the free-stream speed of sound), density ρ is nondimensionalized by ρ_∞; and the total energy per unit volume e is nondimensionalized by $\rho_\infty a_\infty^2$. Pressure can be found from the ideal gas law as

$$p = (\gamma - 1)[e - 0.5\rho(u^2 + v^2 + w^2)] \tag{3.4}$$

and throughout γ is the ratio of the specific heats. Also, κ is the coefficient of thermal conductivity, μ is the dynamic viscosity, and λ from the Stokes' hypothesis is $-2/3\mu$. The Reynolds number is Re and the Prandtl number is Pr.

To enhance numerical accuracy and efficiency and to handle boundary conditions more easily, the governing equations are transformed from the Cartesian coordinates to general curvilinear coordinates(Fig. 11) where

$$
\begin{aligned}
\tau &= t \\
\xi &= \xi(x, y, z, t) \\
\eta &= \eta(x, y, z, t) \\
\varsigma &= \varsigma(x, y, z, t).
\end{aligned}
\tag{3.5}
$$

The resulting transformed equations are not much more complicated than the original Cartesian set and can be written in nondimensional form as

$$\frac{\partial}{\partial\tau}\hat{Q} + \frac{\partial}{\partial\xi}(\hat{E} - \hat{E}_v) + \frac{\partial}{\partial\eta}(\hat{F} - \hat{F}_v) + \frac{\partial}{\partial\varsigma}(\hat{G} - \hat{G}_v) = 0 \tag{3.6}$$

where

$$\hat{Q} = J^{-1}\begin{bmatrix} \rho \\ \rho u \\ \rho v \\ \rho w \\ e \end{bmatrix}, \qquad \hat{E} = J^{-1}\begin{bmatrix} \rho U \\ \rho u U + \xi_x p \\ \rho v U + \xi_y p \\ \rho w U + \xi_z p \\ (e + p)U - \xi_t p \end{bmatrix},$$

$$\hat{F} = J^{-1}\begin{bmatrix} \rho V \\ \rho uV + \eta_x p \\ \rho vV + \eta_y p \\ \rho wV + \eta_z p \\ (e+p)V - \eta_t p \end{bmatrix}, \qquad \hat{G} = J^{-1}\begin{bmatrix} \rho W \\ \rho uW + \zeta_x p \\ \rho vW + \zeta_y p \\ \rho wW + \zeta_z p \\ (e+p)W - \xi_t p \end{bmatrix}. \tag{3.7}$$

and

$$\begin{aligned} U &= \xi_t + \xi_x u + \xi_y v + \xi_z w \\ V &= \eta_t + \eta_x u + \eta_y v + \eta_z w \\ W &= \zeta_t + \zeta_x u + \zeta_y v + \zeta_z w. \end{aligned} \tag{3.8}$$

where U, V, and W are contravariant velocity components written without metric normalization. The viscous flux terms are given by

$$\hat{E}_\nu = J^{-1}Re^{-1}\begin{bmatrix} 0 \\ \xi_x\tau_{xx} + \xi_y\tau_{xy} + \xi_z\tau_{xz} \\ \xi_x\tau_{yx} + \xi_y\tau_{yy} + \xi_z\tau_{yz} \\ \xi_x\tau_{zx} + \xi_y\tau_{zy} + \xi_z\tau_{zz} \\ \xi_x\beta_x + \xi_y\beta_y + \xi_z\beta_z \end{bmatrix},$$

$$\hat{F}_\nu = J^{-1}Re^{-1}\begin{bmatrix} 0 \\ \eta_x\tau_{xx} + \eta_y\tau_{xy} + \eta_z\tau_{xz} \\ \eta_x\tau_{yx} + \eta_y\tau_{yy} + \eta_z\tau_{yz} \\ \eta_x\tau_{zx} + \eta_y\tau_{zy} + \eta_z\tau_{zz} \\ \eta_x\beta_x + \eta_y\beta_y + \eta_z\beta_z \end{bmatrix}, \tag{3.9}$$

$$\hat{G}_\nu = J^{-1}Re^{-1}\begin{bmatrix} 0 \\ \zeta_x\tau_{xx} + \zeta_y\tau_{xy} + \zeta_z\tau_{xz} \\ \zeta_x\tau_{yx} + \zeta_y\tau_{yy} + \zeta_z\tau_{yz} \\ \zeta_x\tau_{zx} + \zeta_y\tau_{zy} + \zeta_z\tau_{zz} \\ \zeta_x\beta_x + \zeta_y\beta_y + \zeta_z\beta_z \end{bmatrix}.$$

where the components of the shear-stress tensor and heat-flux vector in nondimensional form were given in (3.3). Here, the Cartesian derivatives are expanded in ξ, η, ζ space via chain-rule relations such as

$$u_x = \xi_x u_\xi + \eta_x u_\eta + \zeta_x u_\zeta$$

Finally, the metric terms are obtained from chain-rule expansion of x_ξ, y_η, etc., and solved for ξ_x, ξ_y, etc., to give

$$\begin{aligned} \xi_x &= J(y_\eta z_\zeta - y_\zeta z_\eta) & \eta_x &= J(z_\xi y_\zeta - y_\xi z_\zeta) \\ \xi_y &= J(z_\eta x_\zeta - x_\eta z_\zeta) & \eta_y &= J(x_\xi z_\zeta - x_\zeta z_\xi) \\ \xi_z &= J(x_\eta y_\zeta - y_\eta x_\zeta) & \eta_z &= J(y_\xi x_\zeta - x_\xi y_\zeta) \\ \zeta_x &= J(y_\xi z_\eta - z_\xi y_\eta) & \xi_t &= -x_\tau\xi_x - y_\tau\xi_y - z_\tau\xi_z \\ \zeta_y &= J(x_\eta z_\xi - x_\xi z_\eta) & \eta_t &= -x_\tau\eta_x - y_\tau\eta_y - z_\tau\eta_z \\ \zeta_z &= J(x_\xi y_\eta - y_\xi x_\eta) & \zeta_t &= -x_\tau\zeta_x - y_\tau\zeta_y - z_\tau\zeta_z \end{aligned} \tag{3.10}$$

and

$$J^{-1} = x_\xi y_\eta z_\varsigma + x_\varsigma y_\xi z_\eta + x_\eta y_\varsigma z_\xi - x_\xi y_\varsigma z_\eta - x_\eta y_\xi z_\varsigma - x_\varsigma y_\eta z_\xi$$

3.2.2 Thin-Layer Approximation

In high Reynolds number flows, the viscous effects are confined to a thin layer near rigid boundaries. In most cases, there are only enough grid points to resolve the gradients normal to the body by clustering the grid in the normal direction, and resolution along the body is similar to what is needed in inviscid flow. As a result, even though the full derivatives are retained in the equations, the gradients along the body are not resolved unless the streamwise and circumferential grid spacings are sufficiently small. Hence, for many Navier-Stokes computations, the viscous derivatives along the body are dropped. This leads to the thin-layer Navier-Stokes equations.

The thin-layer model requires a boundary layer type coordinate system. In our case, the ξ and η directions are along the body and the viscous derivatives associated with these directions are dropped, whereas the terms in ς are retained and the body surface is mapped onto a constant ς surface. Thus, Eq. (3.6) simplifies to

$$\partial_\tau \hat{Q} + \partial_\xi \hat{E} + \partial_\eta \hat{F} + \partial_\varsigma \hat{G} = Re^{-1} \partial_\varsigma \hat{S} \tag{3.11}$$

where

$$\hat{S} = J^{-1} \begin{bmatrix} 0 \\ \mu(\varsigma_x^2 + \varsigma_y^2 + \varsigma_z^2)u_\varsigma + (\mu/3)(\varsigma_x u_\varsigma + \varsigma_y v_\varsigma + \varsigma_z w_\varsigma)\varsigma_x \\ \mu(\varsigma_x^2 + \varsigma_y^2 + \varsigma_z^2)v_\varsigma + (\mu/3)(\varsigma_x u_\varsigma + \varsigma_y v_\varsigma + \varsigma_z w_\varsigma)\varsigma_y \\ \mu(\varsigma_x^2 + \varsigma_y^2 + \varsigma_z^2)w_\varsigma + (\mu/3)(\varsigma_x u_\varsigma + \varsigma_y v_\varsigma + \varsigma_z w_\varsigma)\varsigma_z \\ \{(\varsigma_x^2 + \varsigma_y^2 + \varsigma_z^2)|0.5\mu(u^2 + v^2 + w^2)_\varsigma \\ + \mu Pr^{-1}(\gamma - 1)^{-1}(a^2)_\varsigma] + (\mu/3)(\varsigma_x u + \varsigma_y v + \varsigma_z w) \\ \times (\varsigma_x u_\varsigma + \varsigma_y v_\varsigma + \varsigma_z w_\varsigma)\} \end{bmatrix} \tag{3.12}$$

It should be emphasized that the thin-layer approximation is valid only for high Reynolds number flows. Also, very large turbulent eddy viscosities invalidate the model.

3.3 Numerical Method

The finite-difference schemes used are the implicit approximate factorization algorithm in delta form by Beam and Warming [63] and a diagonal implicit algorithm by Pulliam and Chaussee [64]. Implicit methods are chosen to avoid the time-step restriction when small grid spacing is used. When spatial resolution

of large gradients such as that associated with shock waves or viscous effects are needed, highly refined grids are required. These requirements yield stiff problems which in turn restrict the time step to very small values. Implicit methods are useful in avoiding such stiffness, and large time steps compared to those of explicit schemes can be used without degrading accuracy.

3.3.1 Beam-Warming Block ADI Algorithm

The basic Beam-Warming algorithm is first- or second-order accurate in time and second- or fourth-order accurate in space. The equations are factored (spatially split) which, for a given time iteration, reduces the process to three one-dimensional problems. Due to the second-order central-difference operators employed, the algorithm produces block tridiagonal systems for each spatial dimension. The stability and accuracy of the numerical algorithm is described by Beam and Warming [63]. According to the linear analysis, the numerical scheme is unconditionally stable in two dimensions but in actual practice time step limits are encountered because of the nonlinear nature of the equations. However, this limitation is much less stringent than comparable explicit schemes. In three dimensions the algorithm is unconditionally unstable, but stability is maintained by the addition of artificial dissipation terms.

The finite-difference algorithm due to Beam and Warming applied to (3.11) results in the following approximate factorization:

$$\begin{aligned}
&(I + h\delta_\xi \hat{A}^n + D_\xi^{(2)})(I + h\delta_\eta \hat{B}^n + D_\eta^{(2)})\times \\
&(I + h\delta_\varsigma \hat{C}^n - hRe^{-1}\delta_\varsigma J^{-1}\hat{M}^n J + D_\varsigma^{(2)})\triangle\hat{Q}^n = \hat{R}^n \\
&= -\triangle\tau(\delta_\xi \hat{E}^n + \delta_\eta \hat{F}^n + \delta_\varsigma \hat{G}^n - Re^{-1}\delta_\varsigma \hat{S}^n) - D^{(4)}\hat{Q}^n
\end{aligned} \tag{3.13}$$

where δ is the central-difference operator and $\triangle$ and ∇ are forward and backward-difference operators, e.g.

$$\begin{aligned}
\delta_\xi \hat{Q} &= [\hat{Q}(\xi + \triangle\xi, \eta, \varsigma) - \hat{Q}(\xi - \triangle\xi, \eta, \varsigma)]/2\triangle\xi \\
\triangle_\xi \hat{Q} &= [\hat{Q}(\xi + \triangle\xi, \eta, \varsigma) - \hat{Q}(\xi, \eta, \varsigma)]/\triangle\xi \\
\nabla_\xi \hat{Q} &= [\hat{Q}(\xi, \eta, \varsigma) - \hat{Q}(\xi - \triangle\xi, \eta, \varsigma)]/\triangle\xi
\end{aligned} \tag{3.14}$$

Indices denoting spatial location are suppressed and $h = \triangle\tau$ corresponds to first-order time-accurate Euler Implicit and $h = \triangle\tau/2$ to second-order time-accurate Trapezoidal Rule. $D_\xi^{(2)}, D_\eta^{(2)}$ and $D_\varsigma^{(2)}$ are the implicit and $D_e^{(4)}$ is the explicit smoothing operator which will be explained later, in Section (3.4).

The Jacobian matrices $\hat{A}^n$, $\hat{B}^n$ and $\hat{C}^n$ are obtained by linearizing the flux

vectors $\hat{E}^n$, $\hat{F}^n$ and $\hat{G}^n$ in time such that

$$\begin{aligned}\hat{E}^{n+1} &= \hat{E}^n + \hat{A}^n(\hat{Q}^{n+1} - \hat{Q}^n) + O(\Delta\tau^2)\\ \hat{F}^{n+1} &= \hat{F}^n + \hat{B}^n(\hat{Q}^{n+1} - \hat{Q}^n) + O(\Delta\tau^2)\\ \hat{G}^{n+1} &= \hat{G}^n + \hat{C}^n(\hat{Q}^{n+1} - \hat{Q}^n) + O(\Delta\tau^2)\end{aligned} \tag{3.15}$$

where indices denoting spatial location are suppressed again and

$$\hat{A} = \frac{\partial \hat{E}}{\partial \hat{Q}}, \quad \hat{B} = \frac{\partial \hat{F}}{\partial \hat{Q}}, \quad \hat{C} = \frac{\partial \hat{G}}{\partial \hat{Q}}. \tag{3.16}$$

are the flux jacobian matrices. These flux jacobians and the viscous coefficient matrix $\hat{M}$, which comes from the time linearization of the viscous vector $\hat{S}^{n+1}$, are documented in Appendix A.

3.3.2 Pulliam-Chaussee Diagonal ADI Algorithm

Block tridiagonal-matrix inversions constitute the major portion of numerical work associated with the standard Beam-Warming algorithm. Equations (3.6) are a coupled set of 5 equations and thereby produce a (5×5) block-tridiagonal structure for the implicit operators of Eqs. (3.13). The diagonal version of the standard algorithm due to Pulliam and Chaussee [64] overcomes this difficulty. In this algorithm, rather than inverting block-tridiagonal matrices in each direction, scalar pentadiagonal matrices are inverted. This is computationally more efficient.

The Jacobian matrices, $\hat{A}$, $\hat{B}$ and $\hat{C}$ have a set of eigenvalues and a complete set of distinct eigenvectors. Similarity transformations can be used to diagonalize $\hat{A}$, $\hat{B}$ and $\hat{C}$,

$$\hat{A} = T_\xi \hat{\Lambda}_\xi T_\xi^{-1}, \quad \hat{B} = T_\eta \hat{\Lambda}_\eta T_\eta^{-1}, \quad \hat{C} = T_\varsigma \hat{\Lambda}_\varsigma T_\varsigma^{-1}. \tag{3.17}$$

where

$$\begin{aligned}\hat{\Lambda}_\xi &= D[U, U, U, U + c(\xi_x^2 + \xi_y^2 + \xi_z^2)^{1/2}, U - c(\xi_x^2 + \xi_y^2 + \xi_z^2)^{1/2}]\\ \hat{\Lambda}_\eta &= D[V, V, V, V + c(\eta_x^2 + \eta_y^2 + \eta_z^2)^{1/2}, V - c(\eta_x^2 + \eta_y^2 + \eta_z^2)^{1/2}]\\ \hat{\Lambda}_\varsigma &= D[W, W, W, W + c(\varsigma_x^2 + \varsigma_y^2 + \varsigma_z^2)^{1/2}, W - c(\varsigma_x^2 + \varsigma_y^2 + \varsigma_z^2)^{1/2}]\end{aligned} \tag{3.18}$$

where c is the speed of sound ($c^2 = \gamma p/\rho$), and for example $\hat{\Lambda}_\xi$ reads as

$$\hat{\Lambda}_\xi = \begin{bmatrix} U & 0 & 0 & 0 & 0 \\ 0 & U & 0 & 0 & 0 \\ 0 & 0 & U & 0 & 0 \\ 0 & 0 & 0 & U + c(\xi_x^2 + \xi_y^2 + \xi_z^2)^{1/2} & 0 \\ 0 & 0 & 0 & 0 & U - c(\xi_x^2 + \xi_y^2 + \xi_z^2)^{1/2} \end{bmatrix} \tag{3.19}$$

The similarity transformation matrices T_ξ, T_η, T_ς and their inverse matrices are given in Appendix B. Relations exist between T_ξ, T_η, and T_ς of the form

$$\hat{N} = T_\xi^{-1} T_\eta, \quad ,\hat{N}^{-1} = T_\eta^{-1} T_\xi, \quad \hat{P} = T_\eta^{-1} T_\varsigma, \quad ,\hat{P}^{-1} = T_\varsigma^{-1} T_\eta \tag{3.20}$$

where

$$T_k^{-1} T_l = \begin{bmatrix} m_1 & m_2 & m_3 & -\mu m_4 & \mu m_4 \\ -m_2 & m_1 & m_4 & \mu m_3 & -\mu m_3 \\ -m_3 & -m_4 & m_1 & -\mu m_2 & \mu m_2 \\ \mu m_4 & -\mu m_3 & \mu m_2 & \mu^2(1+m_1) & \mu^2(1-m_1) \\ -\mu m4 & \mu m_3 & -\mu m_2 & \mu^2(1-m_1) & \mu^2(1+m_1) \end{bmatrix} \tag{3.21}$$

$$m_1 = \tilde{k}_x \tilde{l}_x + \tilde{k}_y \tilde{l}_y + \tilde{k}_z \tilde{l}_z, \quad m_3 = \tilde{k}_x \tilde{l}_z - \tilde{k}_z \tilde{l}_x,$$
$$m_2 = \tilde{k}_x \tilde{l}_y - \tilde{k}_y \tilde{l}_x, \quad m_4 = \tilde{k}_y \tilde{l}_z - \tilde{k}_z \tilde{l}_y, \quad \mu = 1/\sqrt{2}.$$

After applying the similarity transformations of (3.17) and identities (3.20) in Eq.(3.13) and exchanging the smoothing operators with new ones, the diagonal form of the standard algorithm reads

$$\begin{aligned} &T_\xi (I + h\delta_\xi \hat{\Lambda}_\xi - hD_i|_\xi) \hat{N} (I + h\delta_\eta \hat{\Lambda}_\eta - hD_i|_\eta) \times \\ &\hat{P} (I + h\delta_\varsigma \hat{\Lambda}_\varsigma - hD_i|_\varsigma) T_\varsigma^{-1} \triangle \hat{Q}^n = R^n \end{aligned} \tag{3.22}$$

The spatial accuracy of the standard and diagonalized algorithms for steady-state problems (i.e. $\triangle \hat{Q}^n \to 0$ as $n \to \infty$) is determined by the type of differencing in forming $\hat{R}^n$. Since the modification that produces the diagonal algorithm does not effect $\hat{R}^n$, both schemes will have the same steady-state solution assuming that the steady-state solution is independent of the convergence path; i.e., that the steady state is unique. For constant coefficient matrices $\hat{A}$, $\hat{B}$ and $\hat{C}$, the diagonal algorithm reduces to the standard algorithm because the eigenvector matrices are also constant. Therefore, the linear stability analysis of Beam and Warming [63] also holds for the diagonal algorithm.

By numerical experimentation with the TNS code using both schemes, it was found that the diagonal algorithm performs much better in terms of convergence rates (see Flores [65]). To further enhance the convergence rate, two spatially varying $\triangle\tau$ schemes have been used.

$$\triangle\tau = \frac{\triangle t_{ref}}{\lambda_{max}}$$

and

$$\triangle\tau = \frac{\triangle t_{ref}}{1 + \sqrt{J}} \tag{3.23}$$

where J is the Jacobian of the coordinate transformation, λ_{max} is the maximum eigenvalue of the flux jacobians $\hat{A}$, $\hat{B}$ and $\hat{C}$, and $\triangle t_{ref}$ is a reference time step. The latter time stepping scheme proved to be better and was used throughout this study.

3.4 Boundary Conditions

Since the finite-difference scheme used in the TNS code is implicit, it might be expected that the boundary conditions would also be implicit. But the implementation of the implicit boundary conditions necessitates a modification of the inversion matrices which is not very practical. Moreover, past experience is such that explicit boundary conditions have been successfully employed in conjunction with the implicit codes. Also, explicit treatment of the boundaries leads to a simple and flexible scheme. Boundary conditions become a modular element that can be put in or pulled out of a computer program without touching the heart of the implicit code.

Unknown values of $\hat{Q}$ on the boundaries are updated explicitly, and this leads to a zeroth-order time extrapolation. The space extrapolations are either zeroth order or first order according to the physical and geometric constraints. Since in the TNS code a zonal approach is employed, there are two types of boundaries at which conditions must be specified: 1) the physical boundaries such as inflow, outflow, and body surface, and, 2) the zonal boundaries where "zones" are patched together. Treatment of zonal boundaries was presented in Chapter 2.

At the farfield boundaries, free-stream values are specified. This is shown in Fig. 12. At the upper boundary DC, lower boundary AB, side boundary EF, and inflow boundary AD, the conditions are free-stream, i.e., $\hat{Q} = \hat{Q}_\infty$. The conditions at the outflow boundary are found by a zeroth-order extrapolation from the last plane such that $\hat{Q}_{JMAX} = \hat{Q}_{JMAX-1}$. The symmetry plane boundary conditions are more complicated: Here a zeroth-order space extrapolation is used for the density. A first-order extrapolation is employed for the x-direction Cartesian velocity component u and z-direction Cartesian velocity component w, while the spanwise y-direction Cartesian velocity component v is set equal to zero to force symmetry. Pressure is also found by a first-order extrapolation and the total energy is computed using Eq. (3.4). At solid surfaces, the no-slip boundary condition is employed for the three velocity components. Surface pressure is found by using the boundary layer approximation $\partial p/\partial n \approx 0$ such that $p_1 = p_2$, where p_1 is the static pressure on the body surface, and p_2 is the static pressure on the first computational surface off the body. The surface density is found from an adiabatic wall assumption which yields $\rho_1 = \rho_2$. Total energy is computed using Eq. (3.4).

3.5 Artificial Dissipation Models

The numerical solution of the Euler/Navier-Stokes equations for flows involving captured shock waves necessitates the use of numerical or artificial dissipation either by using a scheme which is inherently dissipative or by using a nondissipative scheme with specially designed dissipative terms. The former class of schemes employ some form of upwind differencing under the assumptions of characteristic theory and wave propagation. The schemes due to Steger and Warming [67], Roe [68], Van Leer [69], Osher and Chakravarty [70] and Harten's TVD methods [71] all fall in this category. In this class of schemes, the dissipation is automatically included without user control. The basic ARC3D algorithm [62] used in the TNS code is of the second variety and consists of a centrally-differenced nondissipative scheme with user-controlled smoothing terms. The artificial dissipation is added for two reasons; first to control the odd-even decoupling of grid points typical of central differencing, and second to control strong nonlinear effects such as shocks.

It can be shown that upwind schemes are equivalent to central difference schemes with added dissipation. Pulliam[72] demonstrates that adding a fourth-difference dissipation to a central-difference scheme produces the equivalent of a second-order upwind scheme, whereas the use of a second-difference dissipation term produces a first-order upwind equivalent. There are different dissipation models utilized in the block and diagonal algorithms described earlier in Sec. (3.3).

The block algorithm which was given in Eq. (3.12) uses a constant coefficient dissipation model. In this approach, an explicit fourth-difference dissipation

$$D^{(4)}\hat{Q}^n = \epsilon_e \triangle\tau J^{-1}[(\nabla_\xi \triangle_\xi)^2 + (\nabla_\eta \triangle_\eta)^2 + (\nabla_\varsigma \triangle_\varsigma)^2] J\hat{Q}^n \qquad (3.24)$$

is added to the right-hand side of the equation and an implicit second-difference dissipation

$$D_k^{(2)} = -\epsilon_i J^{-1} \triangle_k \nabla_k J, \qquad k = \xi, \eta, \varsigma \qquad (3.25)$$

is inserted into the respective implicit block operators. Based on linear stability theory, the use of the explicit dissipation alone produces an explicit stability bound. If the second-difference implicit dissipation is added, the algorithm becomes unconditionally stable if ϵ_i is sufficiently large (cf. Ref. [28]). The procedure is to set $\epsilon_e = \triangle\tau$ and $\epsilon_i = 2\epsilon_e$ which results in a consistent definition of ϵ_e such that as the time step increases, the amount of artificial dissipation added relative to the spatial derivatives of convection and diffusion remains constant. This is because all of the convection and diffusion terms in the approximate factorization algorithm of the Eq. (3.13) are factored by the time step $\triangle t$. Instead of second-difference implicit dissipation, using fourth-difference implicit dissipation would improve convergence. However, this would require the inversion

of extremely expensive block pentadiagonal matrices rather than the relatively simple block tridiagonal matrices [72],[73].

The diagonal version of the implicit approximate factorization algorithm due to Pulliam and Chaussee, which was described in Sec. (3.3), substantially reduces this computational cost. The more appropriate fourth-difference dissipation terms can be added, and only require the inversion of scalar pentadiagonal matrices as opposed to block pentadiagonal matrices in the block algorithm. The diagonal algorithm was given by Eq. (3.22). The combination nonlinear dissipation operators are included as follows:

$$D_i|_\xi = \nabla_\xi(\sigma_{j+1,k,l}J^{-1}_{j+1,k,l} + \sigma_{j,k,l}J^{-1}_{j,k,l})(\epsilon^{(2)}_{j,k,l}\triangle_\xi - \epsilon^{(4)}_{j,k,l}\triangle_\xi\nabla_\xi\triangle_\xi)J \qquad (3.26)$$

The terms for $D_i|_\eta$ and $D_i|_\zeta$ have a similar form. The same dissipation model has been implemented in the right-hand explicit side of the algorithm. Hence the constant-coefficient fourth-difference dissipation operator $D^{(4)}$ in Eq. (3.13) is replaced by a combination nonlinear dissipation operator

$$D_e|_\xi = \nabla_\xi(\sigma_{j+1,k,l}J^{-1}_{j+1,k,l} + \sigma_{j,k,l}J^{-1}_{j,k,l})(\epsilon^{(2)}_{j,k,l}\triangle_\xi - \epsilon^{(4)}_{j,k,l}\triangle_\xi\nabla_\xi\triangle_\xi)J \qquad (3.27)$$

The dissipation operators defined by Eq. (3.24) and (3.25) include the metric Jacobian J so that they act upon the unscaled Q and not on $\hat{Q}$. Hence the dissipation is not directly influenced by the grid distribution because smooth functions of Q may occur in regions of rapid mesh variation. This form of smoothing operator is inspired by the recent work applying flux limiters to upwind schemes and TVD concepts which suggest that the best approach for an upwind algorithm is to use locally first-order upwind differences at the shock and second-order elsewhere[72]. This is accomplished by using switch operators $\epsilon^{(2)}_{j,k}$ and $\epsilon^{(4)}_{j,k}$ which govern the type of smoothing, e.g. second-difference smoothing near shocks and fourth-difference smoothing elsewhere. The term $\sigma_{j,k}$ is a spectral radius scaling which in three dimensions is defined as

$$\begin{aligned}\sigma_{j,k,l} = &|U| + a\sqrt{\xi_x^2 + \xi_y^2 + \xi_z^2} \\ &+ |V| + a\sqrt{\eta_x^2 + \eta_y^2 + \eta_z^2} \\ &+ |W| + a\sqrt{\zeta_x^2 + \zeta_y^2 + \zeta_z^2}\end{aligned} \qquad (3.28)$$

and is a sum of the spectral radii of the flux jacobians $\hat{A}$, $\hat{B}$ and $\hat{C}$. The interested reader is referred to Pulliam [72] for a good review of this subject. The effect of different smoothing models in the actual computations for the TNS code will be presented in Section (4.3).

3.6 Turbulence Model

Solving turbulent flows numerically is a very difficult task due to the extreme time and space scales associated with turbulent motion. Hence, the main method of approach in Computational Fluid Mechanics and Heat Transfer for solving turbulent flows is through the Reynolds averaged Navier-Stokes equations. Time or "Reynolds" averaging the equations of motion give rise to new terms which can be interpreted as "apparent" stress gradients and heat flux quantities associated with the turbulent motion. The apparent turbulent stresses in compressible flow can be written as [74]

$$(\tau_{ij})_{turb} = -\rho\overline{u_i' u_j'} \tag{3.29}$$

and the apparent turbulent heat flux components as

$$-(\nabla \cdot \mathbf{q})_{turb} = -\frac{\partial}{\partial x_j}(\rho c_p \overline{T' u_j'}) \tag{3.30}$$

In order to predict turbulent flows by applying finite-difference methods to the Reynolds equations, it is necessary to make assumptions for the terms in Eqs. (3.29) and (3.30). Boussinesq (1877) suggested that the apparent shearing stresses might be related to the rate of mean strain through an apparent turbulent or "eddy" viscosity given in incompressible flow by

$$-\rho\overline{u_i' u_j'} = \mu_T\left(\frac{\partial u_i}{\partial x_j} + \frac{\partial u_j}{\partial x_i}\right) \tag{3.31}$$

Closure for the Reynolds heat flux-term, $\rho c_p \overline{T' u_j'}$ is treated in algebraic models by a form of Reynolds analogy. The Reynolds analogy is based on the similarity between the transport of heat and momentum and applied to the apparent turbulent conductivity in the assumed Boussinesq form

$$\rho c_p \overline{T' u_j'} = -k_T \frac{\partial T}{\partial x_j} \tag{3.32}$$

Experiments reveal that the ratio of the diffusivities for the turbulent transport of heat and momentum which is called the turbulent Prandtl number, $Pr_T = \mu_T c_p / k_T$, is a well-behaved function across the flow and in algebraic models is generally taken to be 0.9. Using the turbulent Prandtl number, the turbulent heat flux is related to the turbulent viscosity and mean flow variables as

$$-\rho c_p \overline{T' u_j'} = \frac{c_p \mu_T}{Pr_T} \frac{\partial T}{\partial x_j} \tag{3.33}$$

Hence, in large scale Navier-Stokes computations an accurate and computationally efficient method of computing eddy coefficients is needed. Since the algebraic eddy viscosity models proved to be fairly accurate and computationally efficient, the Baldwin-Lomax algebraic eddy viscosity model [29] is utilized here. In the Baldwin-Lomax model the effects of turbulence are simulated by replacing the molecular coefficient of viscosity μ_M with the effective viscosity $\mu_M + \mu_T$ in the stress terms of the laminar Navier-Stokes equations. In heat flux terms $k/c_p = \mu/Pr$ is replaced by $\mu/Pr + \mu_T/Pr_T$.

The Baldwin-Lomax model is a two-layer algebraic model in which μ_T is given by

$$\mu_T = \begin{cases} (\mu_T)_{inner}, & y \leq y_{crossover} \\ (\mu_T)_{outer}, & y \geq y_{crossover} \end{cases} \tag{3.34}$$

where y is the normal distance from the wall and $y_{crossover}$ is the smallest value of y at which values from the inner and outer formulas are equal. The eddy viscosity coefficient in the inner layer is based on the Prandtl mixing-length theory

$$(\mu_T)_{inner} = \rho \ell^2 |\omega| \tag{3.35}$$

The parameter ℓ is the mixing length corrected with the Van Driest damping factor to account for the laminar sublayer

$$\ell = k\, y\, [1 - exp(-y^+/A^+)] \tag{3.36}$$

where $k = 0.4$, $A^+ = 26$, and $|\omega|$ is the magnitude of the vorticity given by

$$|\omega| = \sqrt{(u_y - v_x)^2 + (v_z - w_y)^2 + (w_x - u_z)^2} \tag{3.37}$$

and

$$y^+ = \frac{\rho_w u_\tau y}{\mu_w} = \frac{\sqrt{\rho_w \tau_w}\, y}{\mu_w} \tag{3.38}$$

The eddy viscosity coefficient in the outer layer is based on the distribution of vorticity which is used to determine the length scale and is given by

$$(\mu_T)_{outer} = K\, C_{CP}\, \rho\, F_{WAKE} F_{KLEB}(y) \tag{3.39}$$

where $K = 0.0168$ is the Clauser constant and $C_{CP} = 1.6$ is an additional constant. F_{WAKE} is found via

$$F_{WAKE} = min \left\{ \begin{array}{c} y_{max} F_{max} \\ or \\ C_{WK}\, y_{max} u_{DIF}^2 / F_{max} \end{array} \right\} \tag{3.40}$$

where $C_{WK} = 0.25$ and

$$u_{DIF} = (\sqrt{u^2 + v^2 + w^2})_{max} - (\sqrt{u^2 + v^2 + w^2})_{min} \tag{3.41}$$

In Eq. (3.41) the second term is taken to be zero (except in wakes). The quantities y_{max} and F_{max} are determined from the function

$$F(y) = y \mid \omega \mid [1 - exp(-y^+/A^+)] \tag{3.42}$$

In wakes the exponential term is set equal to zero. The quantity F_{max} is the maximum value of $F(y)$ that occurs in the profile and y_{max} is the value of y at which F_{max} occurs. The function F_{KLEB} is the Klebanoff intermittency factor given by

$$F_{KLEB}(y) = \left[1 + 5.5\left(\frac{C_{KLEB}y}{y_{MAX}}\right)^6\right]^{-1} \tag{3.43}$$

and $C_{KLEB} = 0.3$.

Although not seen explicitly, the Reynolds number enters into the computation of eddy viscosity through the computation of y^+. When the variables in Eq. (3.38) are nondimensionalized, the following expression is obtained:

$$y^+ = \sqrt{\frac{Re\ \tilde{\rho}_w \tilde{\tau}_w}{\tilde{\mu}_w}}\,\tilde{y} \tag{3.44}$$

In high Reynolds number flows, as $Re \to \infty$, the length scales l and $F(y)$ in the inner and outer layers go to zero, which result in vanishing values of μ_T. For more discussion on the Baldwin-Lomax turbulence model, the reader is referred to the original paper [29].

3.7 Computational Aspects of the Zonal Algorithm

So far the building blocks of the TNS program were presented: namely, the zonal algorithm, related data management and the numerical methods and flow models. It is very important to explore the characteristics of this code if it is intended to be used in routine flow simulations. The speed, convergence characteristics, efficiency and reliability of the code must be assessed.

The convergence rate of the diagonal version of the code (see Sec. 3.3.2) versus the block (standard) version (see Sec. 3.3.1) is shown in Fig. 13 (see Ref. [65]). The geometry used in this simulation was a NACA 0012 wing (see Fig. 9). The free-stream flow conditions were $M_\infty = 0.826$, $\alpha = 2°$ with a Reynolds number based on chord of 8 million. This is a moderately difficult case involving a strong shock with a moderate amount of separation. In Fig. 13, the abscissa

denotes the number of iterations for the algorithm, and the ordinate denotes the L2-norm of the residual. The time step used in the block version was $\triangle t = 0.004$, where a unit time interval denotes the time required by a particle moving at the free-stream speed of sound to travel one chord length. This was the largest time-step possible while still maintaining stability of the code.

The diagonal version used a variable time-step (see Eq. 3.23) and thus received convergence accelereration from this aspect. However, despite this, the main speed-up associated with the diagonal algorithm is not due to the variable time-stepping alone, but the variable time-step coupled with the correct implicit treatment of the numerical dissipation terms. Pulliam and Steger [73] reported that the variable time-step had often worked poorly in viscous flow until the second-order implicit dissipation terms were replaced by the fourth-order terms which are consistent with the fourth-order explicit dissipation of the right-hand side of the algorithm (see Eqs. 3.26 and 3.27). The same replacement is, of course, possible in the block algorithm, but would necessitate the inversion of expensive block pentadiagonal matrices.

The slow rate of convergence associated with the block scheme seems to occur in the outer zones. The viscous-zone block-scheme residual drops rapidly during the first 1000 iterations but then flattens out. At 5000 iterations, the residuals associated with all zones have dropped by about one to two orders of magnitude. In contrast, the convergence rate of the diagonal scheme drops rapidly in all zones. A three-order of magnitude drop in the L2-norm for a 150,000 grid point mesh occurs in 500 iterations which costs 2450 seconds of CPU time. This is equivalent to 4.9 seconds of CPU time per iteration and 3×10^{-5} seconds of CPU time per grid point per iteration. The convergence rate of the diagonal algorithm is nearly 40 times that of the original block algorithm. This is due to the proper linearization of the dissipation terms and variable time stepping as stated earlier, coupled with the decrease in arithmetic operation count owing to the diagonal algorithm.

The convergence characteristics of the algorithms as discussed above and other computational aspects of the TNS code were thoroughly explored by Flores [65]. It was concluded that: 1) although convergence rates are vastly different for different algorithms, the solution at steady state is not affected, 2) the use of explicit boundary conditions at zonal boundaries has no detrimental effect on the convergence characteristics of the algorithms, 3) there was no noticeable improvement in the convergence rate as a result of changing the extent of overlap between zones, and 4) use of different CFL values in different zones increases the convergence rate by 10-20%.

Data management of large application codes is an important issue which

must be handled carefully. Memory, speed and I/O(input/output) requirements of the TNS code are quite substantial. The key element for handling the memory and I/O requirements of the TNS code is the SSD (Solid State Device) of the NASA Ames Cray X-MP (see Sec. 2.4). The SSD has 16 million 64-bit words of memory. It will be instructive to give some statistics about how this code performs in actual situations, and in particular, how the data management of the metrics was achieved.

To exploit the ADI character of the flow solver algorithm, which necessitates implicit sweeps in all three directions, the metrics are transferred from SSD into main memory with three different orientations: $x-y$ planes, $x-z$ planes, and $y-z$ planes. Hence, there are three different copies of the metrics stored on the SSD corresponding to the three different orientations, which is not a problem because of the ample storage space in the SSD. However, the number of grid points for an adequate grid resolution is still limited by the capacity of the main memory (1 million 64-bit words on Cray X-MP). Each of the metric arrays is required in main memory several times for each grid zone during each iteration. This places extreme demands on I/O requirements. Nevertheless, the SSD handles these I/O requirements without a problem. The computational statistics displayed in Table 2 demonstrate this for two cases (M_∞ = 0.80 and 0.95 and $Re = 8 \times 10^7$, $\alpha = 5°$). The grid used for both calculations is similar to that presented in Fig. 8 and consists of four zones with a total of 166,621 grid points. As seen from Table 2, the higher Mach number case converges more slowly than the lower Mach number case. This is not surprising, since the $M_\infty = 0.80$ case is only moderately separated and the $M_\infty = 0.95$ case is massively separated. To advance a typical interior grid point in the TNS program one time level requires approximately 2030 floating point operations. Thus, for the cases displayed in Table 2, the TNS program execution rate on the Cray X-MP computer is about 63 MFLOPS (million floating point operations per second).

From the statistics in Table 2, the efficiency level associated with the SSD I/O is quantitatively established. During the $M_\infty = 0.95$ case, the program transfers almost 24 billion 64-bit words between the SSD and main memory using about a quarter of a million read/write requests. The I/O time charge for this case is just over two minutes. The estimated I/O time charge for this case, assuming disk is used to replace the SSD, is over 24 hours. (Because the I/O utilized in the TNS program is asynchronous, these I/O time charges represent only that portion of the I/O time that was not "covered up" by the CPU during execution.) For a detailed survey of the computational aspects of the TNS code, please refer to Ref. [75].

Table 2. Computational Statistics from the TNS Program
(NACA 0012 wing, $Re_c = 8 \times 10^7$, AR = 3.0, TR = 1.0, $\Lambda = 20°$)

Quantity	$M_\infty = 0.80$	$M_\infty = 0.95$
Iterations*	825	1890
CPU Time (Hrs)	1.25	2.82
Read/Write Requests (Memory/SSD)	110550	253260
64-Bit Words Transferred (MWDS)	10391	23806
SSD I/O Time (Sec)	61.5	140.8
Estimated Disk I/O Time (Hrs) (If disk had been used in place of SSD)	10.7	24.4

*Avg residual reduced three orders of magnitude (all grid zones).

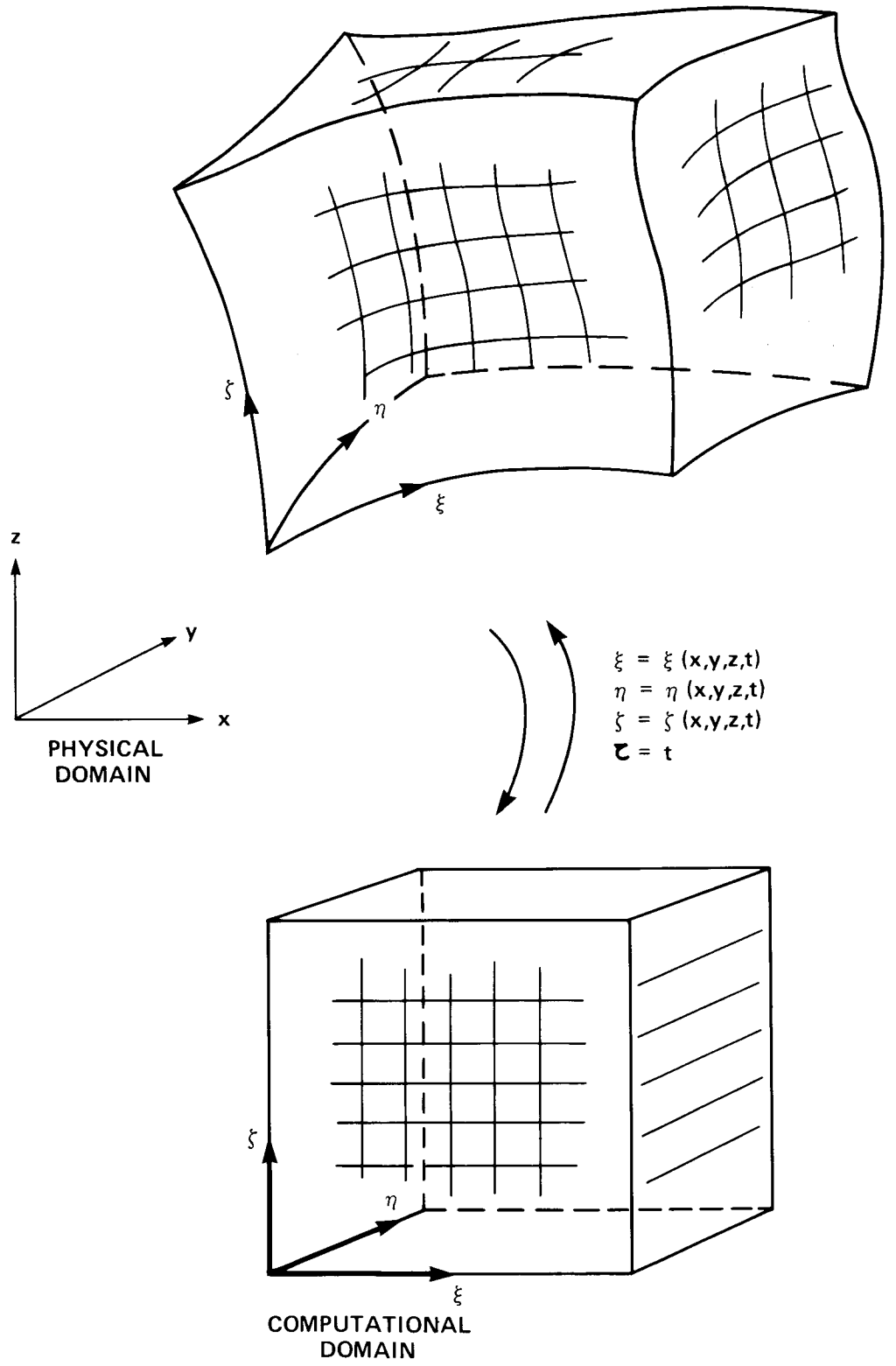

Fig. 11. General curvilinear coordinate transformation from physical to computational domain.

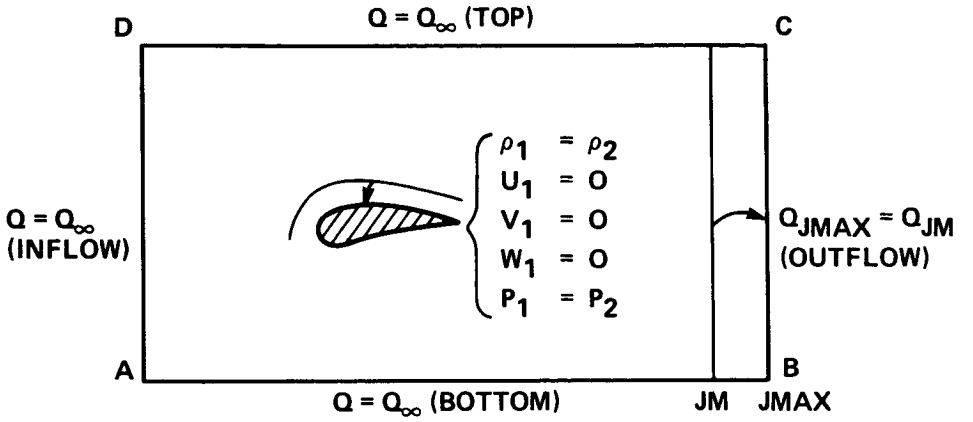

(a) X-Z PLANE (STREAMWISE CUT) OF THE CONTROL VOLUME

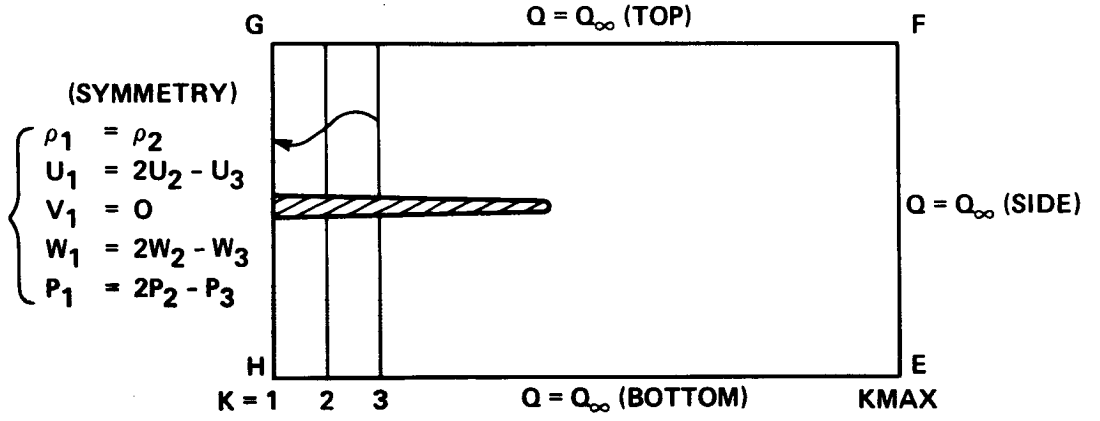

(b) Y-Z PLANE (SPANWISE CUT) OF THE CONTROL VOLUME

Fig. 12. Specification of the boundary conditions.

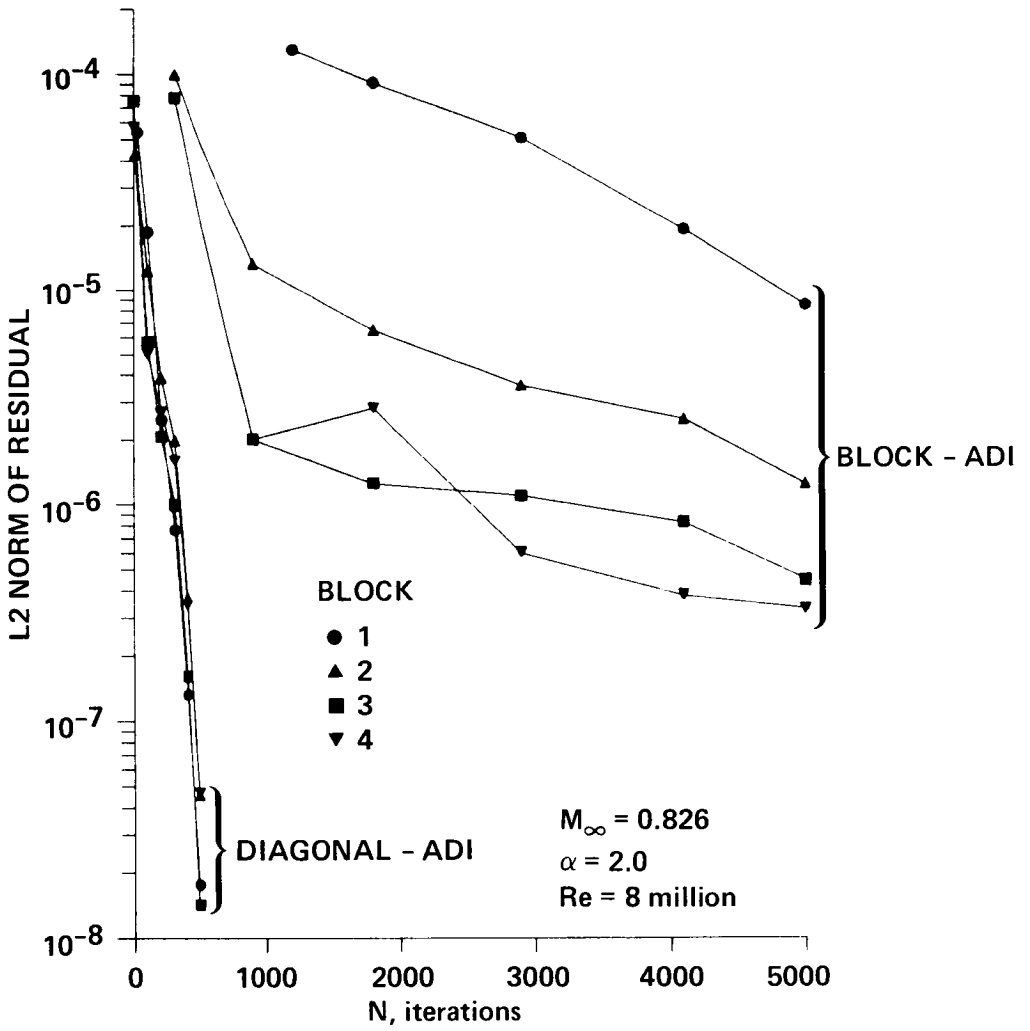

Fig. 13. The convergence rates of the diagonal ADI method and the block ADI (standard) method.

CHAPTER 4

SIMULATION OF WING FLOW FIELDS

4.1 Introduction

Understanding the nature of separated flows is important for an aircraft designer. If the aerodynamic design of a flight vehicle with flow separation is to be successful over the full range of flight conditions, the vehicle must be controllable at all times and possess no rapid changes in force and moment characteristics. Lifting surfaces such as wings, canards, strakes, etc., play an important role in the design process. Accounting for separated flows about these surfaces is one of the most crucial tasks of the aerodynamic design. Designers either want to reduce the adverse effects of separation, or exploit separation for useful purposes. The latter, for instance, is the case for a rolled-up vortex sheet from the sharp leading edge of a delta wing or a strake of a fighter aircraft, in which case the vortex provides so-called "nonlinear lift."

Our present understanding of three-dimensional separation about wings comes principally from flow visualization experiments with surface-oil techniques in wind tunnels, smoke tunnels, and dye flow in water tunnels. However, there have also been some attempts to compute separated flows on wings in recent years. Numerical simulations of the leading edge vortex phenomenon associated with a delta wing have been made using potential flow procedures such as panel methods or vortex lattice methods [76],[77]. Other researchers have used the Euler equations to solve the same problem [78],[79],[80],[81]. For a discussion about the prediction of separation, which is a viscous phenomenon, using the Euler equations, see Ref. [82].

Another technique used in the computation of separated flows is based on viscous-inviscid interaction methods (see Sec. 1.2). These methods are quite appropriate for computing mild separations but, at present, tend to break down for large streamwise separations. Some progress has been made on computing turbulent flows over wings primarily using integral boundary layer schemes, but these schemes cannot easily compute separated flows [42],[43],[44].

Because of the shortcomings of the methods described in the previous paragraph, the Navier-Stokes equations seem to be the proper model equations for computing massively separated flows on wings [40]. This line of research is quite recent, with only a few publications on the subject. The computation of the

supersonic flow over a blunt delta wing by Vigneron et al. [83], the leading-edge separation vortex over a delta wing at high angle of attack by Fujii and Kutler [39], and the simulation of a tip vortex off a low-aspect-ratio wing at a transonic speed by Mansour [34] are a few examples. Also very recently, transonic wing solutions have emerged due to Agarwal and Deese [37], Vadyak [84] and Holst et al. [45].

In this chapter, the computational aspects of the TNS zonal algorithm are presented, and then the mathematical and topological considerations of separated flows will be discussed to better understand them. After this, the impact of the artificial dissipation and turbulence models on separated flow will be demonstrated. Finally, the simulation of two low-aspect-ratio wings will be presented and comparisons will be made where data are present.

4.2 Mathematical and Topological Considerations

4.2.1 Background

The character of a flow near a surface, to a large extent, can be inferred from the surface pattern or "skin-friction lines" which are the lines everywhere parallel to the wall shear stress vectors. The pattern of skin friction lines can often be approximately determined by the experimental oil-flow technique [85]. However, the thickness of the oil film plays an important role in the appearance of the resulting oil-flow pattern. If the film is thick and accumulates in certain regions of the surface, it may lead to misconceptions (private communication with Dean Chapman, 1984).

Although the definition of separation and reattachment is well established in two-dimensional steady flows by the existence of a reverse flow, a straightforward extrapolation of two-dimensional concepts to three-dimensional flows is not possible. In three-dimensions, the meaning of the term "reverse" becomes ambigious. Our present understanding of three-dimensional separation stems essentially from flow-visualization experiments. If, for instance, a surface oil-flow technique is used, Tobak and Peake [86] indicate that the convergence of oil-streaks onto a particular line is a necessary condition for three-dimensional separation. But, whether this is also a sufficient condition is a topic of current debate.

Maskell [87] discussed the global structure of three-dimensional flows in qualitative terms, calling the pattern of limiting streamlines (the streamlines very close to the surface which lie closely along the skin-friction lines) the "skeleton" of the entire flow field. A precise mathematical framework to conceptualize the pattern of "limiting streamlines" was proposed by Legendre [88] in which the

limiting streamlines were considered to possess the properties of a continuous vector field. One principal property is that only one limiting streamline can pass through a regular (that is, nonsingular) point in the flow field. On the basis of this hypothesis, the elementary singular points of the field can be categorized mathematically (see Sec. 4.2.2). Then, the types of singular points, their number and the rules governing the relations between them can be said to characterize the pattern.

In this context, three-dimensional separation has been defined by the convergence of skin-friction lines onto a particular skin-friction line that originates from a singular point of particular type, the saddle point [85],[86]. However, this may not be the only possibility. Under given circumstances, it appears that a separation line may also emanate from a nodal-type singular point [86]. The issue was clarified more concisely by Lighthill [85] by tying the postulate of a continuous vector field to the pattern of skin-friction lines on the three-dimensional body rather than to the limiting streamlines just above the surface. There are two advantages to working with the skin-friction lines: 1) they are defined uniquely everywhere on the surface, even in the vicinity of lines of separation, which are themselves skin-friction lines, and 2) with skin-friction lines being defined uniquely everywhere on the surface, the pattern of skin-friction lines can be viewed as a continuous vector field.

4.2.2 Mathematical Foundations for the Skin-Friction Field

In order to examine the conditions for separation and behaviour of critical points, it is necessary to consider the wall shear stress field. Skin-friction lines are defined as the integral curves of the wall shear stress vector exerted by the fluid on the wall. If at any point the wall shear stress vanishes, the field possesses a saddle or a nodal point, at which the skin-friction lines' directions are indeterminate. The "phase-plane" and "phase-space" methods of exploring the properties of solutions of ordinary differential equations have proved to be extremely successful in the field of nonlinear dynamical systems. Oswatitsch [89], and Lighthill [85] examined viscous flow patterns close to a rigid boundary and classified certain classical points which can occur. They used a mathematics which is equivalent to the phase-plane trajectory analysis. Also Perry and Fairlie [90] and Hornung and Perry [91] applied these techniques to fluid flow problems. The following analysis outlines the mathematical procedure for the topography of skin-friction lines and critical points. In the analysis, cartesian coordinates are assumed for demonstration purposes, however the same conclusions could be drawn if the curvilinear coordinates were used.

The system of equations for particle paths in a steady flow is given by

$$\begin{aligned} \frac{dx}{dt} &= u(x,y,z) \\ \frac{dy}{dt} &= v(x,y,z) \\ \frac{dz}{dt} &= w(x,y,z) \end{aligned} \tag{4.1}$$

where x, y, and z are Cartesian coordinates and u, v, and w are the Cartesian velocity components along x, y, and z respectively (see Fig. 14). The skin-friction lines, or limiting streamlines, are obtained by exploring the limiting behavior of Eqs. (4.1). But because of the no-slip boundary condition at the wall, Eqs. (4.1) are trivial (i.e. $u = v = w = 0$, as $z \to 0$). At this point, it is helpful to introduce a pseduo-time $d\tau$ such as

$$d\tau = z\, dt \tag{4.2}$$

Rewriting, Eqs. (4.1) yield

$$\begin{aligned} \dot{x} &= \frac{dx}{d\tau} = \frac{u}{z} \\ \dot{y} &= \frac{dy}{d\tau} = \frac{v}{z} \\ \dot{z} &= \frac{dz}{d\tau} = \frac{w}{z} \end{aligned} \tag{4.3}$$

It is necessary to analyze the limiting behavior of the shear-stress tensor given in Eq. (3.3). At the surface, the following conditions for the velocity components and their derivatives hold:

$$\begin{aligned} u = v = w &= 0 \\ u_x = u_y = v_x = v_y = w_x = w_y &= 0 \end{aligned} \tag{4.4}$$

but from the continuity equation, $w_z = 0$ also. Hence Eqs. (3.3) reduce to

$$\begin{aligned} \tau_{xx} = \tau_{yy} = \tau_{zz} = \tau_{xy} &= 0 \\ \tau_{xz} &= \mu \frac{\partial u}{\partial z} \\ \tau_{yz} &= \mu \frac{\partial v}{\partial z} \end{aligned} \tag{4.5}$$

Taking the limits as $z \to 0$ for the last two of the preceeding equations yields

$$\begin{aligned} \frac{u}{z} &= \frac{\tau_{xz}}{\mu} = f(x,y) \\ \frac{v}{z} &= \frac{\tau_{yz}}{\mu} = g(x,y) \end{aligned} \tag{4.6}$$

or

$$\frac{\mathbf{u}}{z} = \frac{\tau_w}{\mu} \tag{4.7}$$

in which $\mathbf{u} = (u,v)^T$, $\tau_w = (\tau_{xz}, \tau_{yz})^T$ where the superscript T denotes the transpose of a matrix, and $f(x,y)$ and $g(x,y)$ are nonlinear functions.

It is assumed that, for steady flow of an incompressible Newtonian fluid with constant viscosity at finite Reynolds number over a smooth continuous wall, the velocity and pressure are regular, so that local solutions can be written as Taylor series expansions in the space coordinates. The mathematical support for this assumption is discussed by Ladyzhenskaya [92]. Eq. (4.7) reveals that the vector quantity $\mathbf{u}/z$ is equal to τ_w/μ, and the vector field $\mathbf{u}/z$ has the same integral curves as the wall shear stress; i.e., the skin-friction lines. When $\mathbf{u}/z$ is expanded into a Taylor series about the critical point, and only the lowest order terms are retained, the following linear system of first-order ordinary differential equations is obtained:

$$\begin{bmatrix} \dot{x} \\ \dot{y} \end{bmatrix} = \begin{bmatrix} a & b \\ c & d \end{bmatrix} \begin{bmatrix} x \\ y \end{bmatrix} \tag{4.8}$$

or

$$\dot{\mathbf{x}} = \mathbf{F} \cdot \mathbf{x} \tag{4.9}$$

The matrix $\mathbf{F}$ of Eq. (4.9) has eigenvalues λ_1 and λ_2 which may in general be real or complex. The corresponding eigenvector slopes are

$$\begin{aligned} m_1 &= (\lambda_1 - a)/b = c/(\lambda_1 - d) \\ m_2 &= (\lambda_2 - a)/b = c/(\lambda_2 - d) \end{aligned} \tag{4.10}$$

which, for the case of λ_1 and λ_2 real, may be shown to correspond to the slopes of certain trajectories which emanate from the critical points.

There is just one skin-friction line through each point on a surface, except for a point of separation or attachment, where $\tau_w = 0$. These points are the singular points of the differential equations governing the topography of the skin-friction lines. Such singular points are classified (see Kaplan [93]) depending on the values of the following quantities:

$$\begin{aligned} p &= -(a + d) = -trace\,\mathbf{F} \\ q &= (ad - bc) = det\,\mathbf{F} \end{aligned} \tag{4.11}$$

and

$$\lambda_{1,2} = -\frac{1}{2}[p \mp (p^2 - 4q)^{1/2}] \tag{4.12}$$

The classification of possible critical points is shown in Fig. 15 from Ref. [90]. A singular point where $q < 0$ is a "saddle point"; a point where $q > 0$, however, is

a "nodal point." A nodal point (Fig. 15a) is a point where all of the skin-friction lines except one (labeled AA in Fig. 15) are tangential to a single line BB. A focus (Fig. 15b) differs from a nodal point in that it has no common tangent line. An infinite number of lines spiral around the singular point, either away from it (a focus of attachment) or into it (a focus of separation). At a saddle point (Fig. 15c), only two particular lines, CC and DD, pass through the singular point. The flow directions on opposing sides of the singular point are inward on one particular line and outward on the other line. All of the other lines pass by the singular point in directions consistent with the directions of the adjacent particular lines. Critical points corresponding to values of p and q along the axes ($p = 0$ and/or $q = 0$) and on the parabola $p = 4\,q^2$ are "degenerate" forms.

4.2.3 Topography of Skin Friction Lines

Singular points have certain characteristics that largely determine the distribution of skin-friction lines on the surface. The nodal point of attachment is typically a stagnation point on the forward face of the body, where the free-stream attaches itself to the surface. Hence the nodal point of attachment behaves like a source from which the skin-friction lines issue and circumscribe the body. The nodal point of separation, however, behaves like a sink where the skin-friction lines on the body surface terminate. In other words, this is the rear stagnation point of the body. The saddle point acts typically to divide the skin-friction lines issuing from these nodes. The total number of singular points for a possible pattern on a smooth surface is subject to a topological rule that the number of nodal points must exceed the number of saddle points by 2 (see Kaplan [93]). A physical explanation for this is due to Lighthill [85]: since there are infinite number of skin-friction lines on the surface, and they must begin and end somewhere, there is at least one nodal point of attachment and one nodal point of separation. If there are two nodal points of attachment, however, the skin-friction lines from each node must somewhere run into each other; this necessitates an introduction of a saddle point in between them.

Figure 16 shows such a combination of two nodal points of attachment and one saddle point of separation. If there are n nodal points of attachment, there will be $(n-1)$ saddle points accordingly. Hence the whole combination is equivalent to a single node of attachment which behaves like a "source" as explained before. Similarly, m nodal points of separation and $(m-1)$ saddle points behave like a "sink" into which the skin-friction lines emanating from the "source" vanish. Therefore, there are $(m+n)$ nodal points and $(m+n-2)$ saddle points, and the topological law is satisfied. A particular skin-friction line emerging from a saddle point prevents the lines from the nodal points of attachment from crossing each other. This particular skin-friction line is called a line of separation. Skin-friction lines from either side asymptotically converge on the line of separation.

Hence, it is possible to define the line of separation as a particular skin-friction line toward which other skin-friction lines converge rapidly (in an asymptotic manner, but not a cusp-like manner, c.f. [85],[90]); conversely, a line of reattachment is defined as a particular line from which other skin-friction lines diverge rapidly. It should be kept in mind that this definition is associated with the *necessary* condition of the separation. Whether it is also *sufficient* is a matter of current debate [86].

In the vicinity of the line of separation, the limiting streamline must leave the surface. This can be shown as follows: at a very small distance z from the surface the velocity was found in Eq. (4.7)

$$\frac{\mathbf{u}}{z} = \frac{\tau_w}{\mu}$$

Continuity must be satisfied in a streamtube, for which the volume flow rate $\dot{M}$ is expressed as

$$\dot{M} = z\, d\, \frac{q}{2} = const. \tag{4.13}$$

where d is the distance between the streamlines and $q = |\,\mathbf{u}\,|$. From Eq. (4.7)

$$q = \frac{1}{\mu}\, z\, \tau_w \tag{4.14}$$

where $\tau_w = |\,\boldsymbol{\tau}_w\,|$. From Eqs. (4.13) and (4.14)

$$z \approx (d\,\tau_w)^{-1/2} \tag{4.15}$$

Hence, the height of the limiting streamline z above the surface grows rapidly as the line of separation is approached. According to Eq. (4.15), the mechanism which causes the limiting streamlines to leave the surface is twofold: first, the resultant skin-friction τ_w becomes vanishingly small near the saddle point, and second, the distance d between the adjacent limiting streamlines, falls rapidly as the limiting streamlines converge toward the line of separation.

In the remaining parts of this section, a series of attached and separated flow computations will be presented. The methodology of studying these flows will be from three points of view: 1) the actual phenomena (i.e., the experimental flow pictures), 2) the "conceptualization" or the "postulation" of these pictures in light of topological laws and rules, and 3) the computations. In any kind of interpretation, these three topics must support each other to provide a plausible explanation. The surface phenomenon is very important because the three-dimensional flow field above the surface depends on the surface flow. For instance, three-dimensional stream surfaces emerge from the separation lines,

whereas rolled-up vortex sheets emanate from spiral separation nodes, i.e. the foci on the surface. However, the three-dimensional separation phenomenon is very complex and a given surface pattern can produce many three-dimensional flow patterns depending upon interpretation. Dallmann [94] explains with examples that there is no unique relationship between the pattern of wall streamlines and the flow field above the wall. He adds that topologically different flow fields may exhibit the same oil-flow picture.

4.3 Effects of Artificial Dissipation and Turbulence Models

Turbulence and artificial dissipation models play crucial roles in the simulation of separated flows and shock/boundary layer interactions. Since there is an intimate relation between the skin friction field and flow separation, correct computation of boundary layers is very important. In order to assess the relative effects of these models on the boundary layer characteristics, a series of test cases has been computed for attached and shock-induced separated flows.

4.3.1 Effects of Artificial Dissipation

The impacts of artificial dissipation schemes are firstly investigated for an attached airfoil flow. The test case consists of a two-dimensional flow around a NACA 0012 airfoil at $M_\infty = 0.5$, $Re = 2.89 \times 10^6$ and $\alpha = 0°$. The TNS program was run for a very large aspect ratio wing making the flow at the symmetry plane essentially two-dimensional. The computed and experimental pressure coefficent distributions are compared in Fig. 17. The experimental data is taken from Thibert et al. Ref. [95]. The agreement for this admittedly easy case is very good in terms of pressure.

In Fig. 18, the turbulent boundary layer profiles computed by TNS, using different smoothing models and algorithms, are compared with those of an another CFD code, called TRIVIA. Ideally, the computed boundary layer profiles should be compared with the experimental ones. However, this is not an easy task because of the lack of experimental profile data. An alternative is to compare the computed profiles against those of another "proven" CFD code. For this purpose, the transonic airfoil interaction code of Steger and Van Dalsem [96], called "TRIVIA" was chosen. TRIVIA utilizes the same turbulence model as TNS and proved to be very accurate for a fairly broad range of airfoil flow conditions.

The y^+ values of the first grid points off the surface were about 1 or 2 for TRIVIA and 2 or 4 for TNS. One remarkable feature of this comparison is that although all methods give the same C_p distribution, the computed TNS boundary layer profiles using the diagonal algorithm of Section 3.3.2 are significantly less

full than either TRIVIA or TNS-block-algorithm boundary layer profiles. The TNS diagonal algorithm utilizes a nonlinear artificial dissipation model, while the block algorithm uses a constant coefficient artificial dissipation model. The discrepancy between the results may be explained as follows: the amount of artificial dissipation must be large enough to keep the algorithm stable, yet small enough not to excessively damp the flow physics. The nonlinear smoothing used in the diagonal algorithm was specifically designed for inviscid calculations [97]. Using this algorithm in Navier-Stokes calculations produces too much smoothing in the boundary layer. This is because the spectral radius $\sigma_{j,k,l}$ used in Eq. (3.27) is in the order $\triangle\zeta^{-1}$, and since the normal grid spacing $\triangle\zeta$ is very small in the viscous boundary layer, $\sigma_{j,k,l}$ becomes very large. This problem may be resolved by forcing the artificial viscosity to zero near solid boundaries. The nonlinear explicit smoothing terms of the diagonal algorithm given by Eq. (3.27) is modified to

$$D_e|_\xi = \nabla_\xi f(M)(\sigma_{j+1,k,l}J^{-1}_{j+1,k,l}+\sigma_{j,k,l}J^{-1}_{j,k,l})(\epsilon^{(2)}_{j,k,l}\triangle_\xi-\epsilon^{(4)}_{j,k,l}\triangle_\xi\nabla_\xi\triangle_\xi)J \quad (4.16)$$

where

$$f(M) = \begin{cases} M^2, & \text{for attached flows} \\ M, & \text{for separated flows} \end{cases} \quad (4.17)$$

and M is the local Mach number. The suggested linear and quadratic variations of Mach number depending upon the type of flow was found experimentally. However, this reflects the fact that the amount of artificial dissipation in a separated flow should be larger than its counterpart in an attached flow. This is to secure the numerical stability of the algorithm. Utilizing this concept proved to be very helpful, as evidenced in Fig. 19 where the modified dissipation model results compare favorably with the original TRIVIA results.

Since the modified smoothing algorithm changes the boundary layer, it is expected that the skin-friction field, and consequently the separation characteristics, will also change. Therefore, another test case was set up to simulate a separated flow. The impact of the artificial dissipation, as well as the impact of the turbulence model, will be investigated on this flow. This case involves a transonic flow field about a NACA 0012 section wing with an aspect ratio of 3.0, a taper ratio of 1.0, 20° of sweep, a Reynolds number based on chord of 8 million, a free-stream Mach number of 0.826, and an angle of attack of 2°. The solid wind tunnel walls, which are modeled in this calculation (see Fig. 8), are slightly less than 2 chords above and below the wing. This case corresponds to the experimental work of Lockman and Seegmiller [61], and a comparison of the numerical results with this experiment follows.

The surface pressure coefficent distributions at three selected spanwise locations are compared in Fig. 20. It is seen that the free-air shock position is in error by approximately 10% of chord, and inclusion of wind tunnel wall effects has shifted the shock downstream, in good agreement with the experiment. Also, the pressure plateau downstream of the shock, which signifies the shock induced separation, was not reproduced due to the turbulence model. Note also that general agreement between the wind tunnel simulation and experiment is better inboard of mid-semispan than it is outboard.

The emphasis of this work is on flow separation. In Fig. 21, an oil flow photograph taken from the experiment of Lockman and Seegmiller [61] shows the complexity of the phenomenon. In order to analyze and comprehend the separated flows, postulation of the skin friction lines is very helpful. The reader is reminded that Maskell [87] called the skin-friction lines the "skeleton" of the entire flow field (see Sec. 4.2.1). The author's depiction of the skin friction lines for the flow of Fig. 21 is presented in Fig. 22 to facilitate a possible correlation between the oil flow photograph and the numerical simulations. The oil-flow photograph displays a very interesting skin-friction map typical of transonic separated flows. A strong swept shock wave extends almost over the entire span of the wing, and induces flow separation over two-thirds of the span. The swept shock wave is especially strong in the outer one-half of the span and causes a "mushroom-type" separation zone. In this zone, two counter-rotating vortices are separated by a saddle point, as necessitated by the rules for skin-friction line topography (see Sec. 4.2.3, and also Lighthill [85]). In addition to this interesting feature, two nodal points of separation, one nodal point of attachment and three other saddle points are recognized in Fig. 22. This skin-friction map seems to be plausible since no topological rule is violated. For instance, no saddle-point-to-saddle-point connection, which was shown to be structurally unstable [98] occurs, nor is there a nodal-point-to-nodal-point connection without a saddle point between them (see Fig. 16).

The computed very-near-surface particle paths, or skin-friction lines, which resemble the oil flow pattern of the experiment are presented in Figs. 23 and 24. The pattern in Fig. 23 was computed using the diagonal algorithm with the standard nonlinear smoothing. This simulation does compare well in terms of the extent of the separation region, which has been underpredicted. Indeed, the experimental separation is more than twice as large as the computed one. The pattern in Fig. 24, however, was produced using the same algorithm but with modified smoothing. The modified explicit nonlinear smoothing coefficient given by Eq. (4.16) was employed, and $f(M) = M$ was used as suggested by Eq. (4.17). Note that the result of Fig. 24 is in better agreement with the experiment as indicated by the larger spanwise extent of the separation bubble. Although there is improvement, topologically Figs. 23 and 24 are the same; both have one

nodal point of separation and one saddle point. The nodal point is on the line of separation and the saddle point is on the line of reattachment.

4.3.2 Effects of Turbulence Model

The turbulence model also has important effects on the surface pattern. The Baldwin-Lomax model, which is an equilibrium model, predicts too sharp an increase in the outer layer eddy viscosity through the separation shock [99]. The increase of eddy viscosity from its local equilibrium value far from the wall leads to more turbulent mixing and to more shear stress to balance the adverse pressure gradient, suppressing the tendency toward separation. Rotta [100] concluded from experimental data that when turbulent flow is perturbed from its local equilibrium state, a distance of about one order of magnitude greater than the boundary layer thickness is required to attain a new equilibrium state. To account for the upstream turbulence history effects, Shang and Hankey [101] used a relaxation eddy viscosity model, i.e.,

$$\mu_T = \mu_{T_{eq}} - (\mu_{T_{eq}} - \mu_{T_0}) exp\left(-\frac{x - x_0}{\lambda}\right) \tag{4.18}$$

which was applied on the $y = const.$ lines, where μ_T is the turbulent dynamic eddy viscosity, $\mu_{T_{eq}}$ is the local equilibrium eddy viscosity evaluated from Eq. (3.34), μ_{T_0} is the eddy viscosity at upstream location x_0, and λ is the relaxation length. A good review of turbulence model relaxation techniques can be found in Hung [99]. Conceptually, Eq. (4.18) approximates the experimental observation that, in an abrupt disturbance of a turbulent flow, the Reynolds stress remains nearly frozen at its initial value while it is being convected along streamlines, and then exponentially approaches a new equilibrium state. In a numerical calculation, the initial location of the disturbance from which the relaxation process is initiated, x_0, and a relaxation length scale which describes the exponential decay of the eddy viscosity distribution, λ, must be specified. There are two limiting cases which bound the relaxation length. For $\lambda = 0$, the turbulent eddy viscosity equals the local equilibrium value, and for $\lambda = \infty$, the initial value μ_{T_0} is frozen and is used everywhere in the region $x > x_0$.

The relaxation turbulence model has been applied to the separated flow case in the previous comparison. Varieties of λ values were tried, and $\lambda = 40\,\delta_0$ was found to give a good agreement with the experimental pressure coefficient distribution as well as with the skin-friction field. Here δ_0 is the thickness of the boundary layer at x_0. The resulting computed skin-friction field for the case discussed in Figs. 21-24 is presented in Fig. 25. As seen from the figure, the streamwise separation is somewhat substantially increased; in fact, it is somewhat overpredicted. Also the location of the separation bubble is more inboard than the experimental one, but this may be due to insufficient tip resolution in

the computational grid. The remarkable feature of Fig. 25, however, is that it reproduces the dominant feature of the experiment, that is, the mushroom-shaped separation zone. This feature was lacking in the Figs. 23 and 24. In Fig. 25, although the experiment shows two foci on each side of the saddle point, the computation predicts two nodal points of separation. This is topologically acceptable, although not accurate, because a node and a focus are topologically equivalent (see Fig. 15). The saddle point on the reattachment line was also predicted by the computation.

The impact of the relaxation turbulence model on the pressure coefficient is displayed in Figs. 26 and 27. In Fig. 26, several sectional pressure coefficients are shown across the separation zone. The solid line shows the relaxation turbulence model and dashed line shows the equilibrium turbulence model. Figure 26 reveals that the equilibrium model predicts strong shock waves which more closely resemble the shocks captured in inviscid flow models. The relaxation model, however, predicts the pressure plateau downstream of the shock due to the shock-induced separation. Another feature of the comparison is that the shock wave system of the relaxation model moved slightly forward relative to that of the equilibrium model. Nevertheless this is not totally unexpected. The displacement thickness δ^* of the boundary layer increases due to the shock-induced separation. This portion of the boundary layer acts like a wedge which displaces the shock wave system forward. In Fig. 27, computations from the two turbulence models are compared with experiment. The computed shock positions are somewhat forward of the experimental ones. However, it is remarkable that the pressure plateau predicted by the relaxation model is very close to the experimental one in Fig. 27b. On the other hand, the equilibrium model does not predict such a phenomenon.

There are several things to keep in perspective when interpreting the discrepancy between the experiment and computation. One of the main problems is, of course, the turbulence modeling, as was proven by the improved prediction of the pressure plateau by using a simple relaxation model. Another significant factor in comparing the computation and experiment is that the experiment may need Mach number and angle of attack corrections, a common requirement when comparing with experimental data. Thirdly, the tip resolution in the TNS program is still poor which may be responsible for the inaccuracy of the location of the separation zone. Finally, it is known that prescribing wind-tunnel exit pressure in the computations is useful for predicting the extent of separation and the shock location [23]. Much improved results would be expected if these sources of error were eliminated. In the future, a more detailed study will be made with much finer grid resolution using more powerful machines together with a better turbulence model. Nevertheless, in this stage, it should be emphasized that the relaxation turbulence model was applied to the computation of three-dimensional

separated flows on wings for the first time, and improvements were observed in the skin-friction topography as well as the pressure coefficient of a low aspect ratio wing.

In the remaining parts of this chapter, two low aspect ratio wings will be studied. Of these wings, the first one is an advanced technology wing called "WING C," and the other wing is a rather simpler wing with NACA 0012 airfoil cross-sections. The flow topology on these wings will be thoroughly investigated by running many cases and comparing with the experimental data when they are available. The techniques developed in this section were not employed on these cases presently. However, in the future, as was explained in the previous paragraph, an attempt will be made to rerun these cases with higher grid resolution and better turbulence model. For the present, the aforementioned limitations should be kept in perspective when interpreting the results.

4.4. Simulation of WING C Flow Fields

4.4.1 WING C Design and Testing

In recent years, there have been significant efforts to compute flow fields around wings in the transonic regime. Consequently, it is important to assess the accuracy of these computations by comparing them with reliable experimental data. NASA Ames Research Center and the Lockheed-Georgia Company contributed to this effort by conducting a cooperative computational and experimental investigation of an advanced technology wing, called "WING C" (Fig. 3). The designers of WING C, R. Hicks of Ames Research Center and B. L. Hinson of Lockheed-Georgia, used two existing computer codes: FLO22 [102], a three-dimensional full potential equation solver and a numerical optimization program based on the Method of Feasible Directions [103]. A highly swept, low-aspect-ratio wing was selected that had supercritical airfoils with relatively thick sections, moderate aft loading, mild shock waves, and a mild pressure recovery. The mild shock wave was accomplished by limiting leading edge local Mach numbers to maximum of 1.2 to the leading edge. The design conditions selected were a Mach number of 0.85 and a lift coefficient of about 0.5, at an angle of attack of 5°.

A small-scale 0.261 meter semispan model of WING C was tested in the Lockheed-Georgia Wind Tunnel (CFWT), which has a ($0.508 \times 0.712m.$) test section. The test Reynolds number based on the mean aerodynamic chord was 10 million. Surface pressures were measured both on the wing and on wind-tunnel walls for comparison with calculations of wall effects. The small-scale model data are presented in Ref. [104], and a comparison of these measurements with several three-dimensional transonic inviscid codes is presented in Refs. [105]

and [106]. The top and side walls of the three-dimensional test section have a variable porosity capacity of up to 10%. Most of the wind tunnel testing was conducted at a fixed wall porosity of 4 percent for minimum wall interference effects. The influence of the wind tunnel walls on the test data was explored and a Mach number correction of $\triangle M = -0.005$ was found necessary. An angle of attack correction of $\triangle\alpha = 0.9°$ was also needed in the experiments to match the computations. The method of matching leading-edge pressures was used to select an experimental angle of attack of 5.9°, for which the experimental and computed (FLO22 code, with $\alpha = 5°$), leading-edge pressures agreed. Transition strips were located at a fixed distance from the leading edge equal to 5% of the mean aerodynamic chord on both the upper and lower surfaces of the wing.

A series of tests with the WING C was also performed by NASA Ames Research Center as a part of the cooperative effort. For the Ames tests [107], a large-scale 0.90 meter semispan model was tested in a (1.8 × 1.8 m.) wind tunnel. Model blockage ratio in the test section was 1.3% at zero angle of attack. Surface pressure measurements and oil-flow studies were made at the design angle of attack of 5° over a Mach number range of 0.25 to 0.96 and a Reynolds number range of 3.4×10^6 to 10×10^6. No Reynolds number effect on the results was reported to exist. The lift interference from the tunnel walls was reported to be small. This is because the leading-edge pressures of the experiment and computations in the correlations happened to agree with each other at the design angle of attack of 5°. Transition strips were installed at 4.5% chord.

4.4.2 Attached Flow Cases

The first set of WING C flow computations using the TNS program to be discussed will be attached flow cases. These cases are included to demonstrate the two-dimensional nature of the flow in the attached flow regime. This two-dimensional flow aspect was part of the design goal undertaken by the WING C design project. Attached flow calculations were done for two supercritical cases. In all these and subsequent computations, the Reynolds number is based on the mean aerodynamic chord of the WING C, and turbulent flow calculations are started at the very leading edge without any transition model.

The first case consists of a slightly supercritical flow at $M_\infty = 0.70$, $\alpha = 5°$, and a Reynolds number based on mean-aerodynamic-chord of 6.8 million. Figure 28 shows the pressure coefficient distribution of WING C at 5 spanwise stations. The agreement between the two experiments and computation is quite good even at the $\eta = 0.90$ (tip) location. However, the TNS results agree with the small-scale model data [104] slightly better than with the large-scale model data [107]. The discrepancy between the two sets of data is probably caused by differences in wall interference effects, and differences associated with the measurement of angle

of attack and free-stream Mach number. An increase in the effective boundary-layer thickness decambers the aft section of a supercritical airfoil, which can significantly affect the predictions of lift and pitching moment. Figure 28 and the following figures showing pressure coefficient distributions reveal that the effect of the thickening boundary layer near the trailing-edge is more significant in the large-scale model data than it is in the small-scale model data. Therefore, the trailing-edge pressures of the large-scale model data are consistently lower than those of the small-scale model data. Although the general agreement is good, the TNS trailing-edge pressure values are overpredicted compared to the experiments. Figure 29 shows the experimental oil flow picture from Ref. [107] and the computed upper-surface skin-friction lines side by side. As seen from the figure, the flow is almost entirely two-dimensional on the wing, and the computation accurately reproduces this situation.

The second computation is again an attached flow case with higher Mach number. The flow conditions are $M_\infty = 0.82$, $\alpha = 5^\circ$, and $Re_{m.a.c.} = 6.8 \times 10^6$. The computed pressure coefficient distributions are compared with data from the small-scale and large-scale model tests in Fig. 30. The comparison is very good in general, with the TNS solution in slightly better agreement with the small-scale model data [104]. The same considerations about the discrepancies between the experiments and computation presented for the $M_\infty = 0.70$ case apply here. It is also useful to understand the shock wave development on the wing for interpreting shock-induced separations. Mach number contours, which show the shock wave pattern on the upper wing surface, are presented in Fig. 31. A shock wave forms parallel to the leading-edge, and a small second shock wave forms nearly perpendicular to the root at the tip. Figure 32 shows an experimental oil-flow photograph and the computed skin-friction lines. In the oil-flow picture, only a weak shock wave is evident, indicated by a slight S-shape in the oil streak lines which lie in the outboard section of the wing between about 15% and 25% chord. This shock wave is not strong enough to separate the boundary layer, contrary to the earlier computations by Mansour [34]. The flow is almost two-dimensional in the sense that the spanwise flow is negligible, and flow deflection angles are less than 10° except near the leading-edge.

4.4.3 Separated Flow Cases

The first separated flow case consists of the WING C design conditions: $M_\infty = 0.85$, $\alpha = 5^\circ$, and $Re = 6.8 \times 10^6$. These conditions were intended to result in attached flow with a mild shock wave and a mild pressure recovery. But, for reasons discussed in Ref. [107], these conditions produced a "local" (as called by its author) flow separation. In this dissertation, the adjectives such as "local" versus "global" or "open" versus "closed" will be avoided because of the current debate. However, the interested reader may refer to Ref. [86] for particulars.

The computed pressure coefficient distributions compared with experimental data are presented in Fig. 33. Two shock wave systems are distinguished: a leading edge shock and a secondary shock. The computed leading-edge shock agrees well with the experiments, though there are some discrepancies in the second shock. The computed second shock seems to agree best with the average of the experimental results in this region. Again the viscous effects decamber the aft portion of the wing and the trailing-edge pressures of the large-scale model data (Keener [107]) are lower than the small-scale model data (Hinson and Burdges [104]). Note that the TNS trailing-edge pressures agree well with the small-scale model data. Figure 34 shows the wing-planform Mach number contours plotted at a location above the upper-wing surface which displays the well-known transonic lambda shock-wave pattern.

The experimental oil-flow picture of the same case is presented in Fig. 35. Figure 36 shows the postulated skin-friction field. A separation line caused by the swept shock wave emanates from a saddle point with two counter-rotating vortices on either side. The conjectured skin-friction map also features two saddle points and one nodal point of attachment. In three-dimensional separation, it is not possible to define a closed separation zone or "bubble," as in two-dimensions. Here, the separation zone is largely fed by the vortical flow on the inboard side of the saddle point of separation. The tip flow is highly curved inboard towards the separation zone but does not enter the zone. Also, some streamlines are entrapped by the inboard vortex while others pass by the separation region without being trapped. The flow is almost two-dimensional outside the separation zone.

The computed skin-friction lines for this case are presented in Fig. 37. Note that an angle of attack correction of $+0.9^\circ$, i.e. $\alpha = 5.9^\circ$, was used in the computations to get a closer computational/experimental agreement. In this computation, the global features of the experiment are predicted well: the location and size of the separation line, the streamlines being trapped by the vortex-like formation inboard of the separation line, the curvature of the tip streamlines and almost two-dimensional flow outside the separation zone. The critical points of the skin-friction map weren't predicted, except a nodal point near the corner-like region between the line of separation and the tip flow streamlines. Overall, the simulation is globally very good and is quite encouraging. Moreover, although the critical points were not predicted, the computed topology is capable of producing a map similar to the experimental one: first of all, by increasing the grid resolution and using the techniques described in Sec. 4.3, the vortical flow inboard of the line of separation can possibly evolve into a vortex and, since there is already a nodal point on the other side, emergence of a saddle point between them is inevitable. Such an evolvement was shown to be possible in Sec. 4.3 by applying new artificial dissipation techniques and turbulence models. These techniques weren't applied in this case, but if applied, a significant chance for improvement

would be possible. Also, it should be kept in mind that the grid near the tip is coarse and increasing the resolution would probably improve the correlation. Another important issue to address is that the thin-layer approximation may be deficient in this region where there are strong streamwise and crosswise viscous flow gradients which are not accounted for in the thin-layer approximation. In addition, experimental uncertainties associated with wind-tunnel wall interference, angle of attack measurement, free-stream Mach number measurement, etc., must be considered in evaluating the computational/experimental correlations.

In light of these encouragements, it is interesting to go one step further and study the flow field above the surface. Investigation of a three-dimensional flow is by nature very complex and needs sophisticated graphics utilities. In this work, a post-processing program called PLOT3D developed by Buning [108] at NASA-Ames was used. PLOT3D is a graphics program capable of plotting all relevant quantities of the flow field in three-dimensions. Particularly, the particle-tracing utility of the PLOT3D was helpful because of its power to display the actual fluid motion.

The particle paths, in general, can be divided into two groups: "streamlines" and "sectional streamlines." These two terms are explained in Fig. 38. If a particle is released from point A, its path may be plotted in several ways, including the three shown, AB, AC, and AD. If its motion is not confined to any surface, it moves according to the fluid dynamic forces and becomes a "streamline." Note that in steady flow, pathlines are equivalent to streamlines. If the motion of the particle is confined to $x-y$ or $y-z$ planes, "sectional streamlines" are obtained: the lines AD and AC respectively. It is not hard to imagine a sectional streamline. For example, the line AD may be likened to the motion of a free-surface fluid particle when a body is immersed into a liquid and set into a motion. In this case, the motion of the particle is confined to the free-surface of the liquid. The sectional streamlines are computed from only the components of velocity on that particular surface, i.e., the projections of the velocity vectors on the surface. Note that the sectional streamlines are not the same as the projection of streamlines on the surfaces. For example, if the streamline AB was projected on the $x-y$ or $y-z$ surfaces, lines other than AC or AD would be obtained.

Now, let us explore how to obtain various lines and surfaces which are of importance in the topography of flow fields. First of all, in steady flow, the trajectory of a "free" particle is a streamline. It shows exactly where the fluid is going. The skin-friction lines, which resemble the oil-flow, are simply the sectional streamlines traced on a surface very near a body. The reader is reminded that as $z \to 0$ the $\mathbf{u}/z$ field becomes identical to the surface stress field of a body (see Sec. 4.2.2). Therefore, in Computational Fluid Dynamics, the skin-friction lines are obtained by plotting the particle paths constrained to the first grid

surface off a body. However, the distance z from the body must be essentially constant to make the $\mathbf{u}/z$ field identical to the $\mathbf{u}$ field.

The physical meaning of the sectional streamlines is limited. The sectional streamlines coincide with the true streamlines only on the solid surfaces and symmetry surfaces if the flow is also symmetric. However, keeping in mind the limitations, the sectional streamlines are still instrumental for understanding the flow fields. At this point, some figures which will be discussed later in this paper can be used here as examples. As for example in Fig. 68, the sectional streamlines are used to illustrate the vertical extent of the separated region, and the vortical flow inside that region. From the very same figure, it could be imagined that a line which emerges from the line of separation extends above the wing, and divides the vortical flow in the separated region from the free stream which flies over that region.

If we define a surface which emanates from a line of separation, and which divides the mass of separated fluid from the surrounding fluid as a "streamsurface," the aforementioned line in Fig. 68 which is composed of closely packed streamlines, is the cross-section of that "streamsurface" versus the JL plane. Therefore, we understand that it is possible to define the boundaries of a streamsurface by cutting it through with a sufficient number of planes each of which displays the sectional streamlines. This was done, for example, in Figs. 54 and 55. The separated zone could also be studied by using the sectional streamlines in a different orientation. In this case, as in Fig. 56, the sectional streamlines are plotted in the JK (body-parallel) planes. These figures serve to define approximately the boundary of the streamsurface as observed from above.

In other examples, Figs. 62 and 67, an even more dramatic application of the sectional streamlines has been made. If we concentrate, say, on Fig. 67, the boundaries of the vortical flow are evident. In this figure, particles are released from different normal levels and are confined to stay on their respective planes. Had the Figs. 67 b, c, d been placed on top of each other, the boundaries of the vortical flow would have coincided. On the other hand, the true streamlines which were traced for the same case in Fig. 65 don't give us such clear information, but give a very complex picture. Hence, the sectional streamlines are extremely useful for such cases.

There are certain things to keep in mind when dealing with the sectional streamlines, however. Since they are the integrated curves of the projections of the velocity vectors on a certain surface, the orientation angle of the cutting plane is very important. Unless the cutting plane angle is nearly perpendicular to the lines of separation or reattachment, a distorted view is obtained. This is illustrated in Fig. 39. The figure depicts skin-friction lines for an ideal case: a

separation "bubble" which might occur on an infinitely swept wing. The skin-friction field at the root of such a "bubble" is cut by three planes I-I, II-II, and III-III, making an angle of 90°, −45°, and 45°, respectively, with the lines of separation and reattachment. The separation and reattachment points are designated by S, S,′ S,″ and R,R,′ R″, respectively, on the three cutting planes. Observe that only plane I-I accurately represents the separation and reattachment lines (S-R). For the other planes, the plotting program cannot accurately predict these lines, showing the distance between the singular points to be shorter on plane II-II (as S′-R′), and longer on plane III-III (as S″-R″). The situation for the actual three-dimensional flows is even more difficult and, without use of other sectional streamlines, it is not possible to gather accurate information.

These particle tracing techniques are very helpful in understanding three-dimensional flow fields, and they will now be employed to survey the separated WING C flow. Figure 40 shows the WING C surface grid together with the index designations for the planes of interest which will be used in subsequent figures. Figure 41 is the same as Fig. 37, except it is a three-dimensional perspective view. In this figure, only one particle at each spanwise η station was released from the J=15 grid line parallel to the leading-edge. The particles were confined to the first grid surface off the body, and therefore become sectional streamlines which define skin-friction lines. This figure defines the separation line and the particles which are entrapped by the separation zone, and also shows that the tip streamlines do not enter the zone. To help understand the following particle-path plots, the difference between the streamlines and sectional streamlines on the wing are demonstrated in Fig. 42. Instead of releasing just one particle from each spanwise station (as in Fig. 41), two particles were released in different modes. One set of particles was confined to the first grid surface off the body, and the second set was released without constraint from the same physical position. Hence, the first set becomes sectional streamlines or, to be more specific, skin-friction lines, and the second set becomes streamlines. As observed, two particles released at the same point trace the same path for a short distance and then diverge. If the two particles are released upstream of the separation zone, they trace similar paths until they encounter the separation. In the vicinity of separation, the constrained particle is entrapped but the free particle is not. It is easy to understand why the unconstrained particle flies over if the separation zone is thought of as a solid barrier. This situation may be likened to the phenomenon in Fig. 38. Here, line AD resembles a constrained particle path and line AB resembles an unconstrained particle path. Observe that the separation zone in Fig. 42 is thin, as deduced from the curvature of streamlines above the region.

A series of pictures in Fig. 43 displays the separation surface emanating from the separation line as well as other interesting features of the three-dimensional boundary layer. In each picture, particles are released along an L-grid line which

is perpendicular to the wing from near the body to above the boundary layer. The particles are released from spanwise stations K = 14, 15, 18, and 21, which span the separation zone. It should be emphasized that these particles are constrained to stay on their respective ξ-η parallel surfaces to define the separation surface. If any particle hits the separation surface, it must go around it because the separation zone behaves like a solid object. Figure 43a shows the particles released from the K = 14 station, which is the last station, for which particles are not entrapped by the vortical-like flow of the separation zone. The inviscid streamlines are almost parallel to the free-stream direction. As the viscous boundary layer is gradually penetrated, the streamline curvatures rapidly increase toward the separation zone. Figure 43b shows how the particles released from K = 15 go around the separation zone. The first particle path off the body is the skin-friction line which represents the line of separation. Notice that the second particle path follows parallel to the line of separation and becomes a tip flow. Figure 43c shows the particles released from the K = 18 plane. This figure clearly shows how the separation surface evolves from the line of separation. When the particles released from different levels approach the separation zone, they can not penetrate it; rather they flow over the separation surface, which is also a surface made of streamlines. Finally, Fig. 43d shows that the particles released from the K = 21 plane avoid the separation zone and pass by it without entrainment. This was already discovered in the study of the oil-flow pictures (see Figs. 35 and 36). To give an idea about the thickness of the separation zone, sectional streamlines constrained to lie within ξ-ς planes are presented in Fig. 44. The separation zone is extremely thin, being less than 0.001 chords. To complete the flow field survey, sectional streamlines in planes parallel to the wing surface (ξ-η) are presented in Fig. 45. The separation and reattachment lines are observed in the L = 2 plane, which is the first grid surface off the body. The Figs. 45 b, c and d, define the boundary of the streamsurface which emanates from the line of separation in Fig. 45 a. The separation line-type lines in Figs. 45 b, c, and d are the cross-sections of the streamsurface with the JK planes.

The second separated case associated with WING C consists of a flow at off-design conditions: $M_\infty = 0.90$, $\alpha = 5°$, and $Re = 6.8 \times 10^6$. The computed and experimental pressure coefficient distributions are compared in Fig. 46. The leading-edge and aft shock-waves are stronger than those of the previous case, and the aft shock-wave is further downstream. This is a consequence of the increased free-stream Mach number. Despite a slight overprediction of the trailing-edge pressures, the agreement between the experiment and computation in this difficult case is very good except in the tip region, probably because of the coarse grid effect. The strength and location of the lambda shock-wave is accurately predicted. The planform view of WING C showing the lambda-shaped shock-wave is presented in Fig. 47. This agrees very well with the experimental

pattern reported in Ref. [104]. The Mach number contours of the ξ-ς plane which cuts the wing in the streamwise direction at the station $\eta = 0.77\%$ is shown in Fig. 48. The zonal boundaries are also shown in this plot. Note the smoothness with which the shock wave crosses the zonal interface boundary. This indicates that the communication between the blocks is implemented in a conservative manner. In addition, most of the other contours cross the zonal interface boundaries in a smooth and continuous fashion. Downstream in the wake where the fine viscous grid interfaces with a relatively coarse grid (see Fig. 5), the wake abruptly stops. This aspect of the solution exists because the coarse inviscid grid cannot retain the sharp wake gradient.

The surface oil-flow photograph and the present *postulation* of the skin-friction lines for this case are presented in Fig. 49. When the Mach number is increased from 0.85 to 0.90, the flow separation that existed over the outer 30% of the wing moves slightly downstream and grows significantly in size. The counter-rotating vortices which emerged in the previous case grow substantially, and the larger vortex inboard of the separation line extends as far as the trailing-edge. A line of separation emerges from the saddle point of separation. There is one focus on the tip side and a node of separation on the inboard side of this line. Another saddle point exists very near this node of separation. This saddle point lies between the node and the second, larger, focus. There exists another saddle point near the trailing-edge. The inboard vortex is strong and provides a mechanism to feed fluid to the separation zone by entrapping the streamlines coming from the inboard side of the separation zone. The flow between the separation zone and the symmetry plane is again almost two-dimensional in the sense that the spanwise flow is negligible.

The computed skin-friction lines for the same case ($M_\infty = 0.90$) are presented in Fig. 50. As observed, the agreement between these computed lines and the experimental picture in Fig. 49 is rather poor. A weak swirling motion is exhibited in the computation on the inboard side of the separation zone, yet the smaller vortex near the tip is nonexistent. Because of the coarseness of the present grid near the tip, this vortex is probably not resolvable. The disagreement occurs close to the tip where the computation does not capture the shock location well. It is this poor shock location (see Fig. 46) which moves the separation line too close to the trailing edge and causes the disagreement between the experiment and computation. In an attempt to better align the computed line of separation with that of the experiment, this case was recalculated at a slightly lower Mach number. It was found that when the Mach number was reduced slightly, to 0.88, significant changes were observed which were in close agreement with the $M_\infty = 0.90$ experiment.

The computed skin-friction lines for this slightly lower Mach number are

shown in Fig. 51. This flow pattern is indeed more descriptive of the experimental oil-flow at $M_\infty = 0.90$: the line of separation moves forward, in better agreement with experiment, and there is substantially stronger vortical flow in the area of the inboard vortex. The node of separation in the experiment was captured. The saddle point which lies near the trailing-edge of the wing in the experiment was also captured. However, the vortex close to the tip has not been resolved. Had this vortex been resolved, emergence of the experimental saddle point between this vortex and the node would have been automatic according to the continuity equation. The computation also predicts a reattachment line at the trailing-edge near the tip, though this doesn't exist in the experiment. To recapitulate, although quantitative details are not accurately reproduced many qualitative details are. The location and extent of separation are in reasonable agreement with experiment, as is the pressure distribution. The onset of vortex formation which is evident in the experiment is also present in the computation. In addition, experimental uncertainties associated with wind-tunnel wall interference, angle of attack measurement, free-stream Mach number measurement, etc., must be considered in evaluating the computational/experimental correlations.

Although the surface flow was not accurately reproduced, it is instructive to explore the three-dimensional flow exhibited by the computation above the wing. Again, the sectional-streamlines will be used to study the flow field. The computed skin-friction lines which were presented in Fig. 51 are shown again in perspective view in Fig. 52 to give a more in-depth look at the flow field. The rapid convergence and divergence of the skin-friction lines clearly mark the separation and reattachment lines, respectively. To give an idea about the thickness of the separation, sectional streamlines are presented on a streamwise cut ξ-ς plane at spanwise station K = 17 (Fig. 53). The thickness of the separation zone is about 0.005 chords; which is much larger than the previous case. Figure 54 is an expanded view of the previous picture in the vicinity of the line of separation. Note that a shear surface lifts off the body from the line of separation at point S on the ξ-ς computational plane. This shear surface partitions the outer flow from the separated flow, and is made of many streamsurfaces emerging near the separation line which enfold each other. In Fig. 55, a series of sectional streamlines in (ξ-ς) planes which span the separation zone are presented. As seen in the figure, the boundary layer displacement thickness grows from station K = 12 to K = 20. In this figure, the vertical scale was expanded 5 times with respect to the horizontal scale to better observe the details. At the K = 19 and 20, a vortex core is observed under the shear surface. It should be kept in mind that, in all these plots, there is a substantial amount of transverse flow perpendicular to the $\xi - \varsigma$ planes. Also note that the points of separation and reattachment cannot be determined accurately from these views for the reasons enumerated in reference to Fig. 39. Accurate detection is only made possible by the skin-friction lines.

Sectional streamlines through the separation zone in the surface-parallel computational planes (ξ - η surfaces) are presented in Fig. 56. This figure gives a sequence of views from the body surface to the edge of the separation zone. The shear surface emanating from the line of separation acts as a barrier between the flow within the zone and the flow upstream of it. In this figure, the approximate location of the shear surface is seen as a line of cross section between each body-parallel computational plane and the zone.

The last computed case associated with WING C involved another off-design condition: $M_\infty = 0.95$, with $\alpha = 5°$, and $Re = 6.8 \times 10^6$. The comparison of the computed skin-friction lines with the experimental oil-flow photograph was similar to the $M_\infty = 0.90$ case discussed before and is not presented here. However, the pressure coefficient comparison is shown in Fig. 57. Despite the high free-stream Mach number and the large amount of separation, reasonable agreement is obtained except at 90% semi-span.

4.5 Simulation of NACA 0012 Wing Flow Cases

Simulation of the NACA 0012 wing with wind tunnel walls modeled was presented in Sec. 4.4. Experiments made by Lockman and Seegmiller [61] furnished the information necessary to assess the capabilities of the various features of the TNS code. Among these are the wind-tunnel wall modeling characteristics, and the effects of artificial viscosity and turbulence models. In order to ascertain the degree of robustness of the present algorithm and, in particular, the ability of the present zonal interface scheme to cope with large flow gradients, some NACA 0012 wing free-air cases in more extreme conditions were run.

Three of these cases are presented here: flows with free-stream Mach numbers of 0.80, 0.85 and 0.90 at an angle of attack of 5 degrees with a Reynolds number based on chord of 80 million. Free-air conditions were necessary because the calculations with wind-tunnel walls modeled for the highest two Mach numbers were choked (see Holst et al. [45]). As a result, no experiment is available to compare with these cases. However, very interesting separated surface flow patterns and three-dimensional flows above the wing were obtained. They are introduced here with the belief that these solutions will be helpful in understanding separated wing flows.

The first case consists of a flow with mild streamwise separation. Flow conditions were $M_\infty = 0.80$, $\alpha = 5°$, and $Re = 8 \times 10^6$. Computed skin-friction lines are presented in Fig. 58. Except for significant inboard flow at the tip which is induced by the 5°angle of attack, the surface flow topology for this case is very similar to the wind-tunnel case presented in Fig. 23. Figure 58 describes a line of separation, a narrow streamwise separation zone, and a line of reattachment.

There is a node of separation and a saddle point on the lines of separation and reattachment, respectively.

The second computation corresponds to a massively separated case. Flow conditions were $M_\infty = 0.85$, $\alpha = 5°$, and $Re = 8 \times 10^6$. Figure 59 shows the wing upper-surface Mach number contours. As observed, there is an S-shaped swept shock wave which extends from the symmetry plane to very near the tip. This shock wave causes the boundary layer to separate between 20% to 90% of semi-span as shown in Fig. 60. A line of separation emanates from a saddle point with a focus on the inboard side and a nodal point of separation on the outboard side. This case exhibits a large reverse surface flow between the line of separation and the line of reattachment, which is located very close and parallel to the wing trailing-edge. Another saddle point can be recognized at the wing trailing-edge/tip. It seems that there is another line of secondary separation in addition to the primary streamwise separation. Surface flow coming from the tip region and from the line of reattachment coalesce on this line of secondary separation, and a streamsurface leaves the wing surface.

The large vortex defined by the focus constitutes the root of a large vortical flow between the lines of separation and reattachment. Also, the streamsurface emanating from the secondary line of separation probably coils into two small secondary vortices above the wing. Development of this large vortex and the secondary vortices above the wing are illustrated in Figs. 61 and 62. Figure 61 presents a series of three-dimensional pictures. They show sectional streamlines plotted on subsequent body-parallel computational planes in the JK plane.

Pictures from *a* to *h* are successive planes above the body surface to a height of nearly 10% of a chord. The pictures *a*, *b*, and *c* show lines similar to the separation line of Fig. 60. These lines are the cross sections of the computational planes with the separation surface which emerges from the line of separation. Note that there is a saddle point on each of these lines. The large vortex which coils up from the focus of Fig. 60 maintains its strength throughout the sequence of computational planes. The secondary separation line of Fig. 60, though not very clear, breaks into two secondary vortices as shown in Figs. 61*d*, 61*e*, and 61*f*. In these pictures, particles were released inside the separation zone to describe these vortices. Finally, pictures *g* and *h* of Fig. 61 show that these secondary vortices were probably dispersed and could not be traced any further, but the large vortex remains. Figure 62 complements Fig. 61 in describing the vortical flow pattern above the wing. In this figure, particles were released from the leading-edge at different L-levels and each was constrained in its respective JK plane. Figs. 62*a*, 62*b*, and 62*c* show that the particles very near the wing are captured by the core of the large vortex, whereas the particles away from the body flow past it undisturbed. Figure 62*d* shows the particles captured by the

big vortex and the secondary vortices as well.

The last case is again a massively separated case. Flow conditions were $M_\infty = 0.90$, $\alpha = 5°$, and $Re = 8 \times 10^6$. Again in this case, an S-shaped shock wave extending from the symmetry plane to very near the tip causes the boundary layer to separate. This shock wave is stronger than the previous one, and separates the boundary layer in the same S-shape. In this case, computed skin-friction lines exhibit a very interesting surface pattern shown in Fig. 63. The separation zone extends from the symmetry plane to very near the tip, and the chordwise extent of the separation zone varies from about one- to three-quarters of a chord. A line of separation emanates from a saddle point which is located at about two-thirds of the span. A focus occurs near the tip, and a node of separation is located inboard at about 30% of semispan. On the line of reattachment, another saddle point is recognized. Expanded views of these critical points are shown in Fig. 64. In this figure, the focus quite interestingly defines a motion which is not swirling inward, but swirling outward from the core. Although not shown here, a surface pressure plot reveals that this vortex is located at a low pressure region. The primary mechanism which feeds this vortex seems to be the downward flow coming from the large vortex as seen in Fig. 65. In this figure, particles are injected from about 40% of chord at L = 2 and are unrestricted. This figure exhibits two important phenomena: 1) there are two vortices, a large and a small one, and they are located at either side of the saddle point of separation, 2) it seems as if the streamlines coming from the large vortex feed the small vortex. Note that particles by the small vortex eject from it at the tip side. This is a very curious mechanism.

Unlike the particles in Fig. 65, the particles in Figs. 66*a* and 66*b* are restricted to their respective computational JK planes which are parallel to the surface. They are, therefore, sectional streamlines and define the core of the large vortex. The vortex core starts from the nodal point of separation shown in Fig. 63 and expands as it moves out from the surface. Sectional streamlines are also used in Fig. 67 to give the situation a more three-dimensional appearance. In these figures, the same technique utilized in making Fig. 43 is used. Sectional streamlines on JK (body-parallel) computational planes are obtained by releasing particles from different levels at particular spanwise stations. In Figs. 67*a* and 67*b*, particles are released from the tip side of the saddle point at K = 18 and 14. Figure 67*a* specifically shows that the particles closest to the surface are drawn into the small vortex. Particles more distant from the surface swirl around the small vortex but go to the core of the large vortex without entering the small vortex. Finally, particles away from the body run on straight paths without swirling. Figure 67*b* shows the same sort of behavior, but exhibits the particles captured by the large vortex more clearly. Figures 67*c* and 67*d* display the particle paths for particles released from K = 12 and 10, respectively, which are

inboard of the saddle point.

The most important feature of these figures is that they define an approximate envelope of the large vortex. The core of the vortex is observed at the bottom, and the near-circles at each level altogether define an approximate boundary of the three-dimensional vortex. This idea can be supported by placing Figs. 67*b*, 67*c*, and 67*d* on top of each other and observing that they fit together. Note that some particles are drawn toward the low pressure region of the small vortex. Finally, Fig. 68 shows the sectional streamlines in JL planes which are perpendicular to the wing surface. This cross-sectional plot was made at a semi-span station of $2y/b = 0.66$. Note that at this station, the separation region is large and easily extends from the Navier-Stokes region, across the zonal boundary, into the Euler region. The particles pass smoothly across the interface boundary with no function or slope discontinuities.

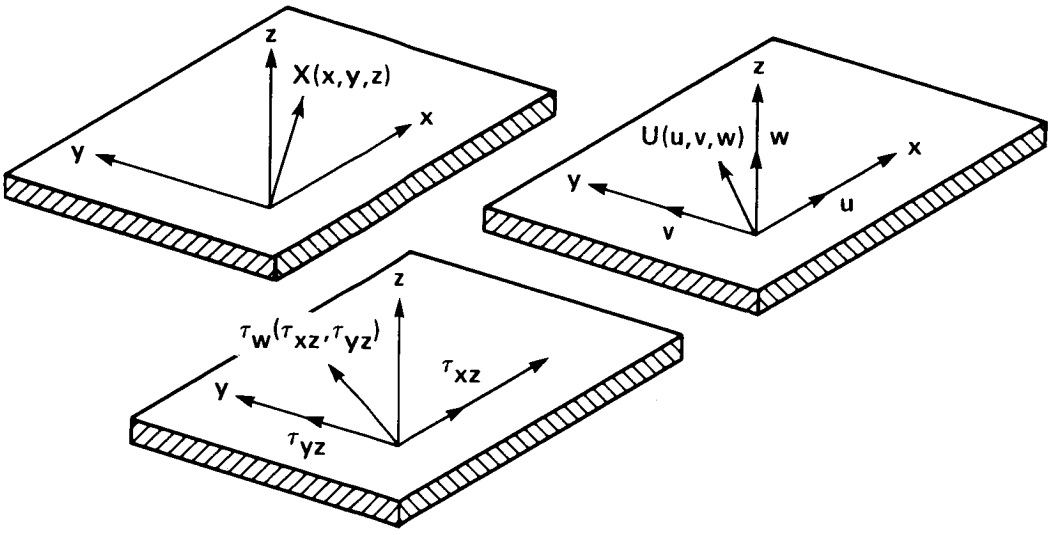

Fig. 14. The Cartesian coordinates, velocities and surface shear-stress vector components.

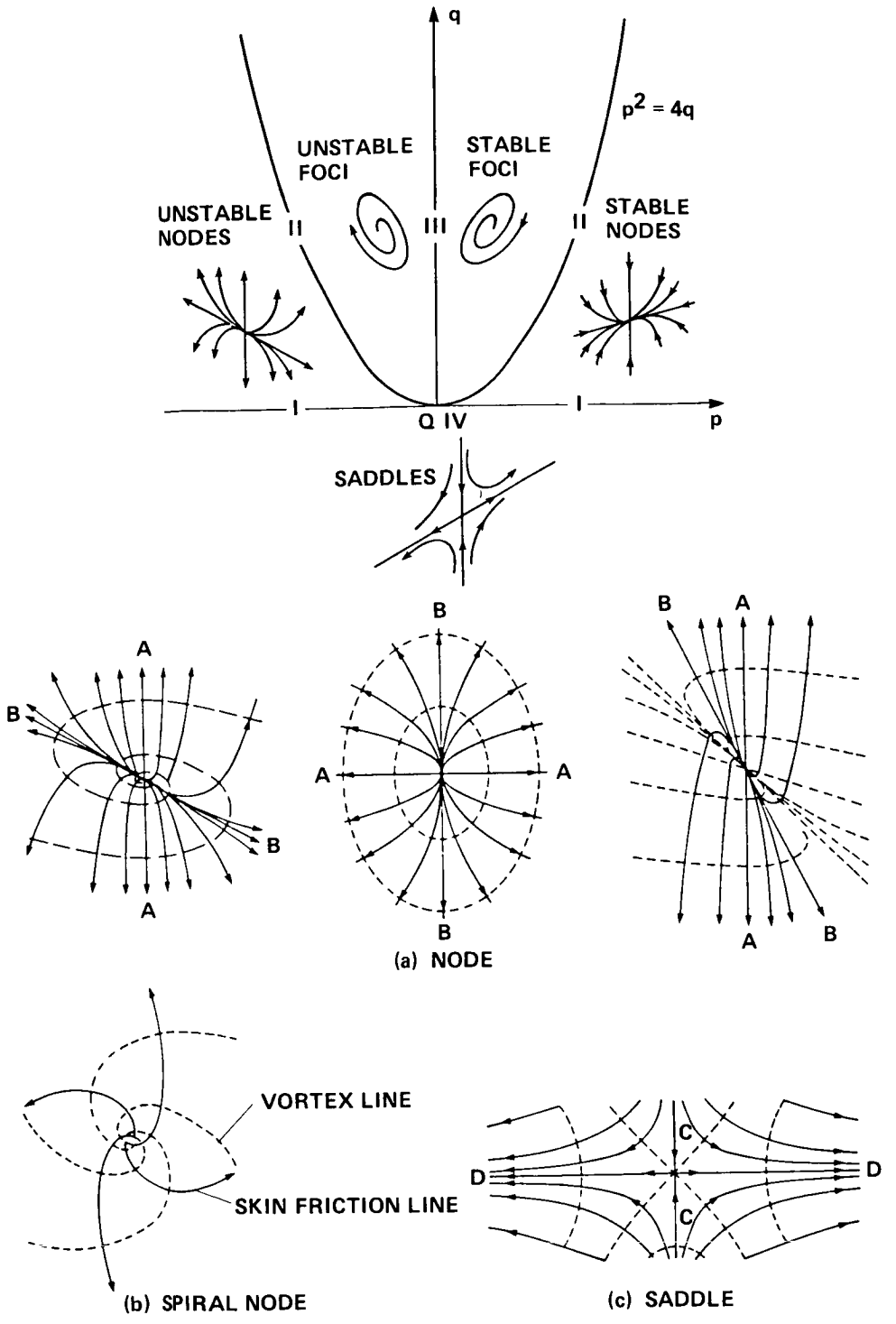

Fig. 15. Classification of critical points.

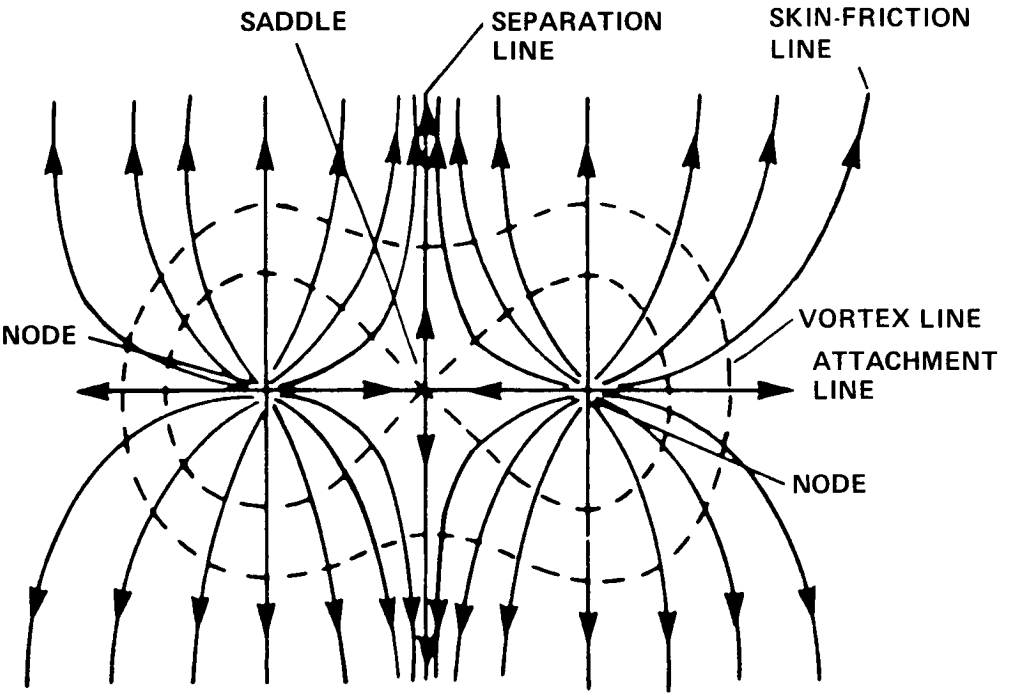

Fig. 16. A combination of two nodal points of attachment and a saddle point.

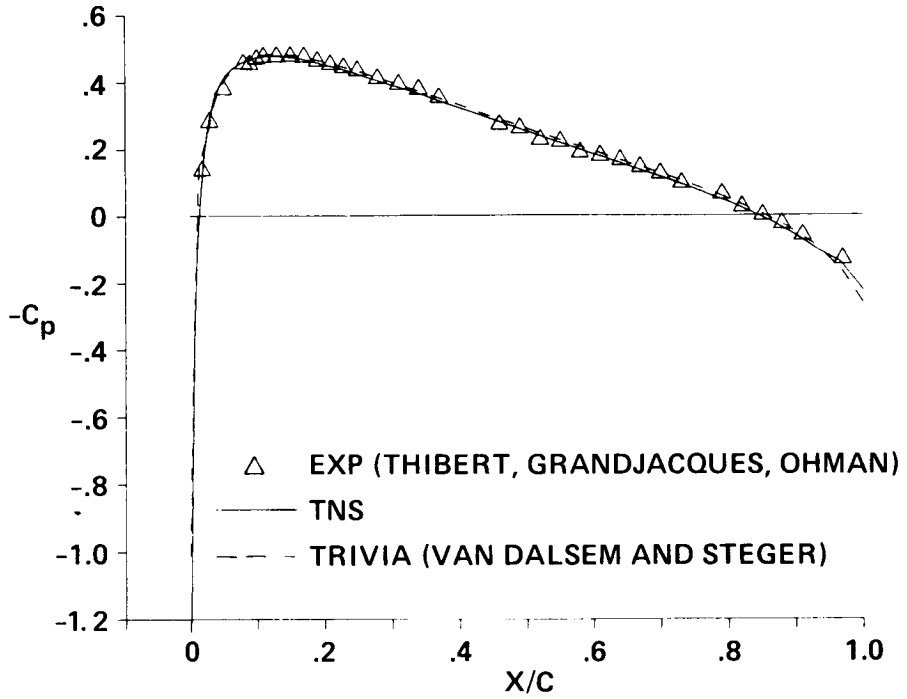

Fig. 17. Pressure coefficient comparison: NACA 0012 airfoil section, $\Lambda_{LE} = 0°$, $AR \gg 1$, $TR = 1.0$, $M_\infty = 0.5$, $\alpha = 0°$, $Re_c = 3 \times 10^6$.

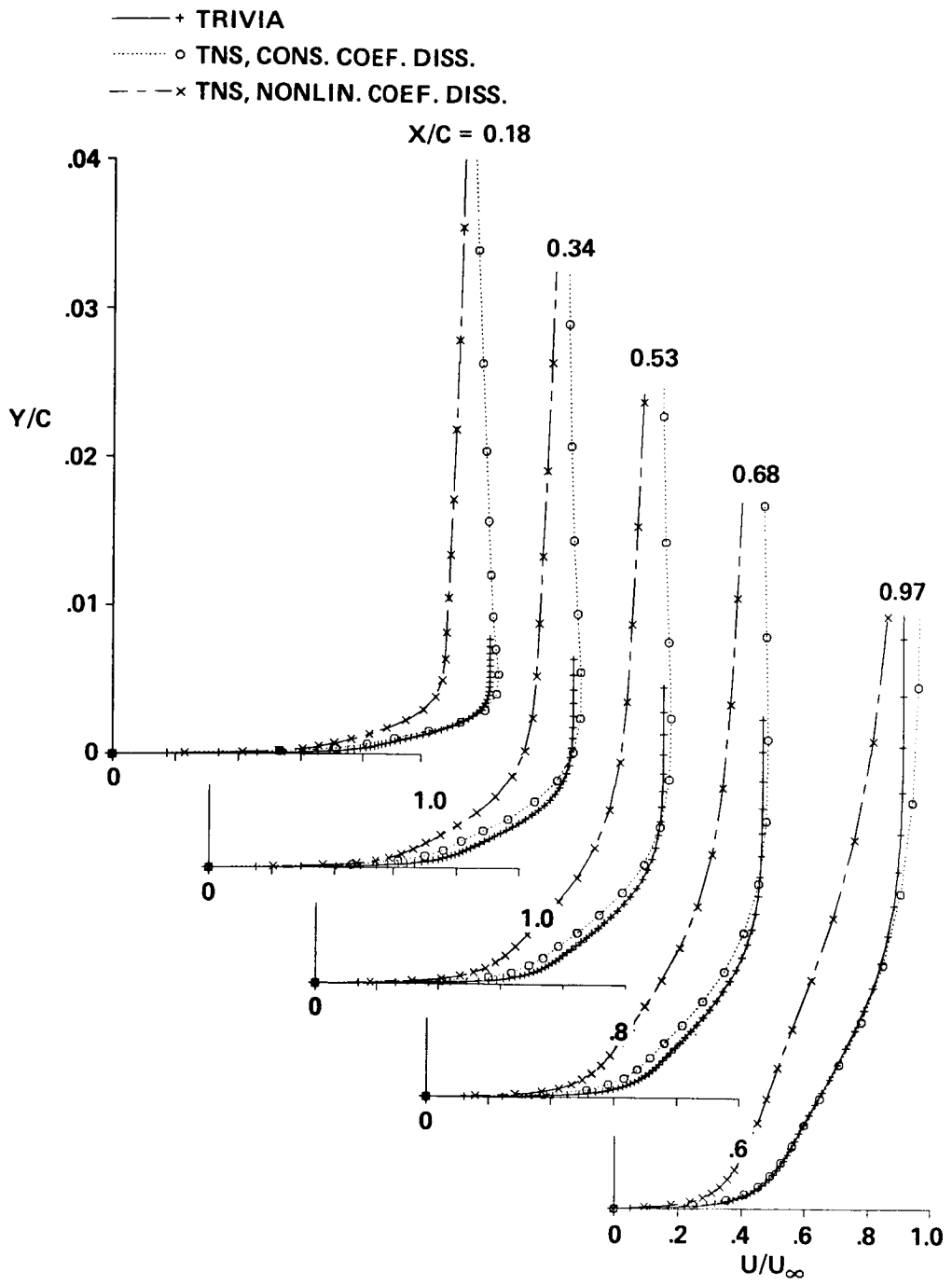

Fig. 18. Boundary layer velocity profiles computed from TNS using different smoothing terms: NACA 0012 airfoil section, $\Lambda_{LE} = 0°$, $AR \gg 1$, $TR = 1.0$, $M_\infty = 0.5$, $\alpha = 0°$, $Re_c = 3 \times 10^6$.

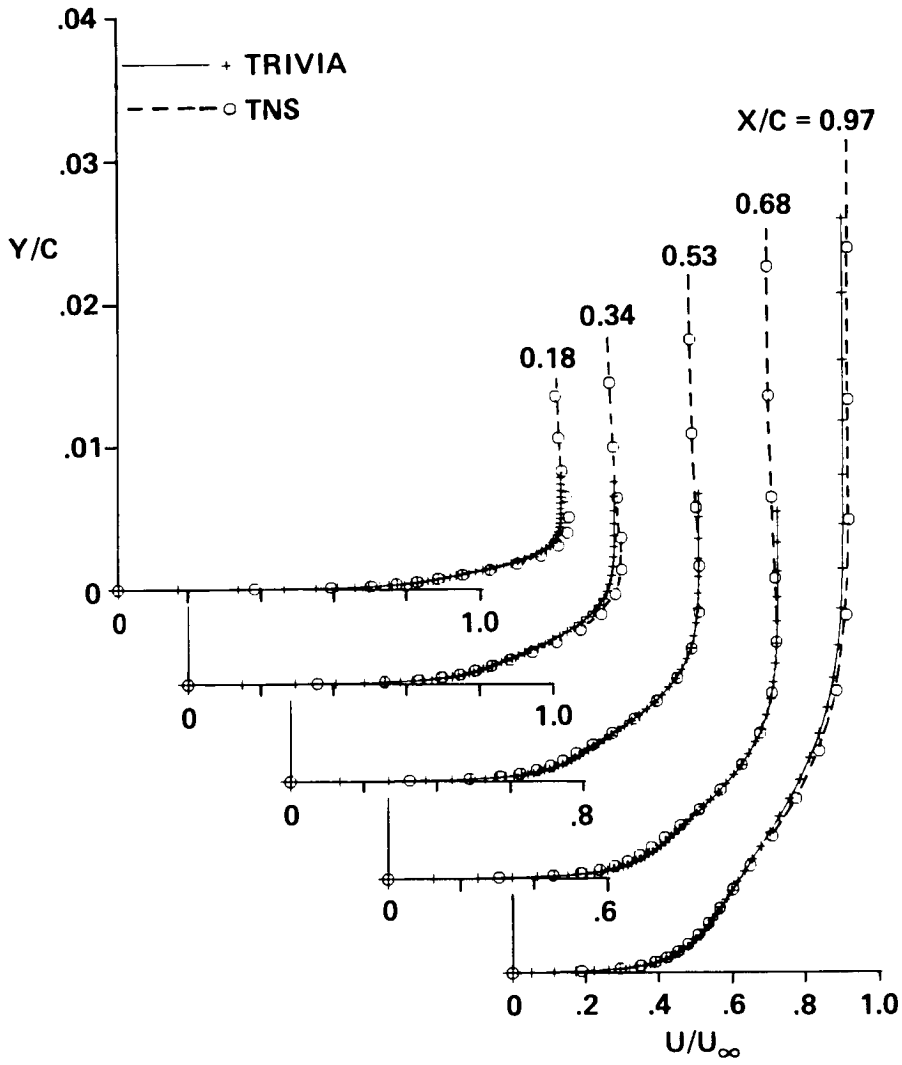

Fig. 19. Boundary layer velocity comparisons of TNS and TRIVIA: NACA 0012 airfoil section, $\Lambda_{LE} = 0°$, large aspect ratio, $TR = 1.0$, $M_\infty = 0.5$, $\alpha = 0°$, $Re_c = 3 \times 10^6$.

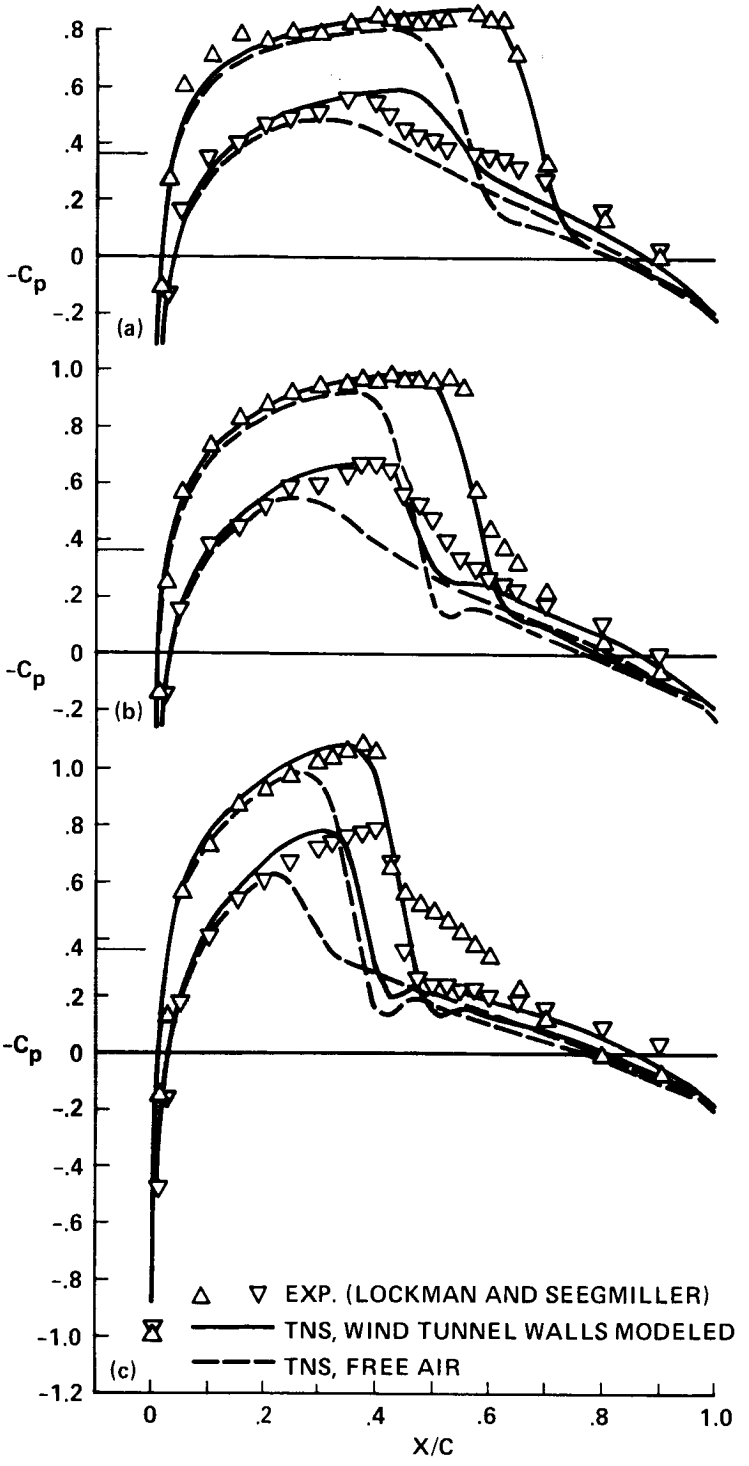

Fig. 20. Pressure coefficient comparisons: NACA 0012 airfoil section, $AR = 3$, $\Lambda_{LE} = 20°$, $TR = 1.0$, $M_\infty = 0.826$, $\alpha = 2°$, $Re_c = 8 \times 10^6$, *a*) $2y/b = 0.25$; *b*) $2y/b = 0.50$; *c*) $2y/b = 0.78$.

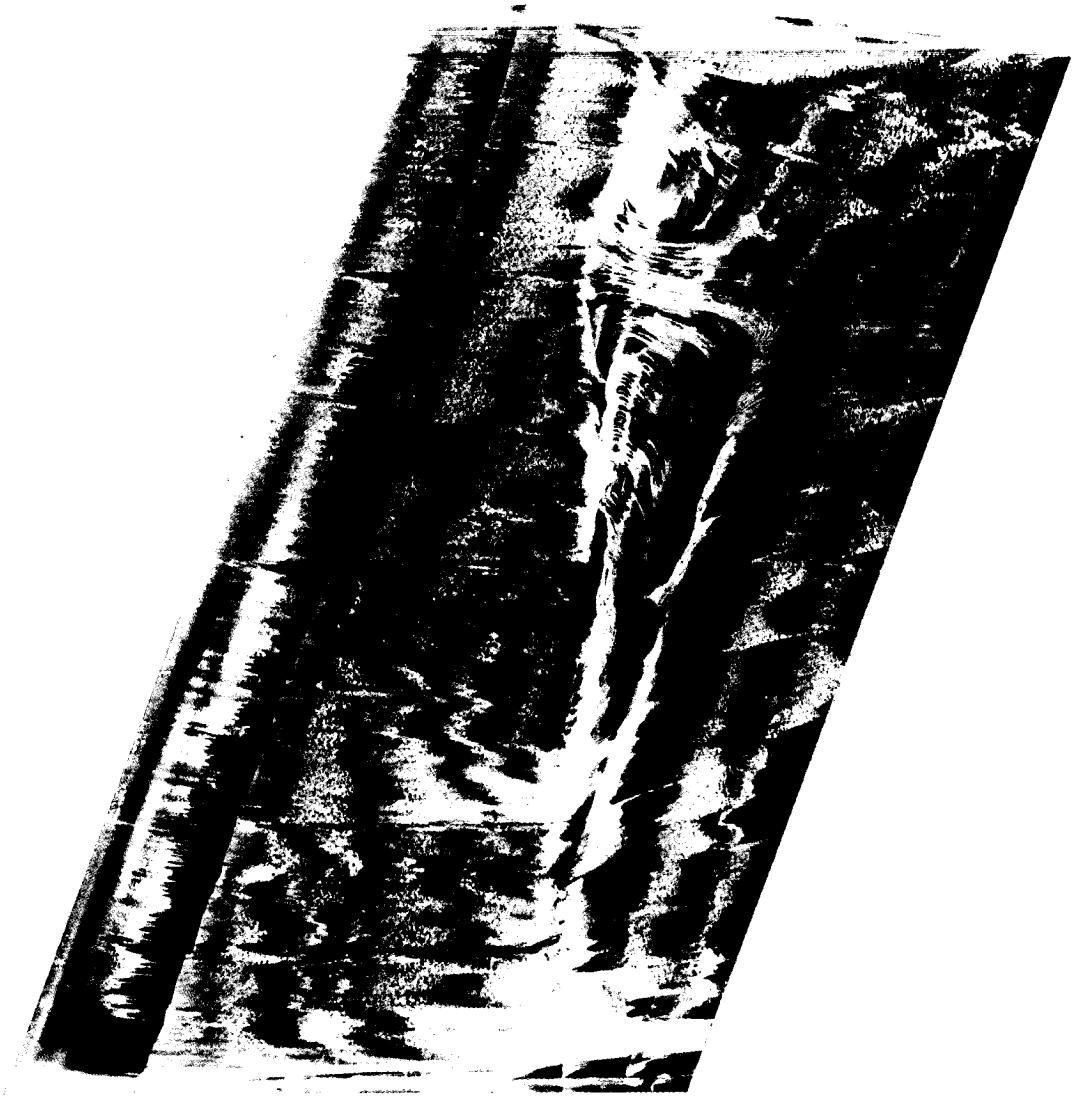

Fig. 21. Oil-flow pattern on upper wing surface: NACA 0012 airfoil section, $AR = 3$, $\Lambda_{LE} = 20°$, $\alpha_{TWIST} = 0°$, $TR = 1.0$, $M_\infty = 0.828$, $\alpha = 2°$, $Re_c = 8 \times 10^6$.

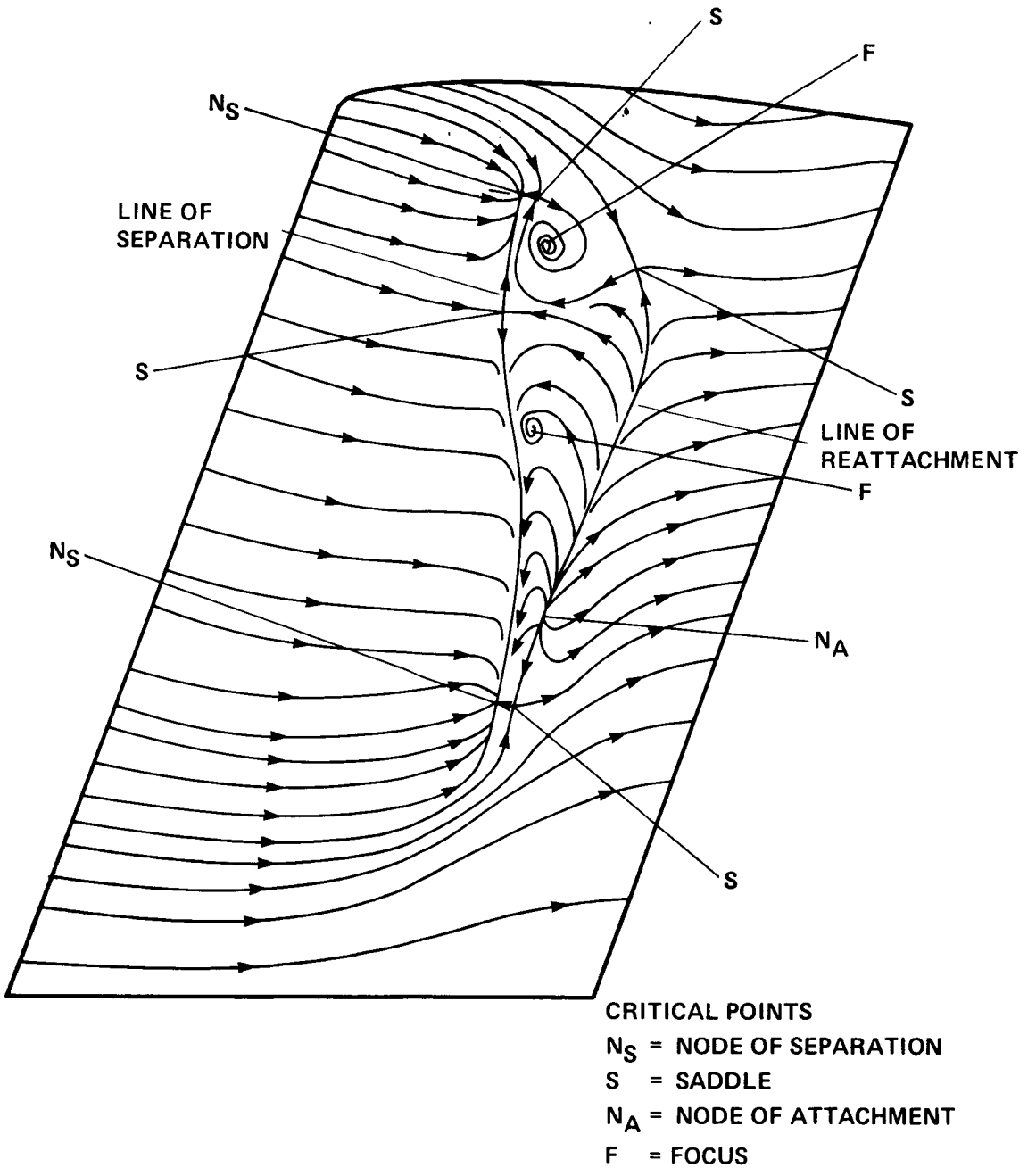

Fig. 22. "Postulated" skin friction lines for flow over the NACA 0012 wing of Fig. 21.

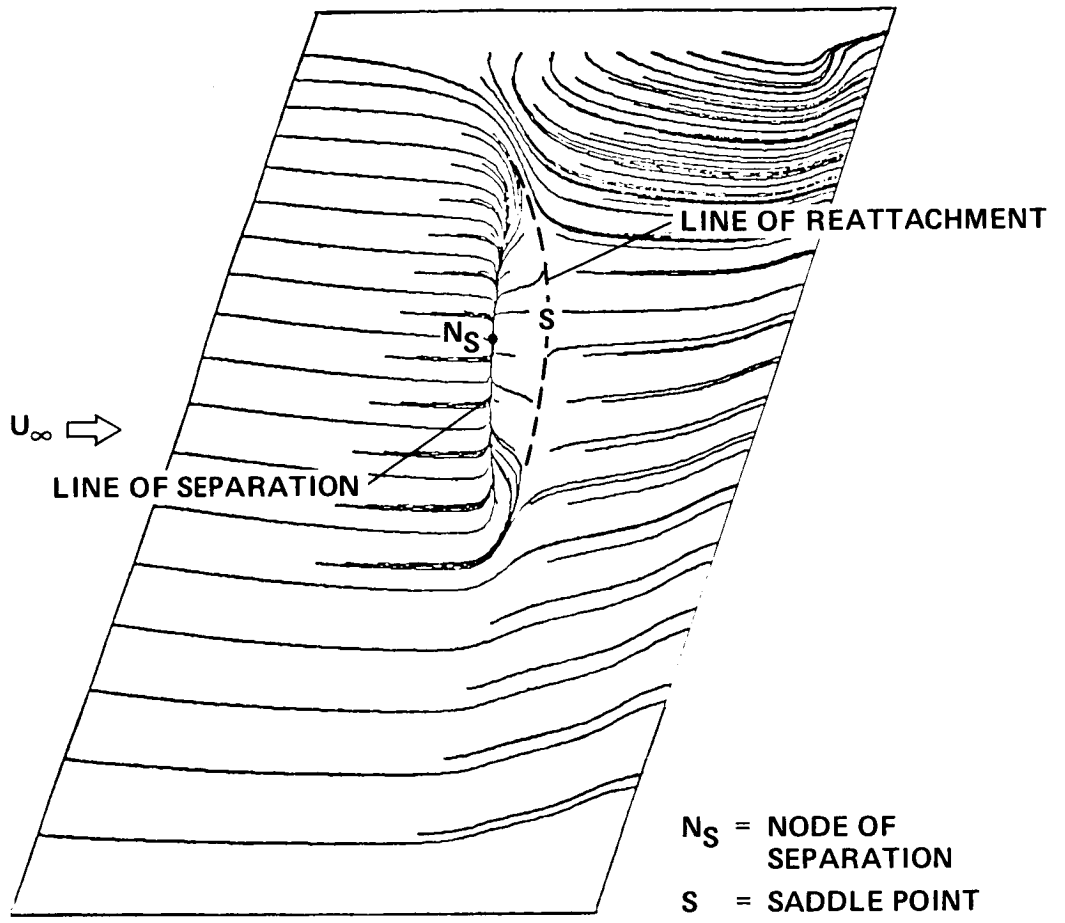

Fig. 23. Computed skin friction lines for the flow over the NACA 0012 wing of Fig. 21 with standard artificial dissipation model.

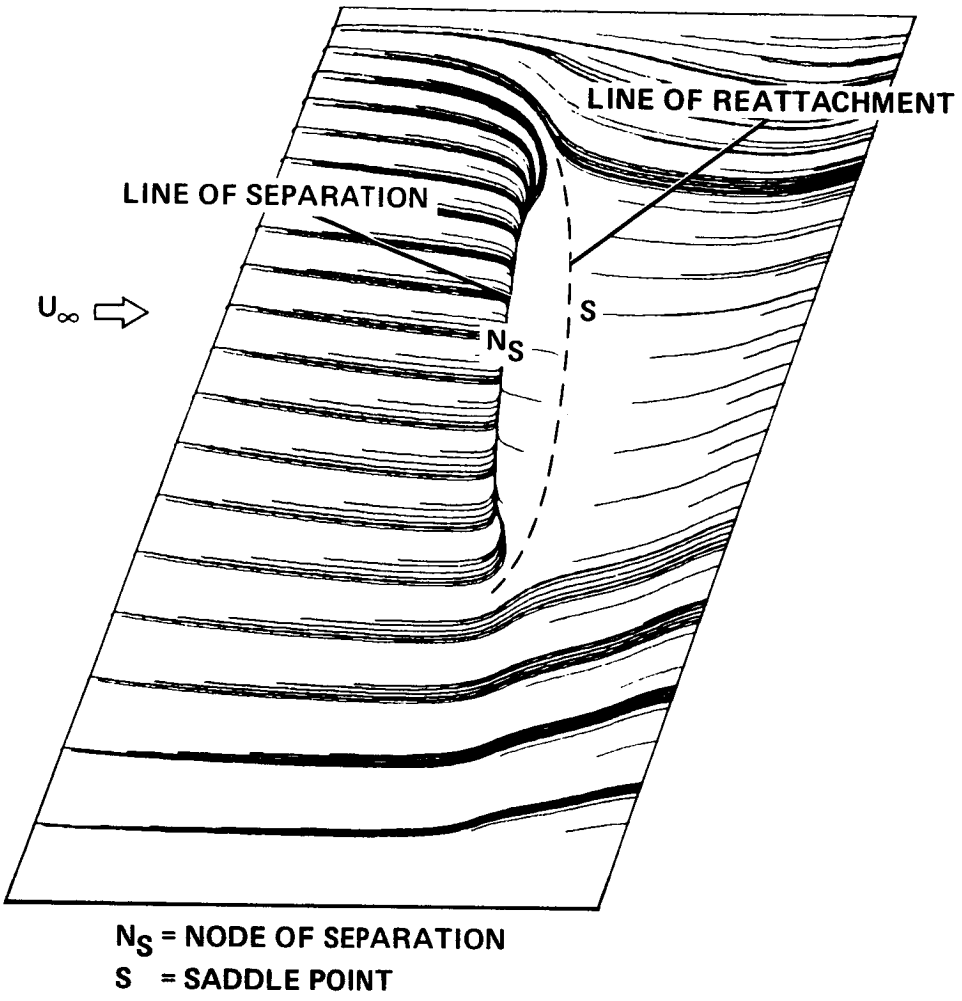

Fig. 24. Computed skin friction lines of the flow over the NACA 0012 wing of Fig. 21 with new artificial dissipation model.

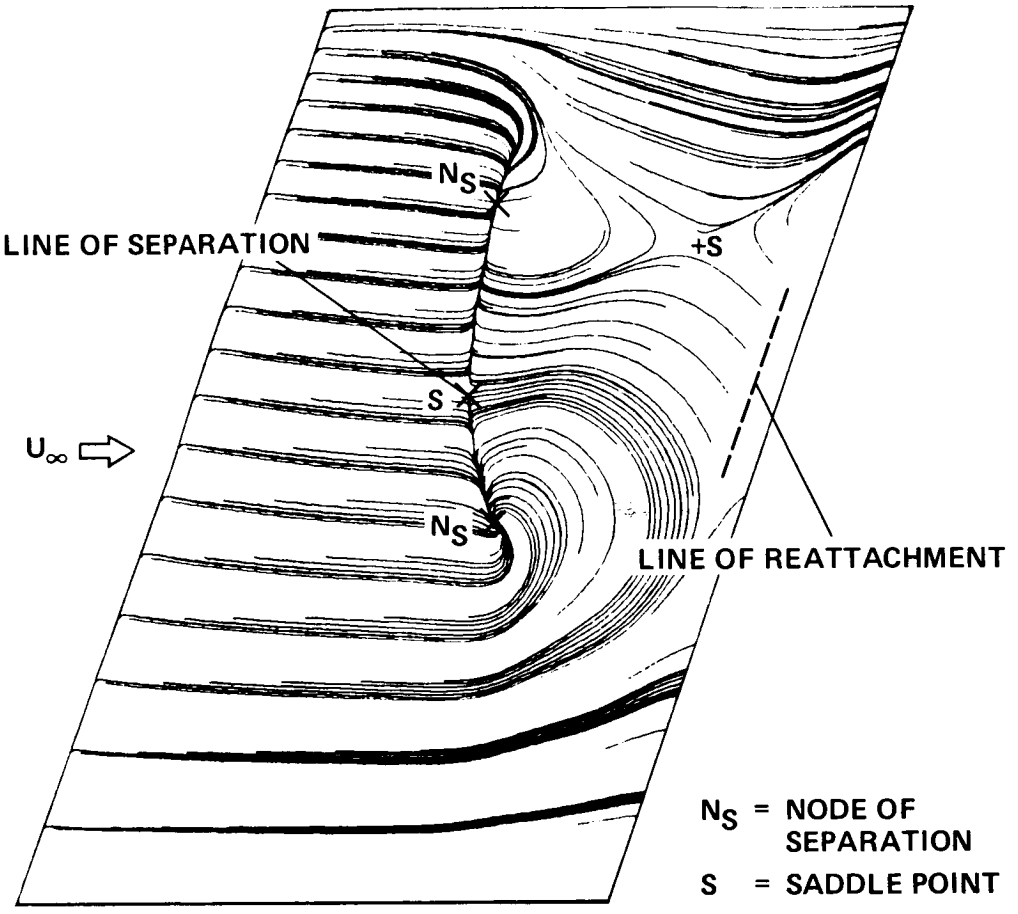

Fig. 25. Computed skin-friction lines for the flow over the NACA 0012 wing of Fig. 21 with new dissipation model and relaxation turbulence model.

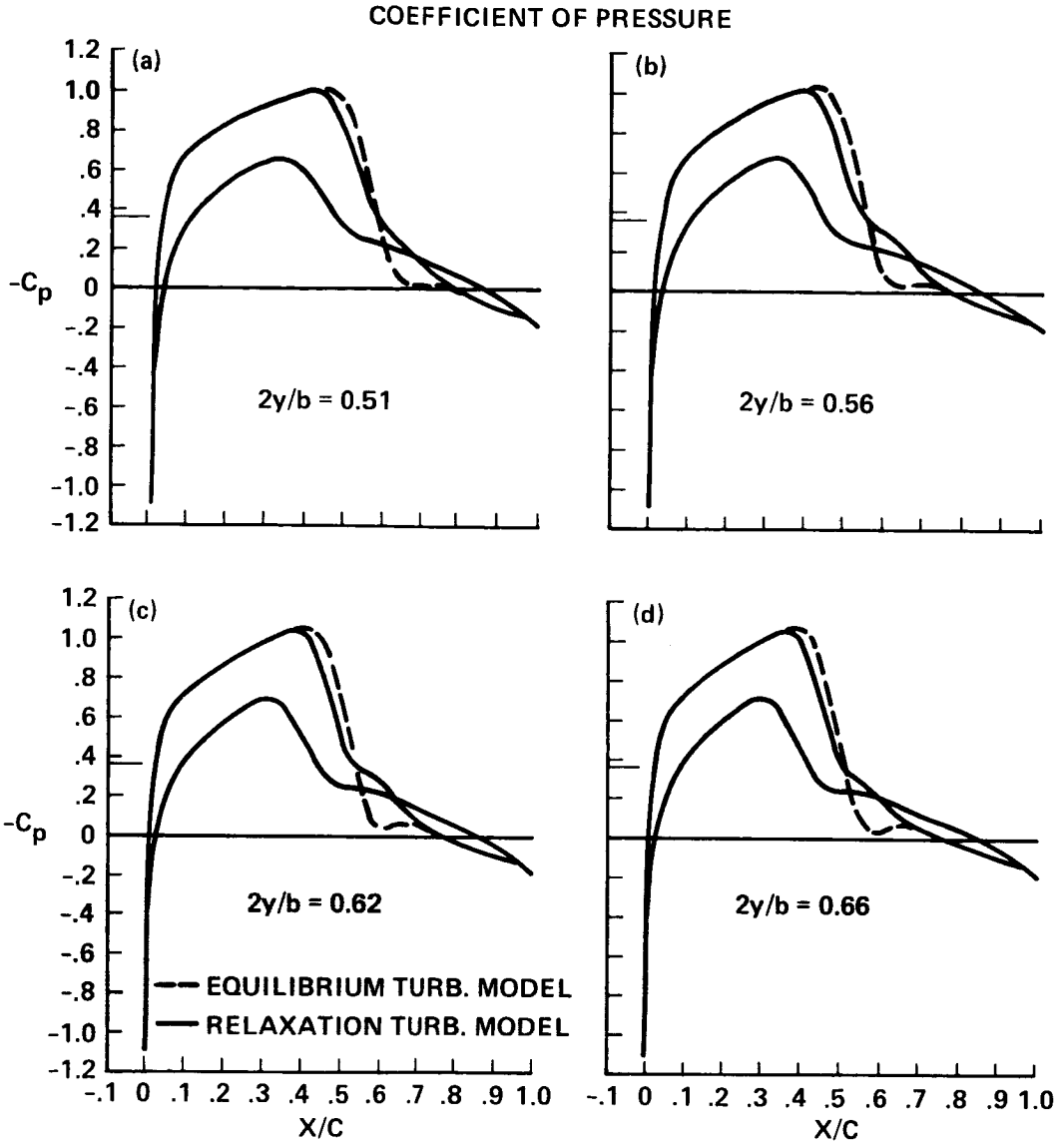

Fig. 26. Comparison of computed pressure coefficents using the baseline and relaxation turbulence models: NACA 0012 airfoil section, $AR = 3$, $\Lambda_{LE} = 20°$, $TR = 1.0$, $M_\infty = 0.826$, $\alpha = 2°$, $Re_c = 8 \times 10^6$, *a*) $2y/b = 0.51$; *b*) $2y/b = 0.56$; *c*) $2y/b = 0.62$; *d*) $2y/b = 0.66$.

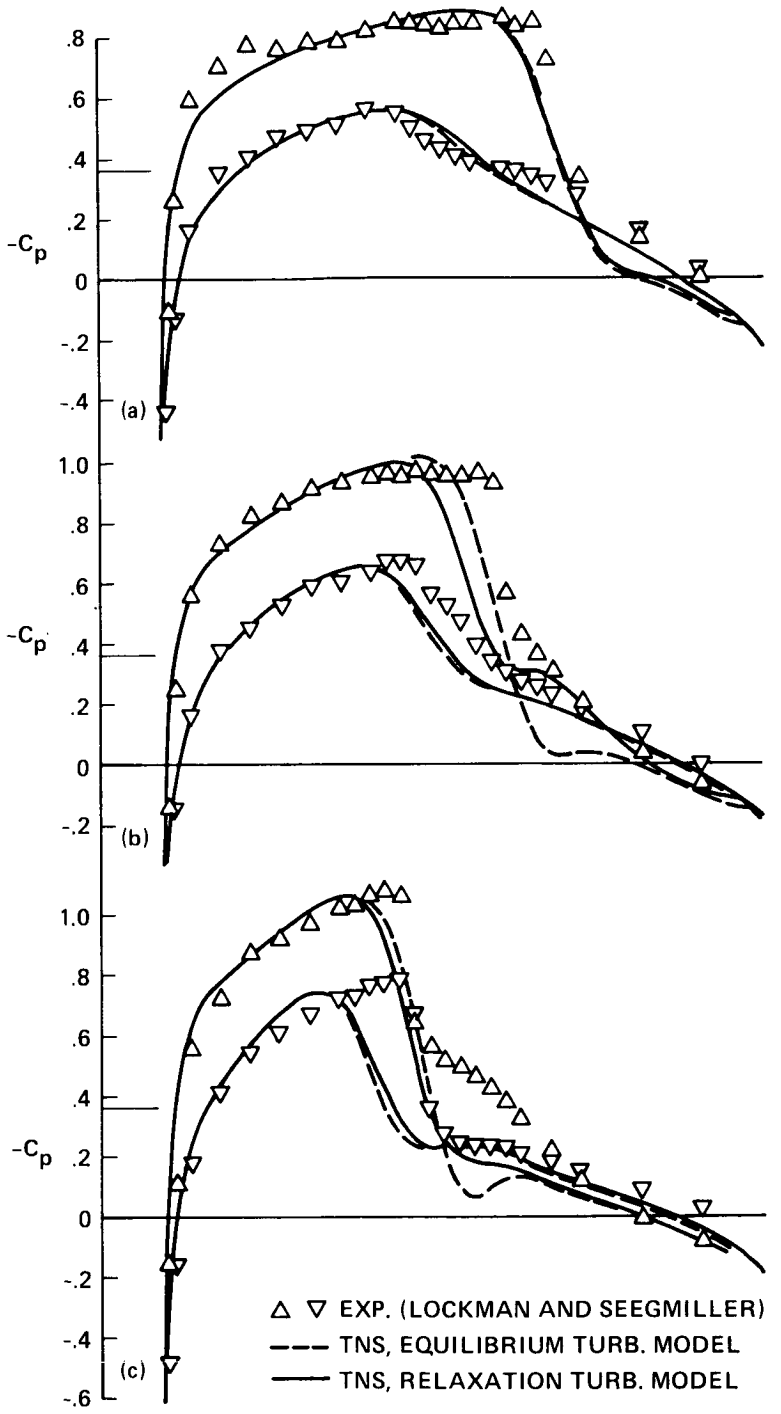

Fig. 27. Comparison of experimental and computed pressure coefficients using different turbulence models: NACA 0012 airfoil section, $AR = 3$, $\Lambda_{LE} = 20°$, $TR = 1.0$, $M_\infty = 0.826$, $\alpha = 2°$, $Re_c = 8 \times 10^6$, *a*) $2y/b = 0.25$; *b*) $2y/b = 0.50$; *c*) $2y/b = 0.78$.

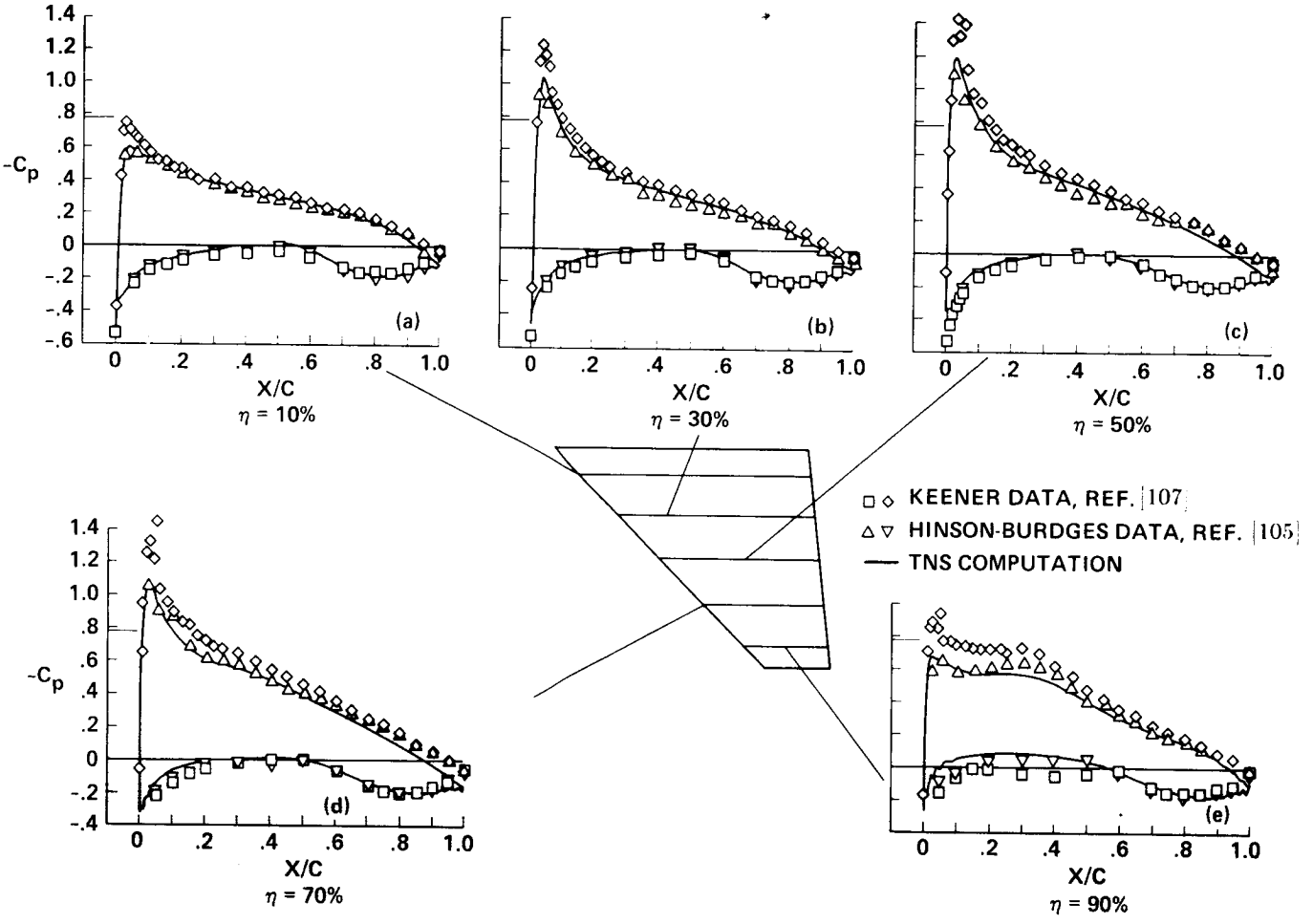

Fig. 28. Comparison of experimental and computed pressure coefficients for WING C: $M_\infty = 0.70$, $\alpha = 5°$, $Re_{m.a.c.} = 6.8 \times 10^6$.

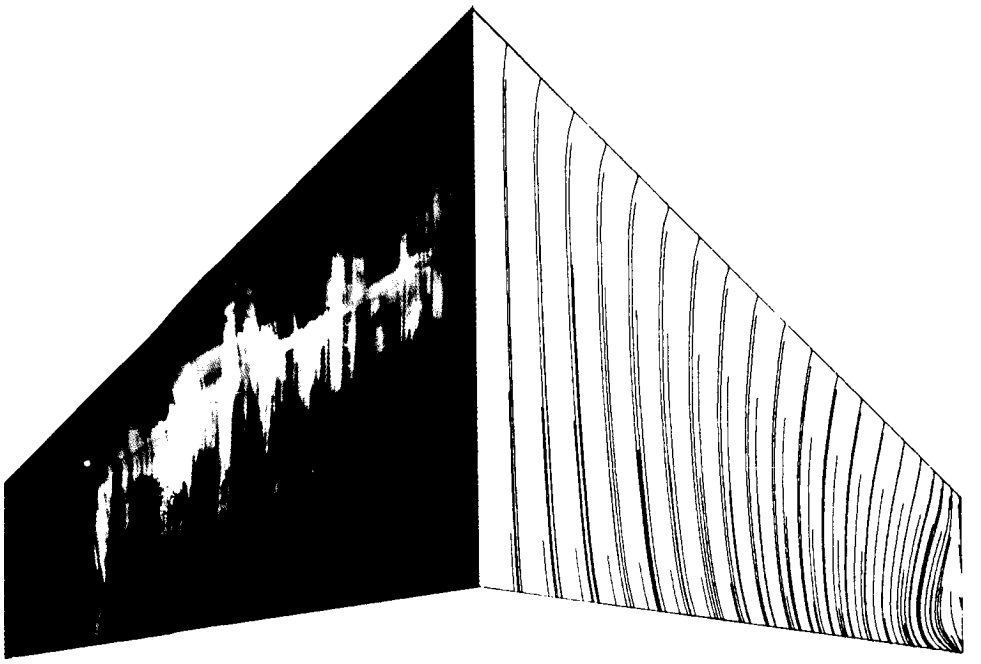

Fig. 29. An experimental oil-flow picture (from Ref. [107]) and computed upper surface skin-friction lines for WING C: $M_\infty = 0.70$, $\alpha = 2°$, $Re_{m.a.c.} = 6.8 \times 10^6$.

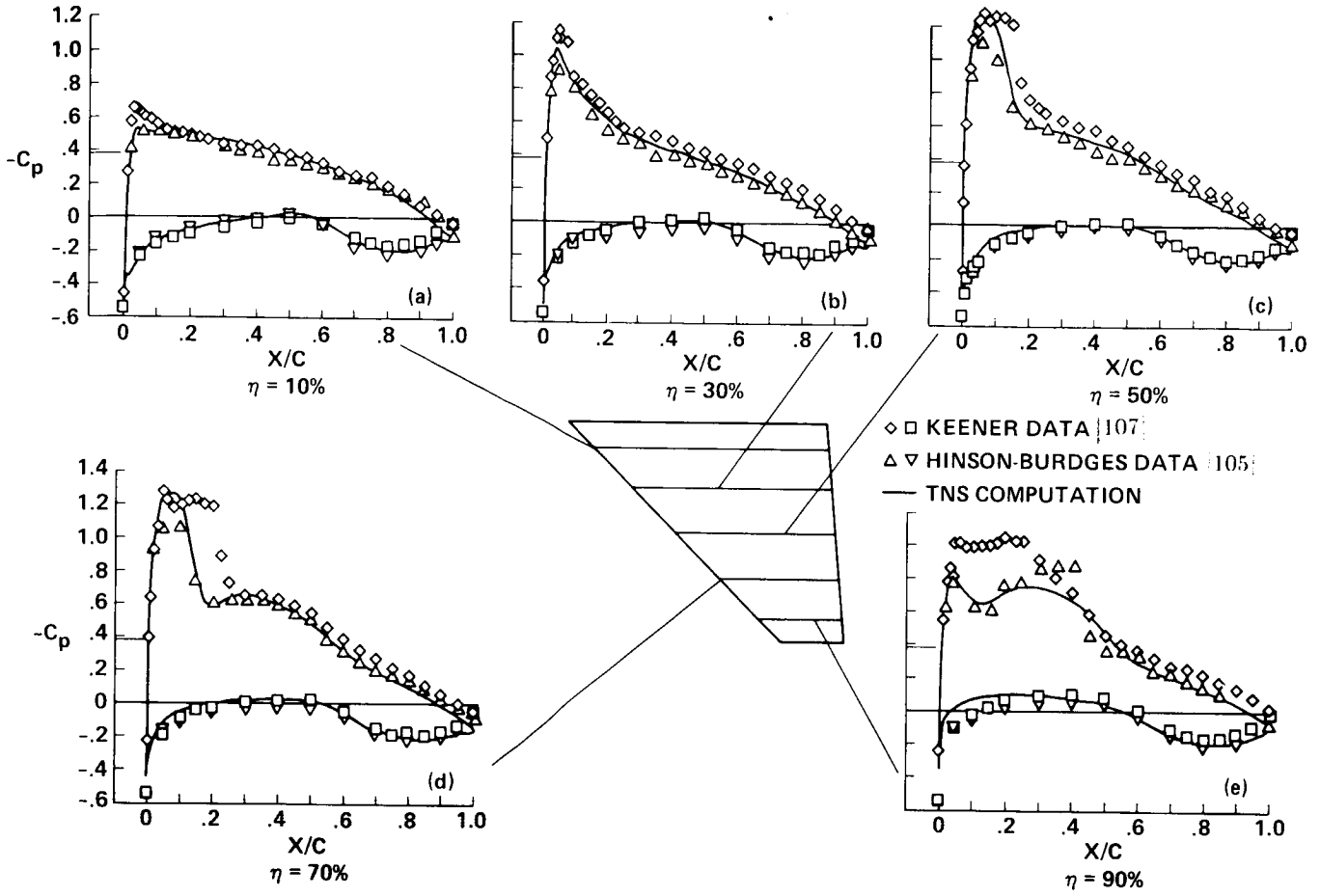

Fig. 30. Comparison of experimental and computed pressure coefficients for WING C: $M_\infty = 0.82$, $\alpha = 5°$, $Re_{m.a.c.} = 6.8 \times 10^6$.

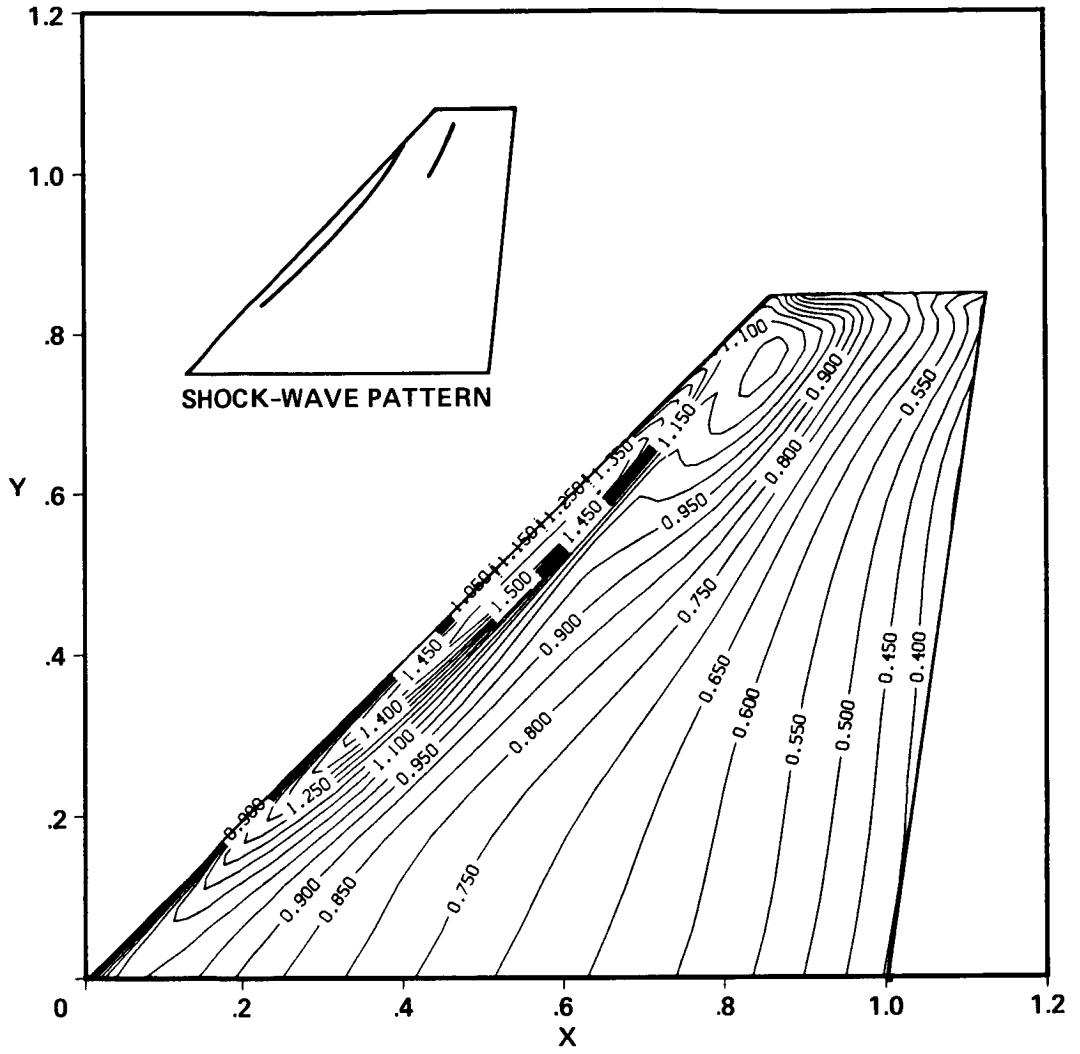

Fig. 31. Mach number contours on the upper surface of WING C: $M_\infty = 0.82$, $\alpha = 5°$, $Re_{m.a.c.} = 6.8 \times 10^6$.

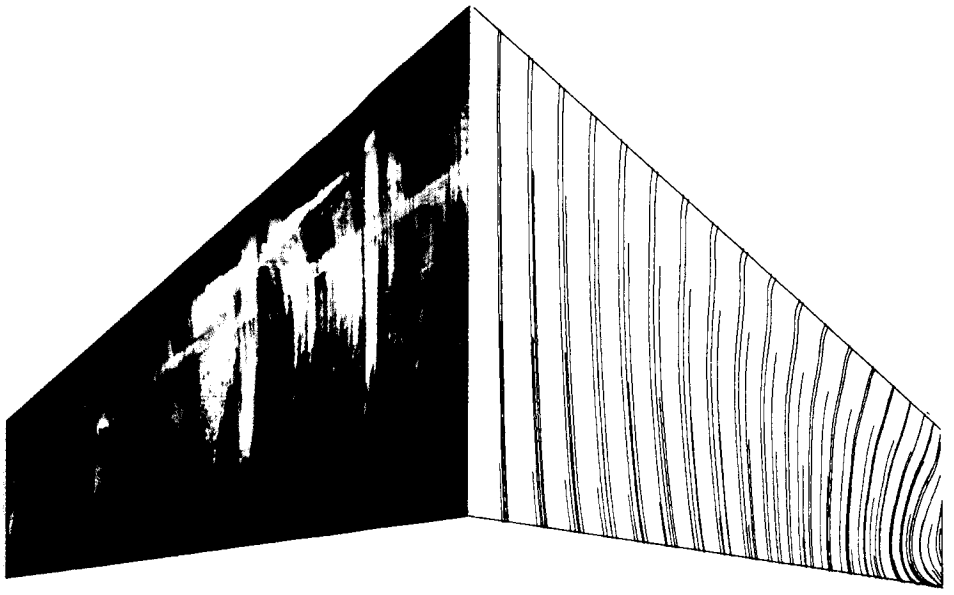

Fig. 32. Experimental oil-flow picture (from Ref. [107]) and computed upper surface skin-friction lines for WING C: $M_\infty = 0.82$, $\alpha = 5°$, $Re_{m.a.c.} = 6.8 \times 10^6$.

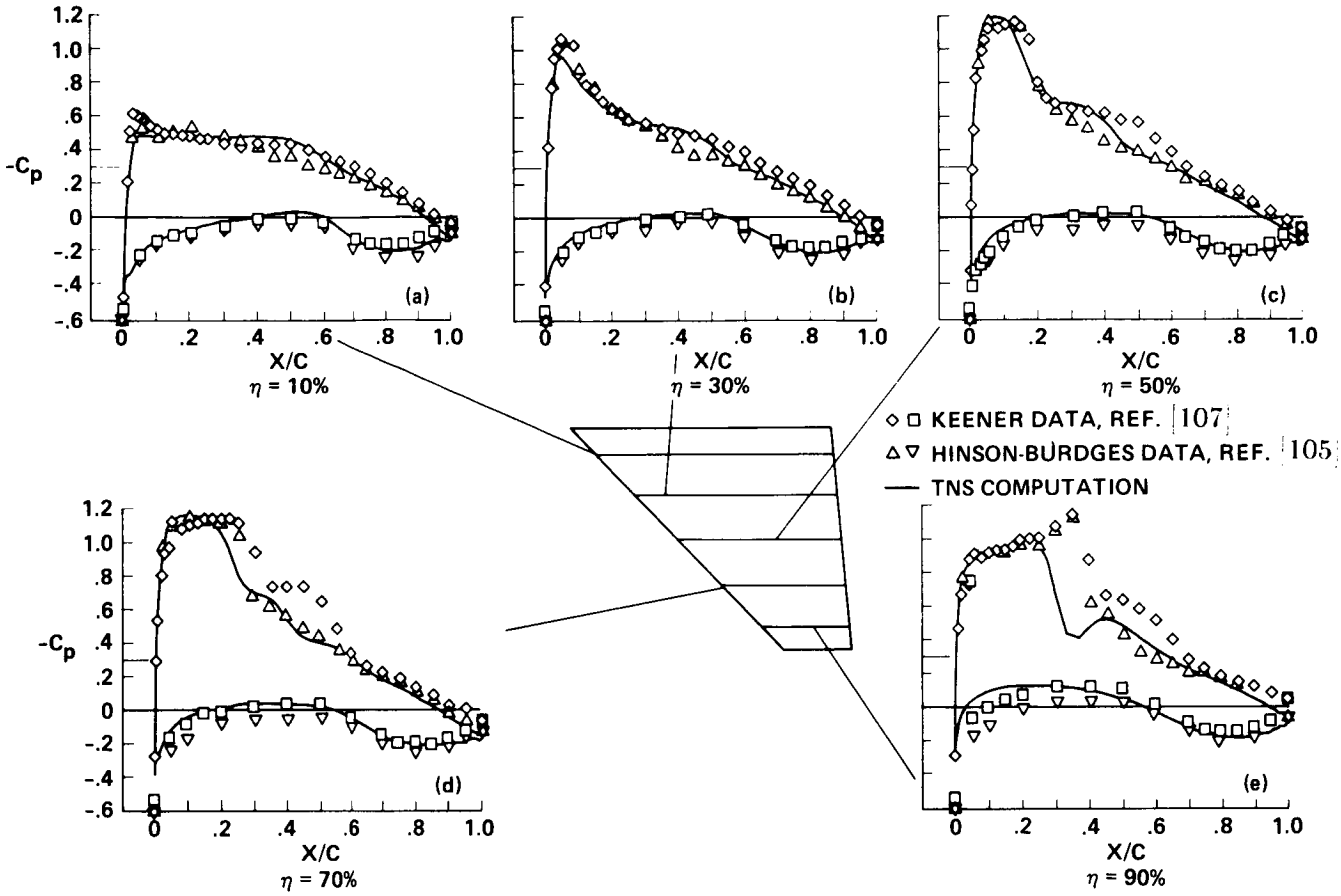

Fig. 33. Comparison of experimental and computed pressure coefficients for WING C: $M_\infty = 0.85$, $\alpha = 5^\circ$, $Re_{m.a.c.} = 6.8 \times 10^6$.

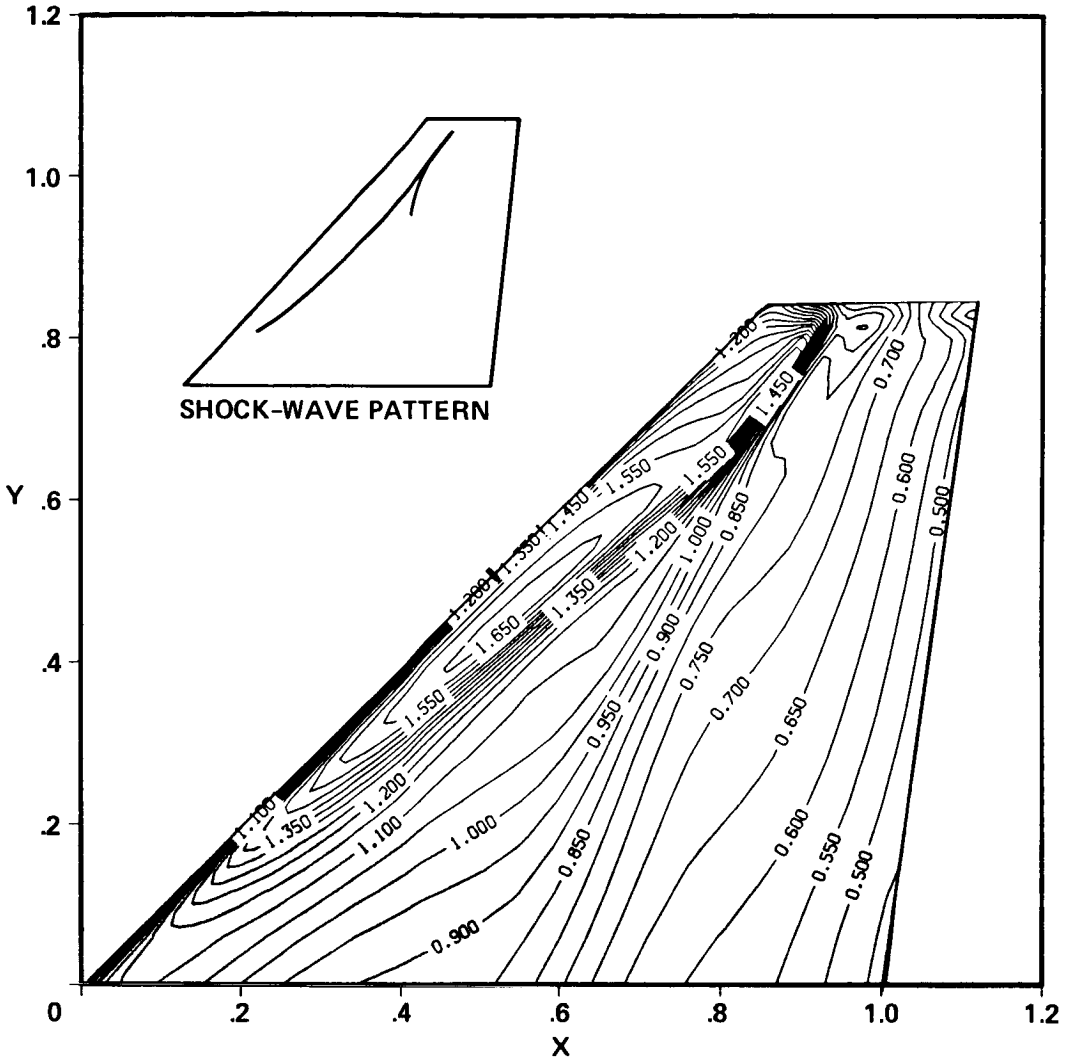

Fig. 34. Mach number contours on the upper surface of WING C: $M_\infty = 0.85$, $\alpha = 5°$, $Re_{m.a.c.} = 6.8 \times 10^6$.

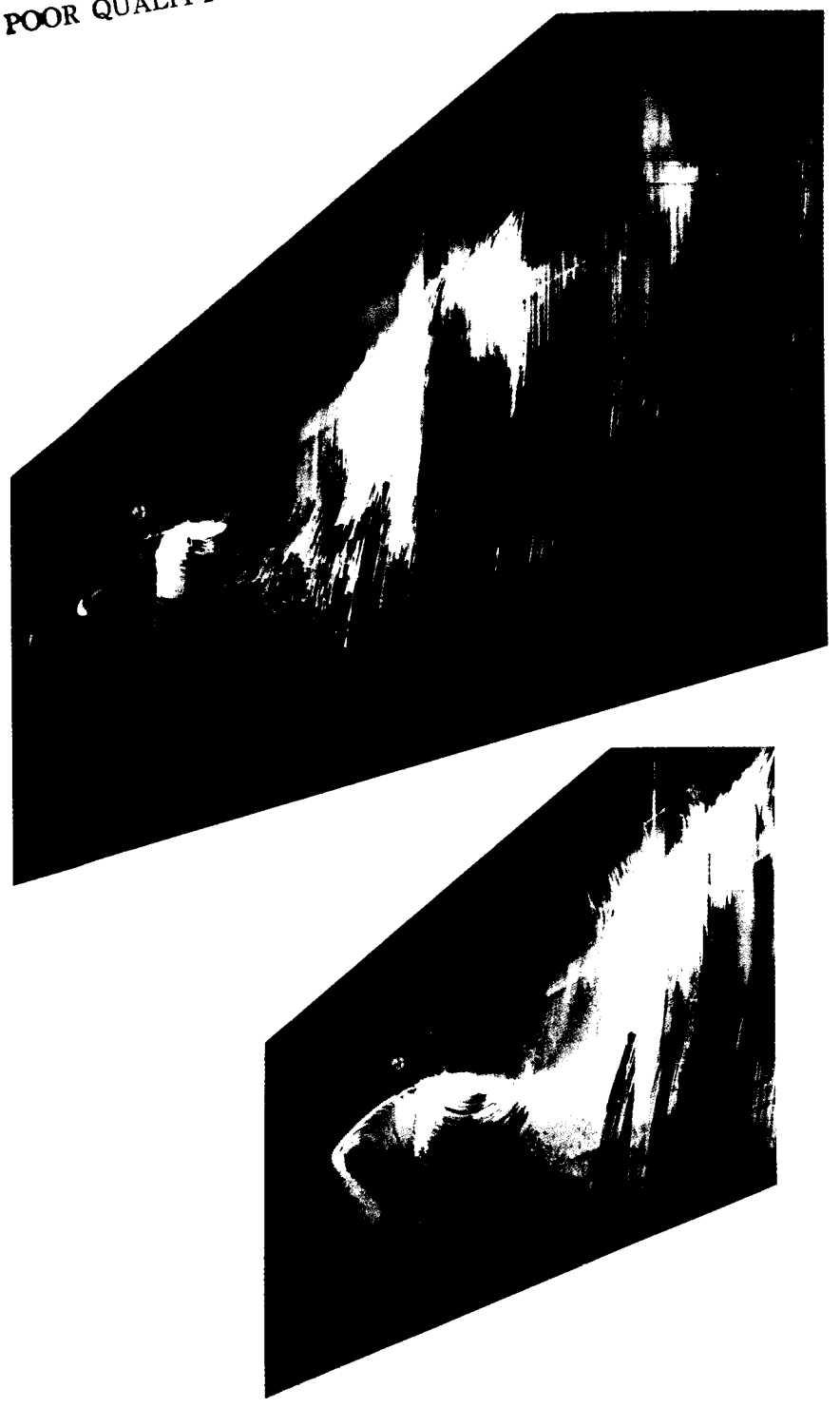

Fig. 35. Experimental oil-flow picture (from Ref. [107]) and an expanded view of the counter-rotating vortices for WING C: $M_\infty = 0.85$, $\alpha = 5°$, $Re_{m.a.c.} = 6.8 \times 10^6$.

C-2

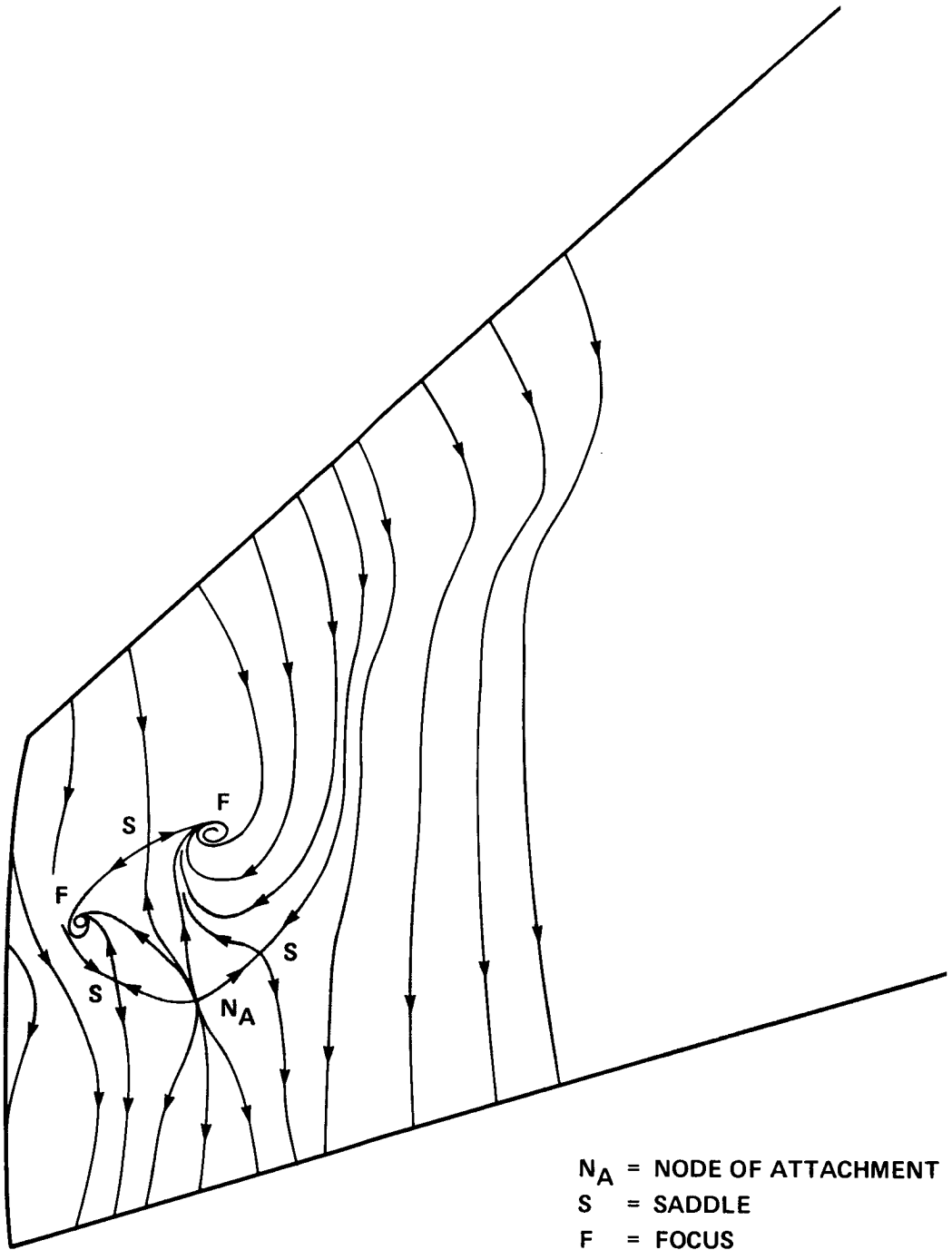

Fig. 36. "Postulated" skin-friction lines for the WING C case shown in Fig. 35 ($M_\infty = 0.85$).

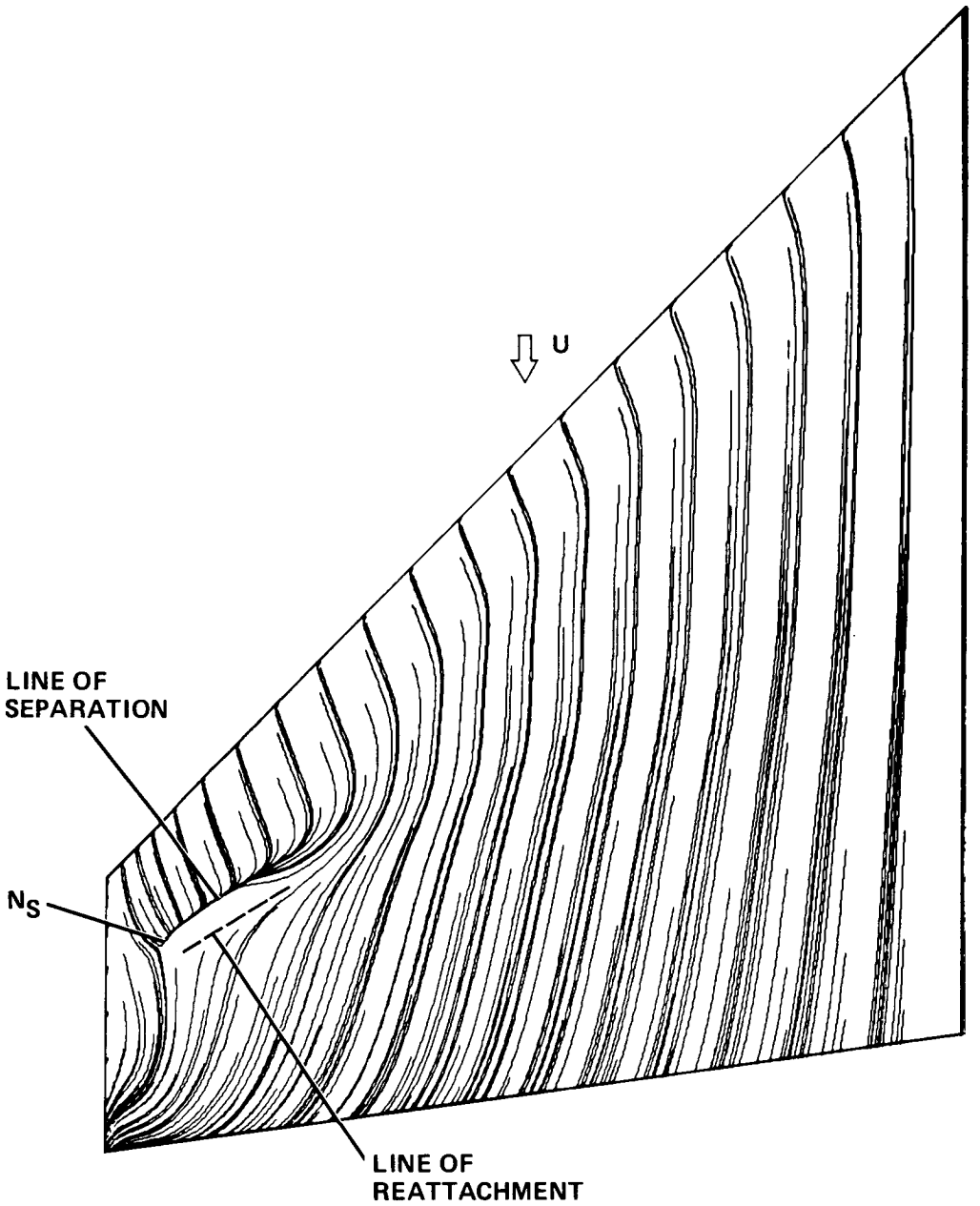

Fig. 37. Computed skin-friction lines for WING C upper surface: $M_\infty = 0.85$, $\alpha = 5.9°$, $Re_{m.a.c.} = 6.8 \times 10^6$.

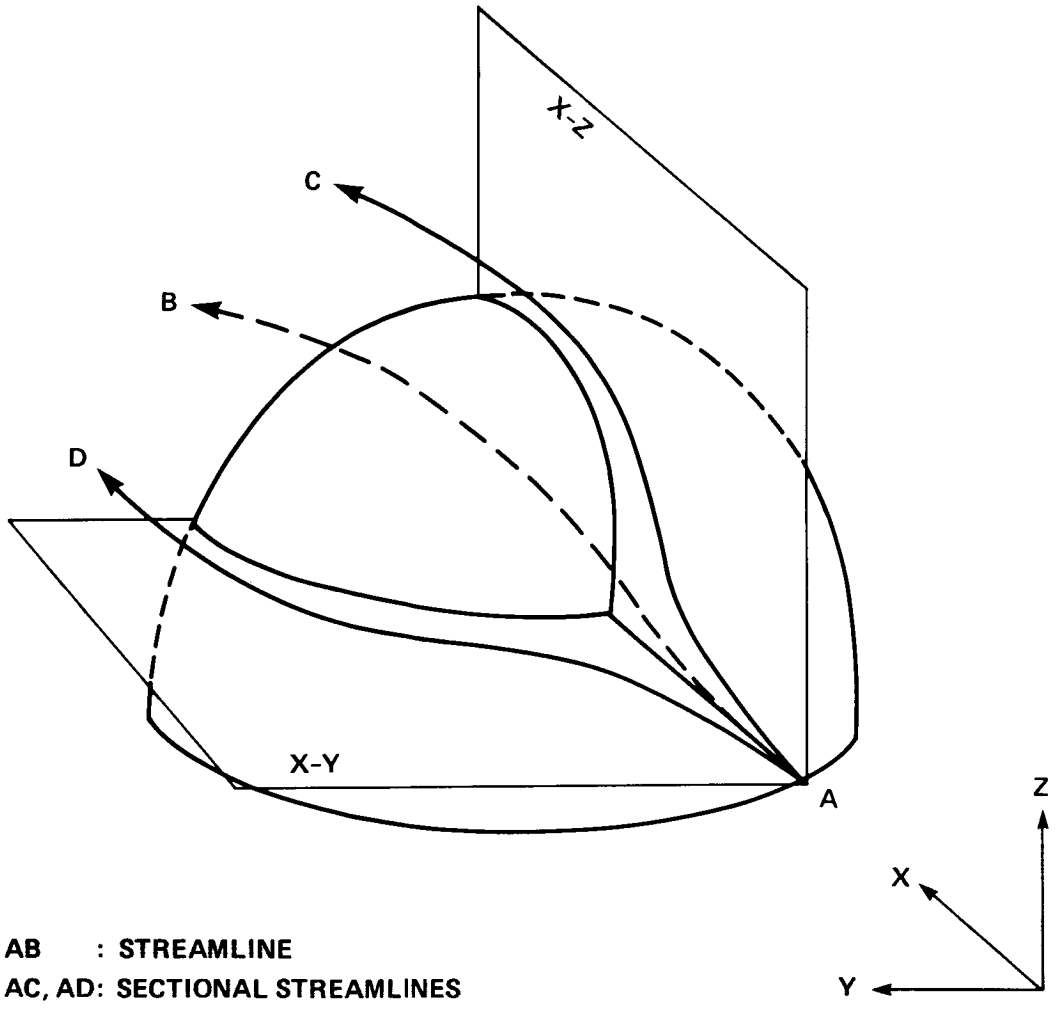

Fig. 38. Illustration of "streamlines" and "sectional streamlines."

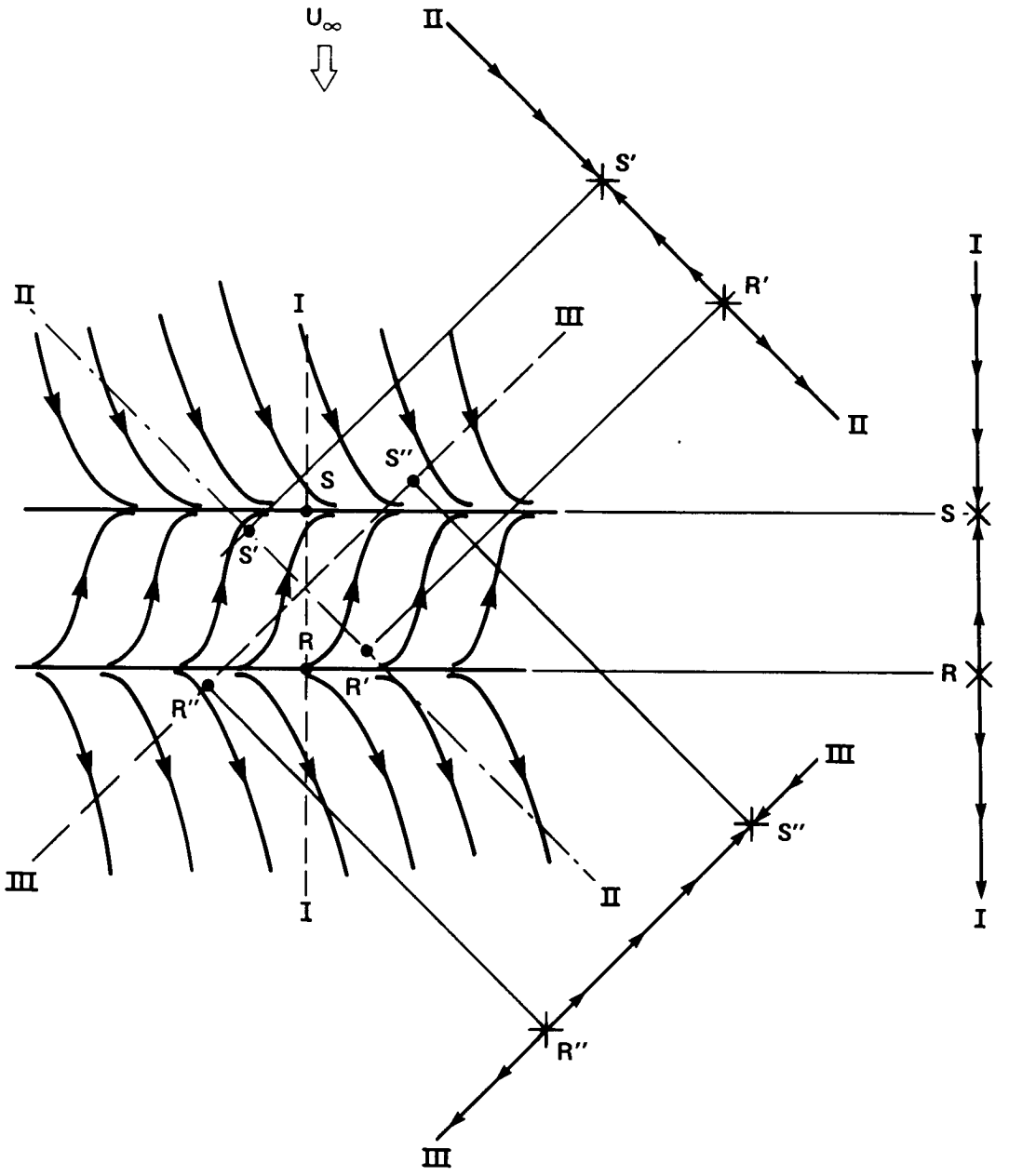

Fig. 39. Illustration of obtaining different separation and reattachment points for a "bubble" depending upon the viewing angle.

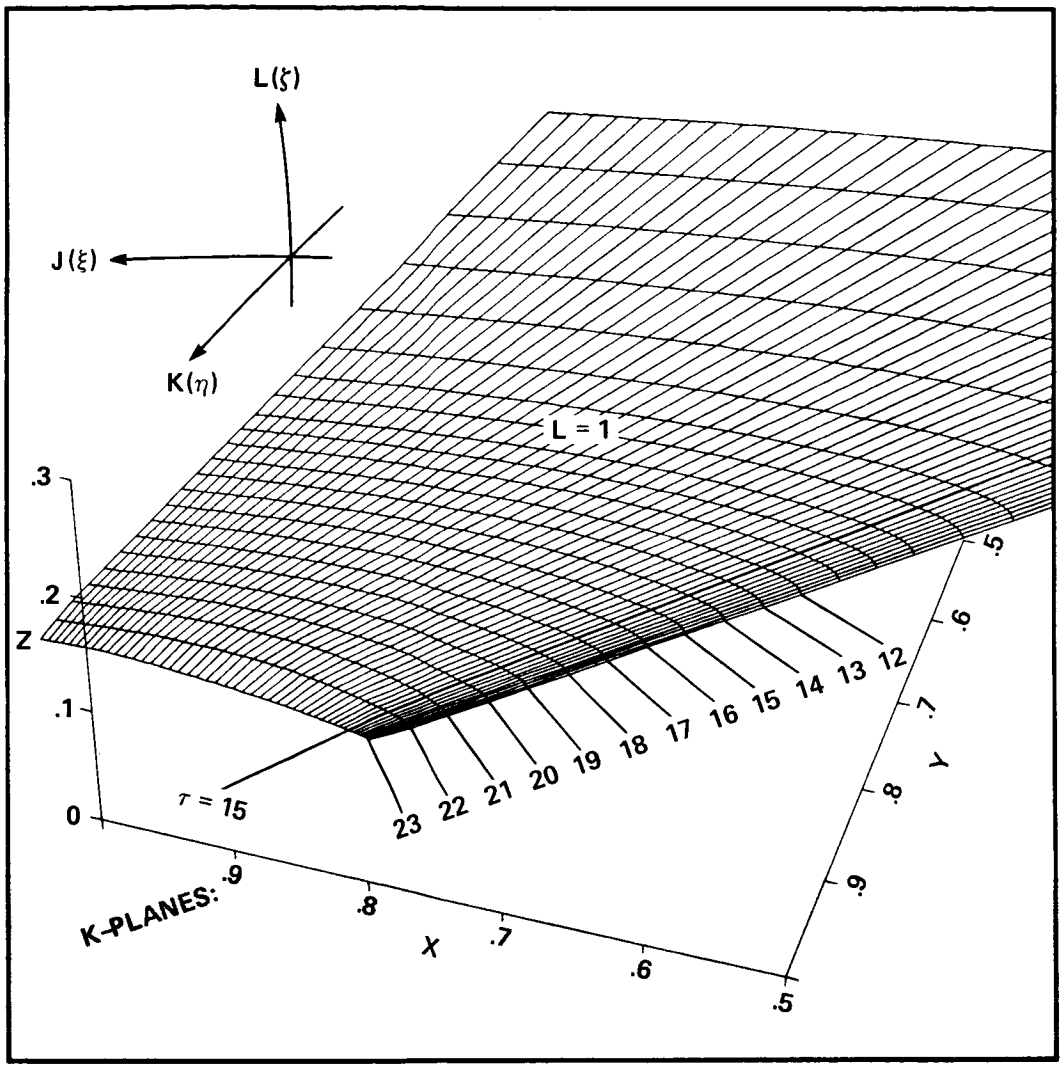

Fig. 40. Perspective view of the WING C surface grid and index designations for the computational planes.

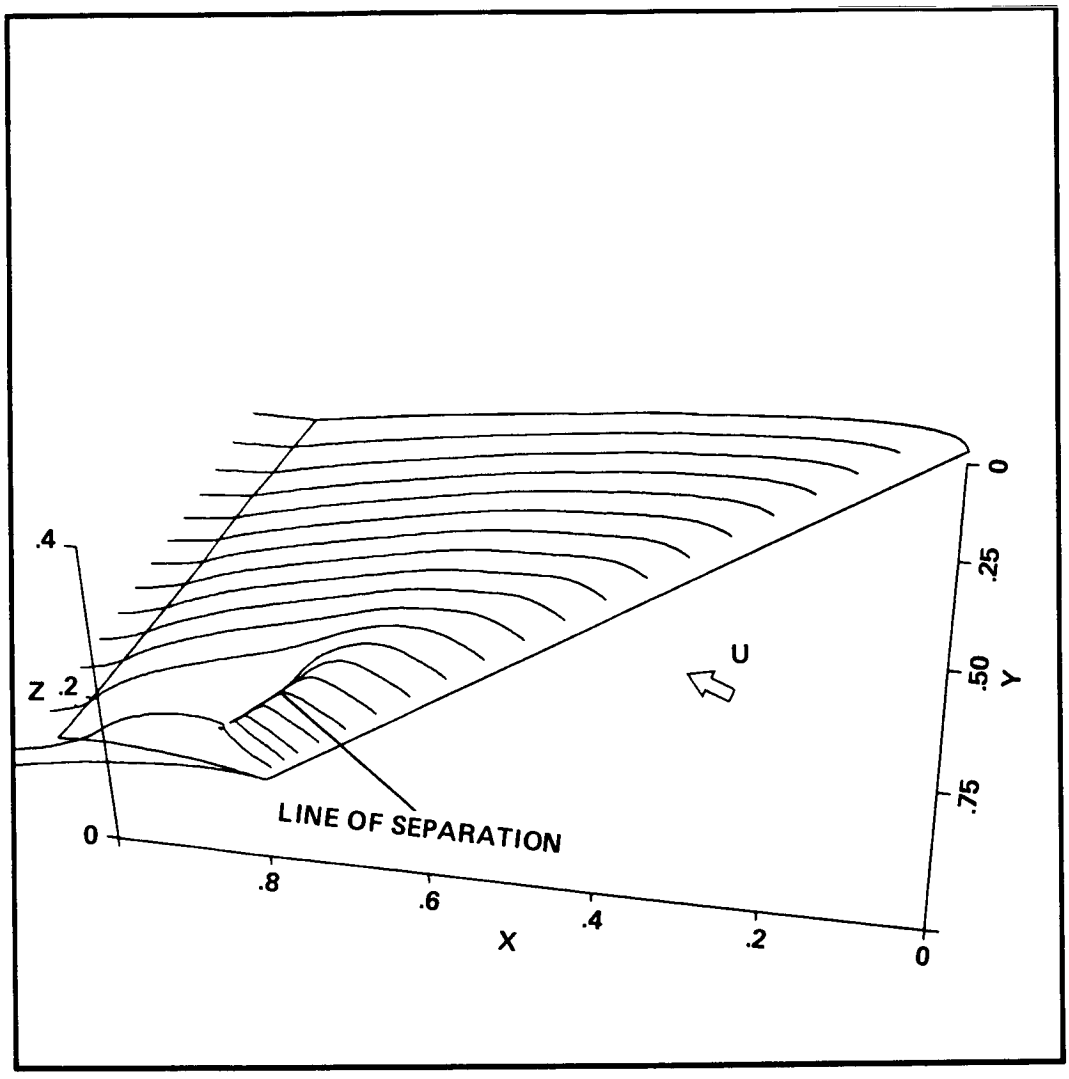

Fig. 41. Perspective view of computed skin-friction lines for WING C: $M_\infty = 0.85$, $\alpha = 5.9°$, $Re_{m.a.c.} = 6.8 \times 10^6$.

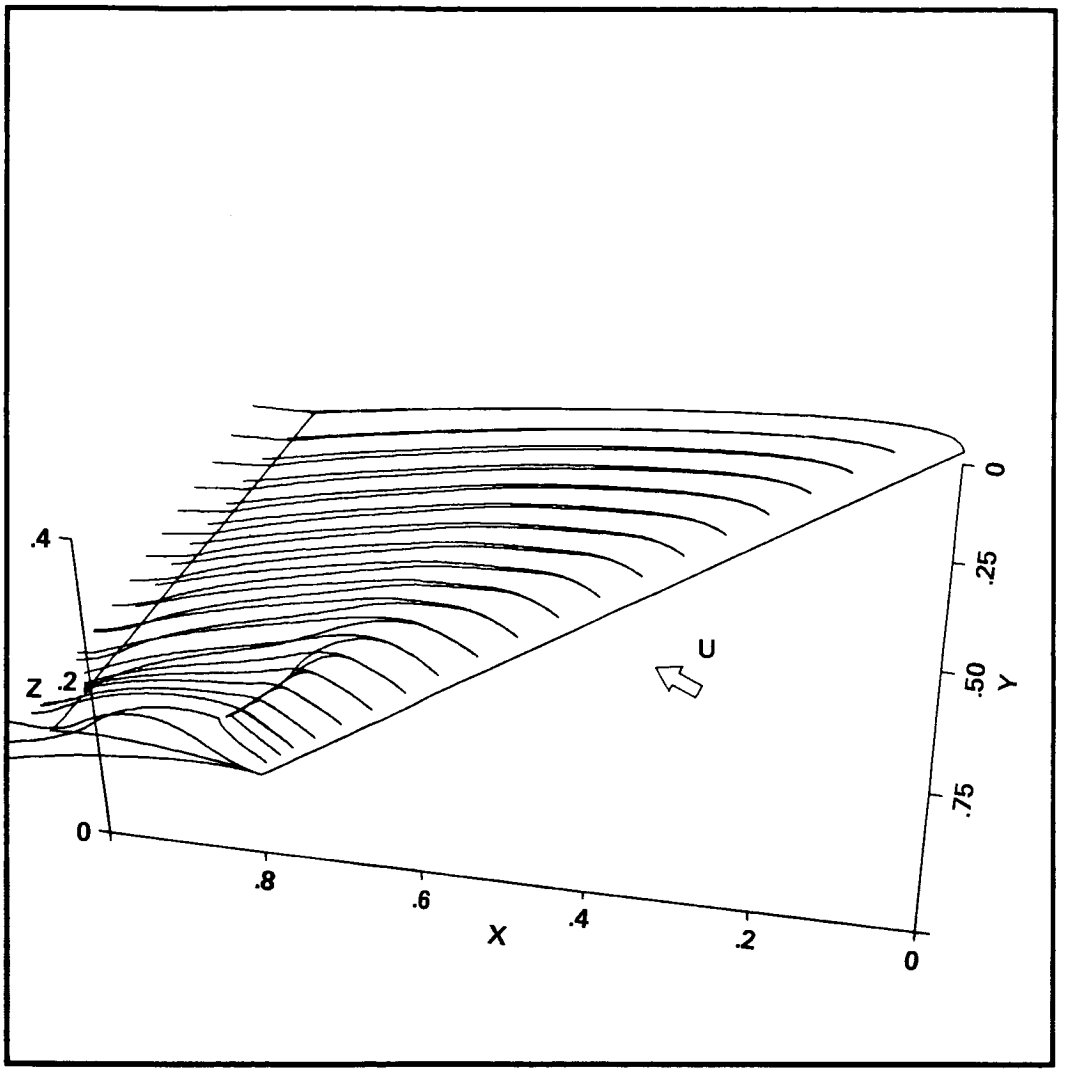

Fig. 42. Perspective view of computed "streamlines" and "sectional streamlines" for WING C: $M_\infty = 0.85$, $\alpha = 5.9°$, $Re_{m.a.c.} = 6.8 \times 10^6$.

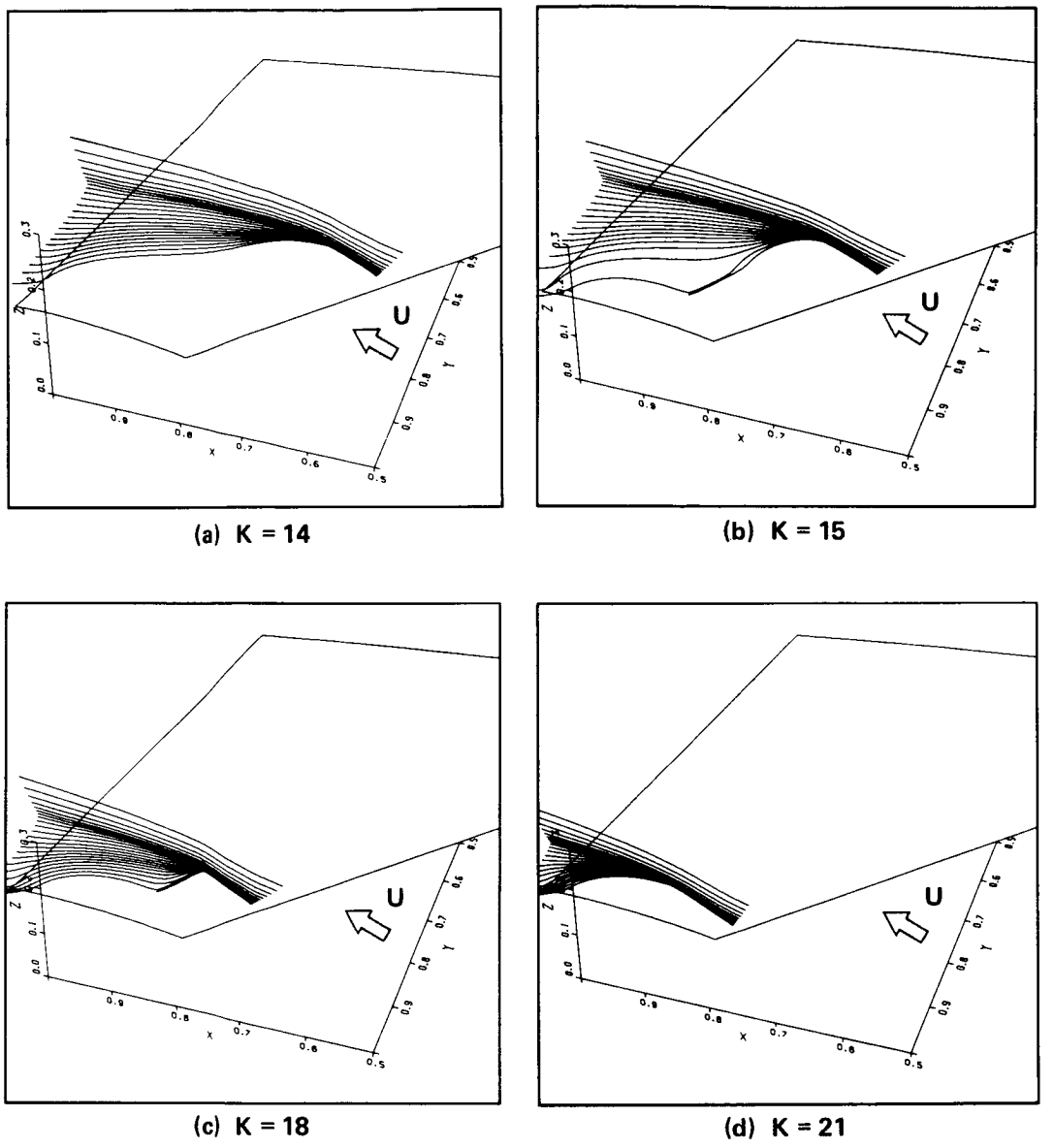

Fig. 43. Sectional streamlines on JK (body-parallel) computational planes obtained by "releasing" particles at different L levels for a fixed value of J ($M_\infty = 0.85$).

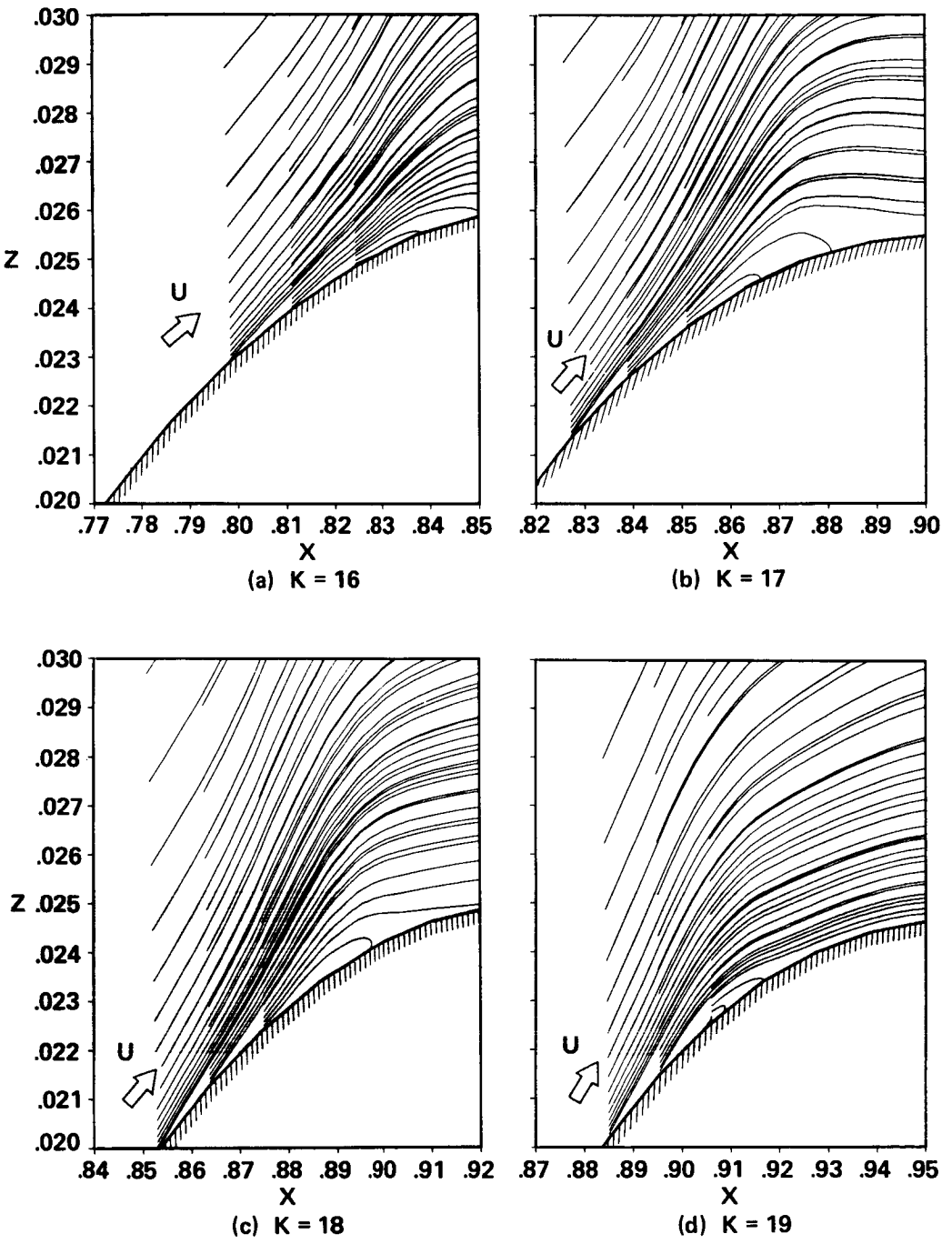

Fig. 44. Sectional streamlines on JL (cross-sectional) computational planes obtained by "releasing" particles at different L levels from streamwise stations through the separation zone ($M_\infty = 0.85$). (Note the expanded z-scale.)

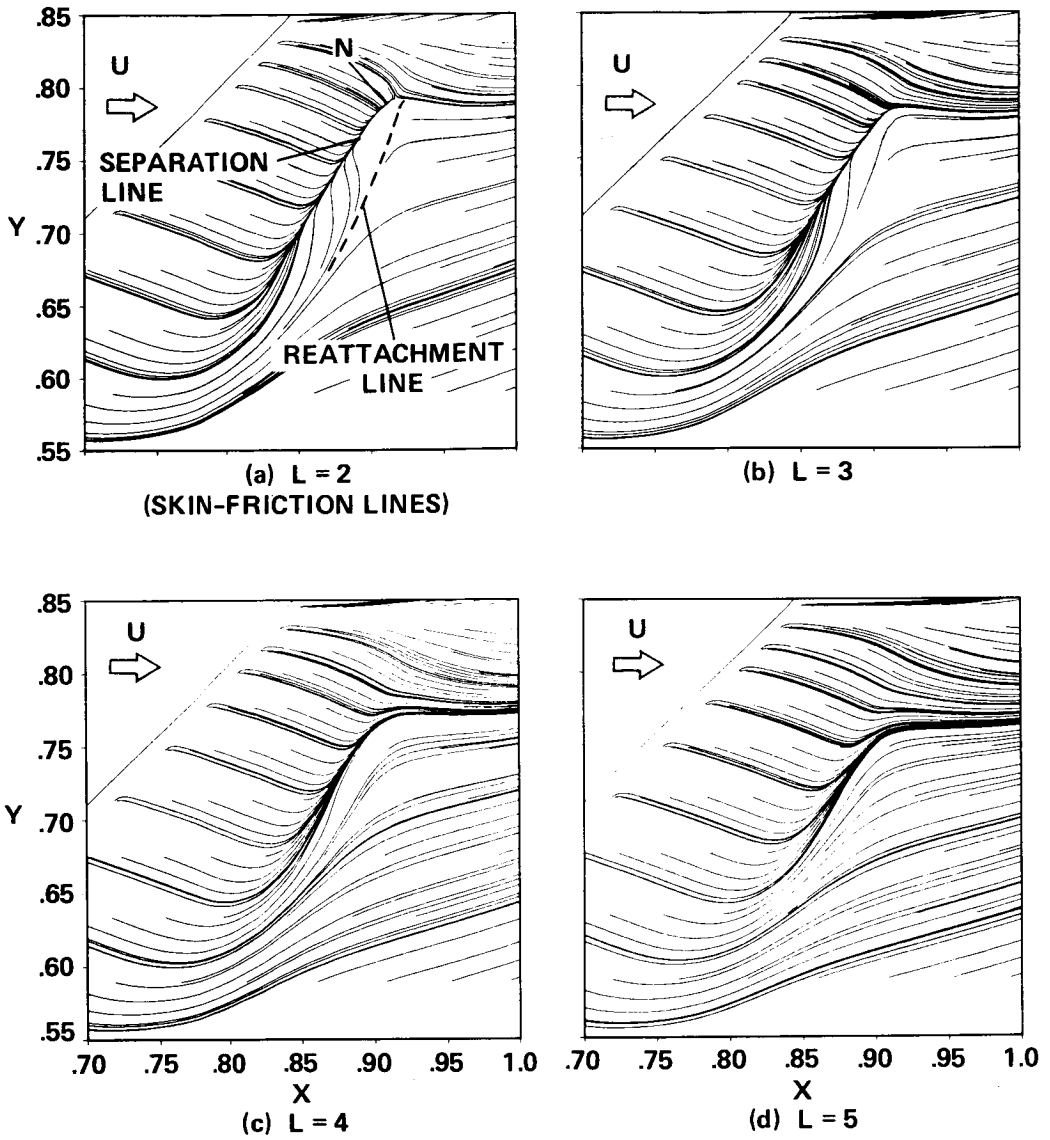

Fig. 45. Sectional streamlines on JK (body-parallel) computational planes. Particles are "released" from a line parallel to the leading-edge ($M_\infty = 0.85$).

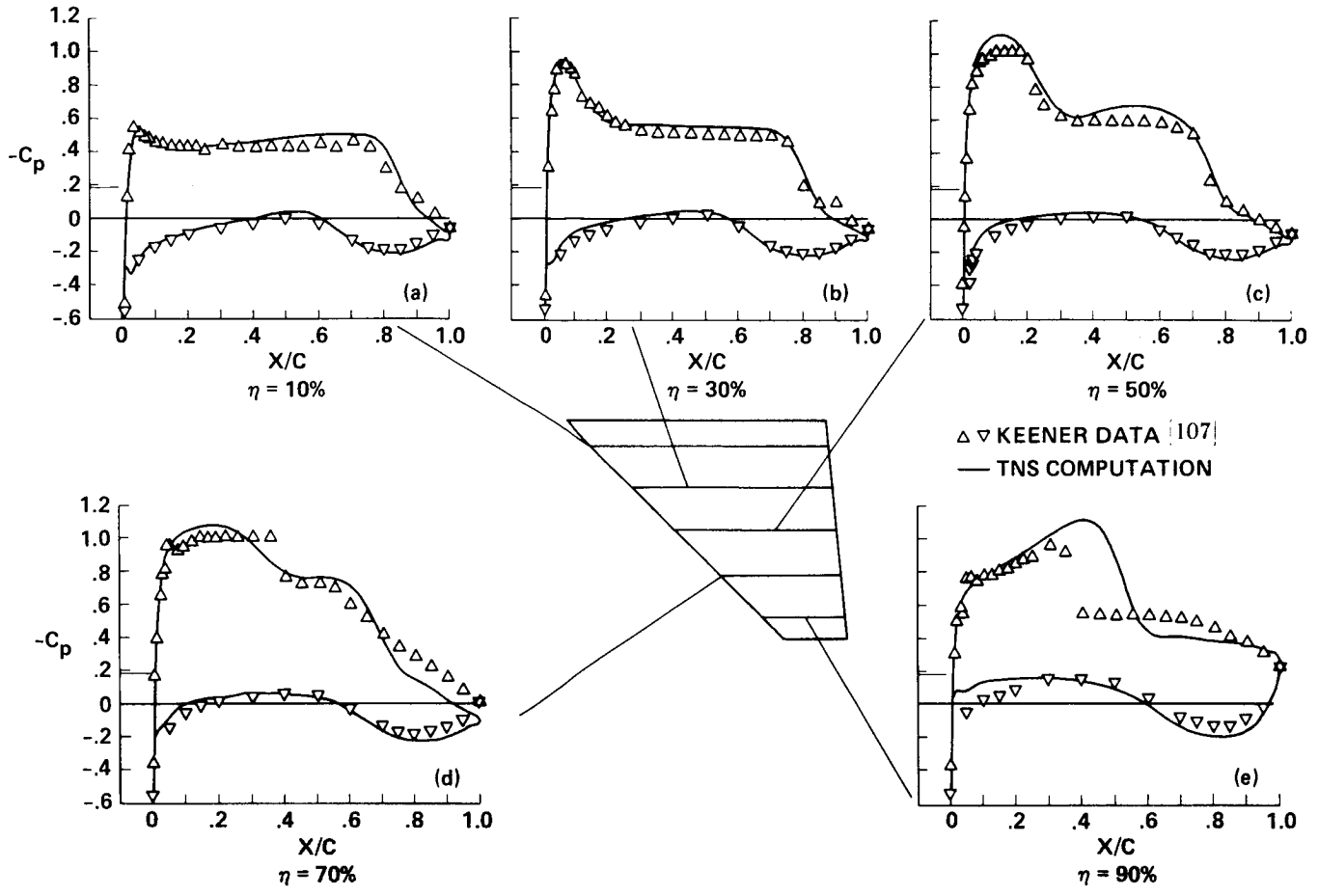

Fig. 46. Comparison of experimental and computed pressure coefficients for WING C: $M_\infty = 0.90$, $\alpha = 5°$, $Re_{m.a.c.} = 6.8 \times 10^6$.

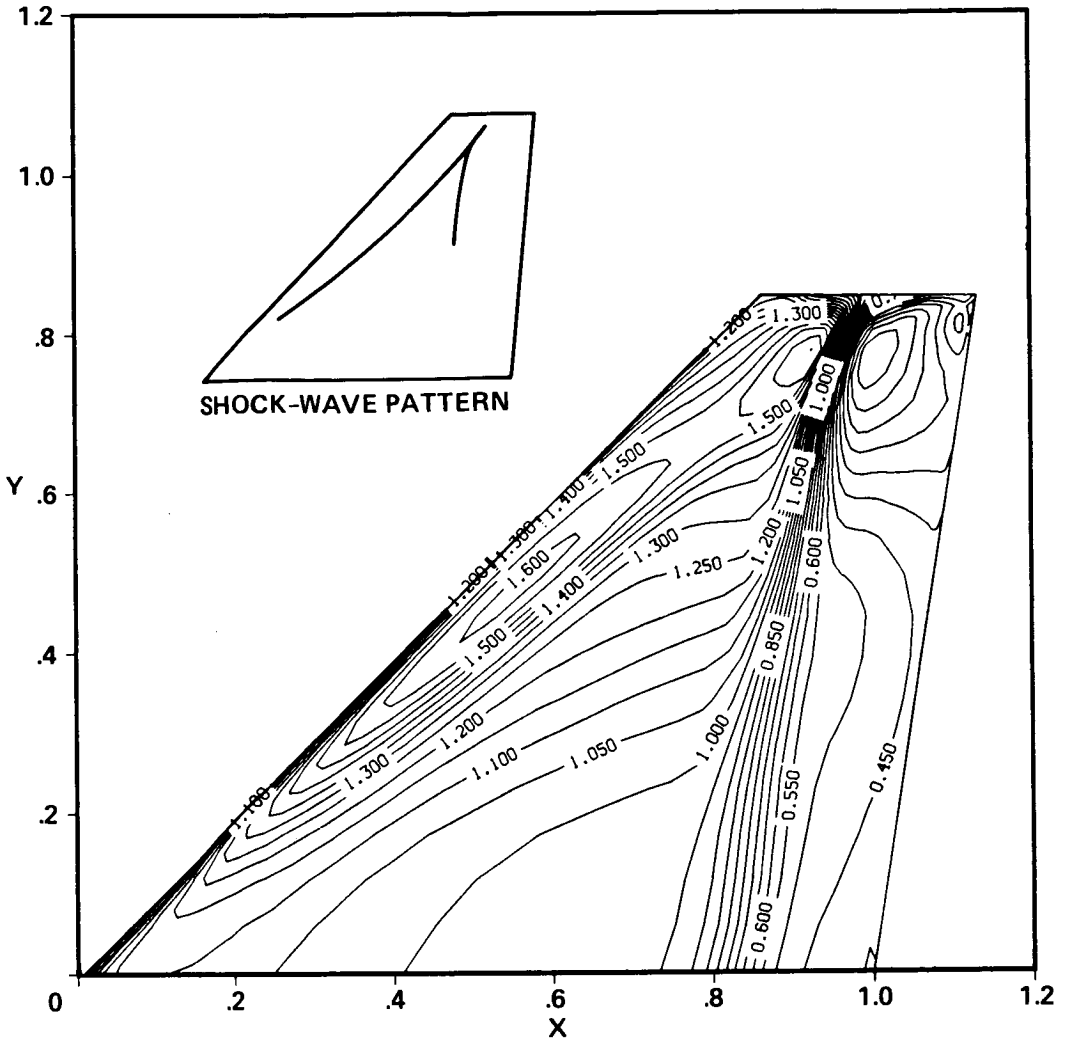

Fig. 47. Mach number contours on the upper surface of WING C: $M_\infty = 0.90$, $\alpha = 5°$, $Re_{m.a.c.} = 6.8 \times 10^6$.

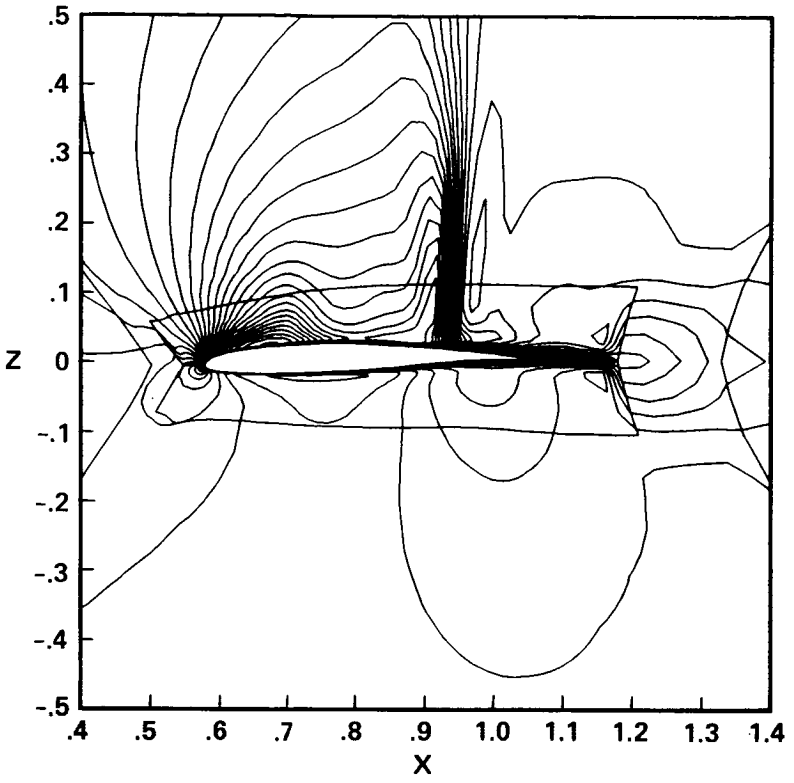

Fig. 48. Cross-sectional Mach number contours for WING C at $2y/b = 0.77$: $M_\infty = 0.90$, $\alpha = 5°$, $Re_{m.a.c.} = 6.8 \times 10^6$.

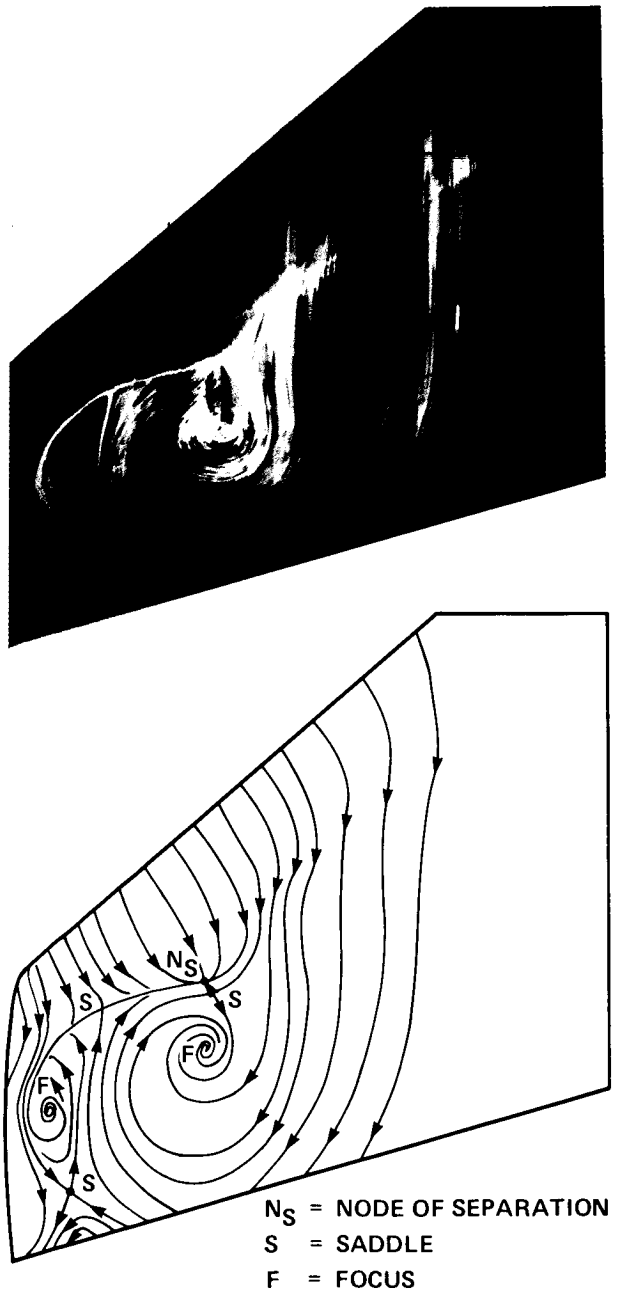

Fig. 49. Experimental oil-flow picture(from Ref. [107]) and "postulated" skin-friction lines for WING C: $M_\infty = 0.90$, $\alpha = 5°$, $Re_{m.a.c.} = 6.8 \times 10^6$.

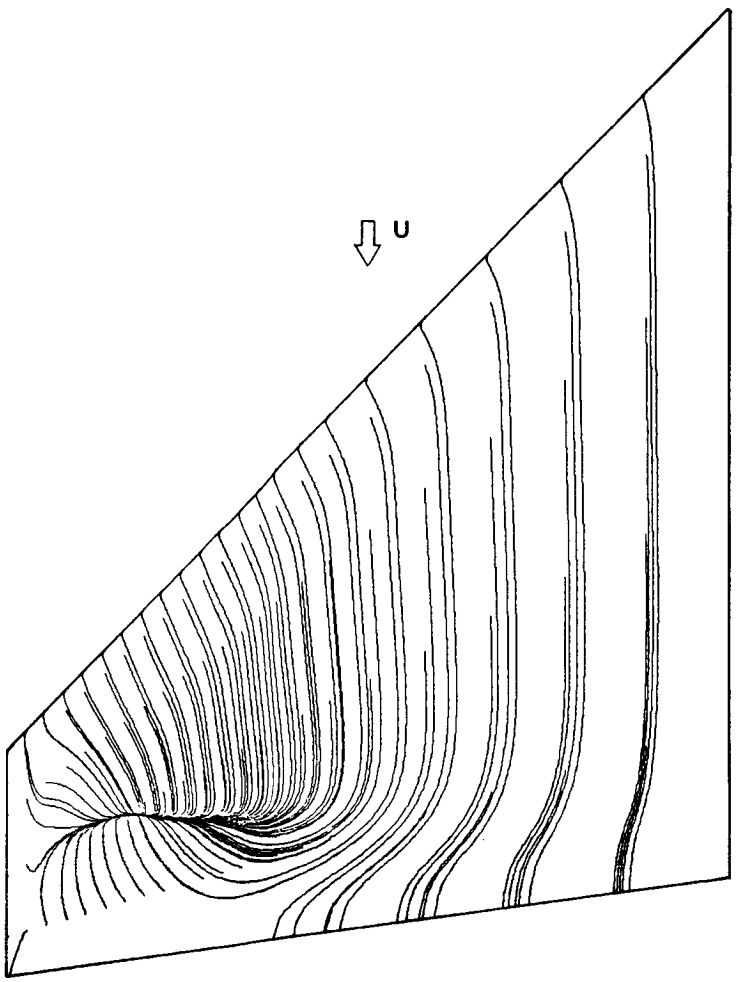

Fig. 50. Computed skin-friction lines for WING C upper surface: $M_\infty = 0.90$, $\alpha = 5.0°$, $Re_{m.a.c.} = 6.8 \times 10^6$.

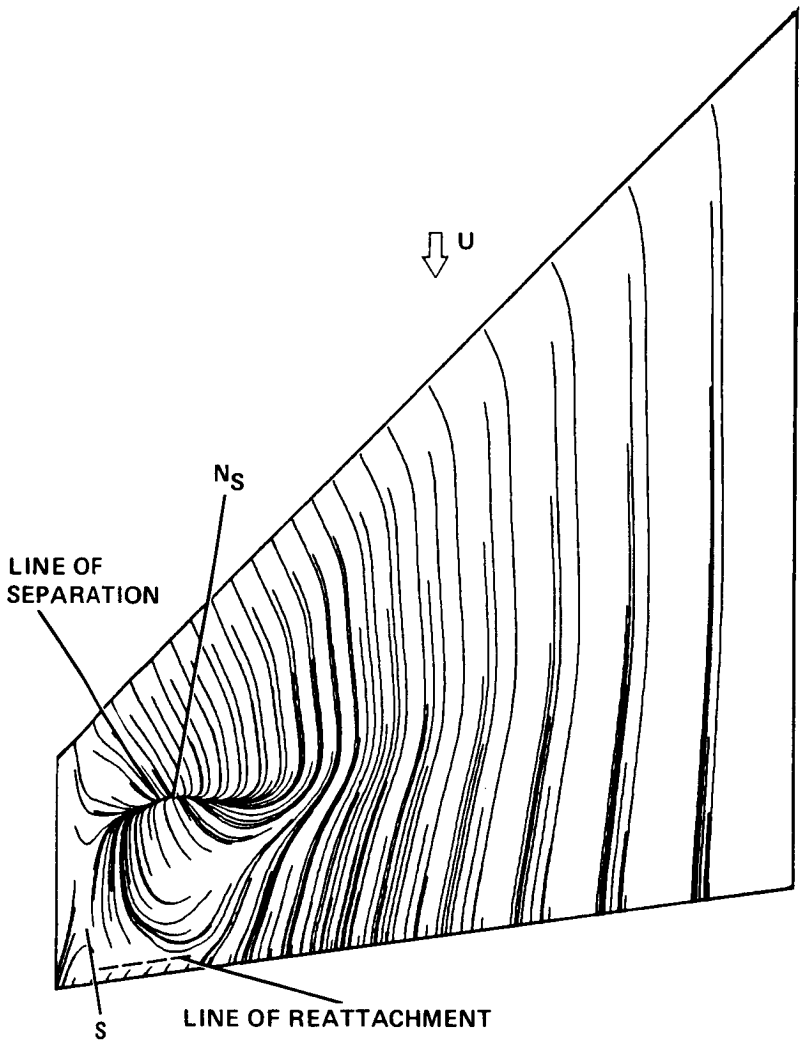

Fig. 51. Computed skin-friction lines for WING C upper surface: $M_\infty = 0.88$, $\alpha = 5.0°$, $Re_{m.a.c.} = 6.8 \times 10^6$.

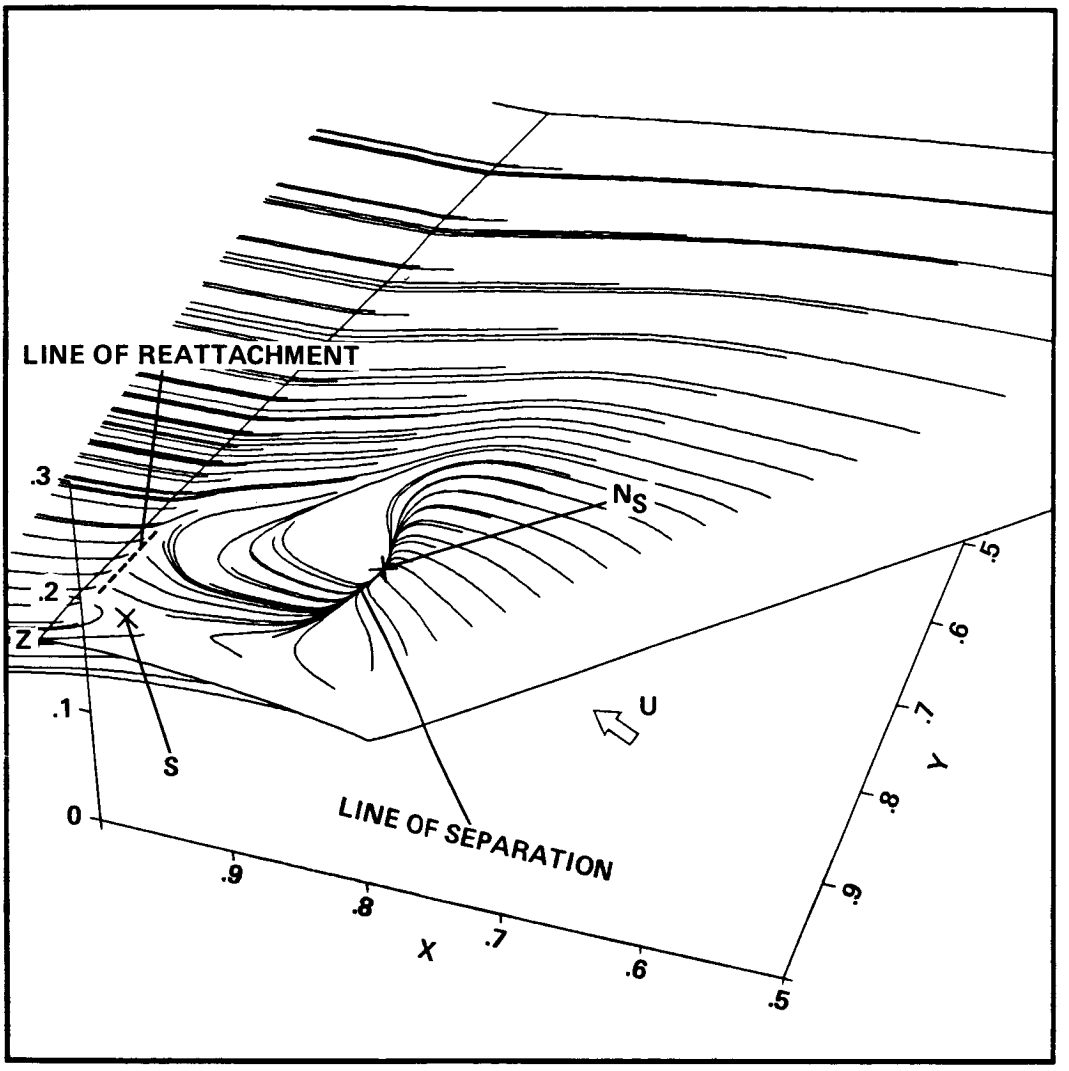

Fig. 52. Perspective view of computed skin-friction lines for WING C: $M_\infty = 0.88$, $\alpha = 5.0°$, $Re_{m.a.c.} = 6.8 \times 10^6$.

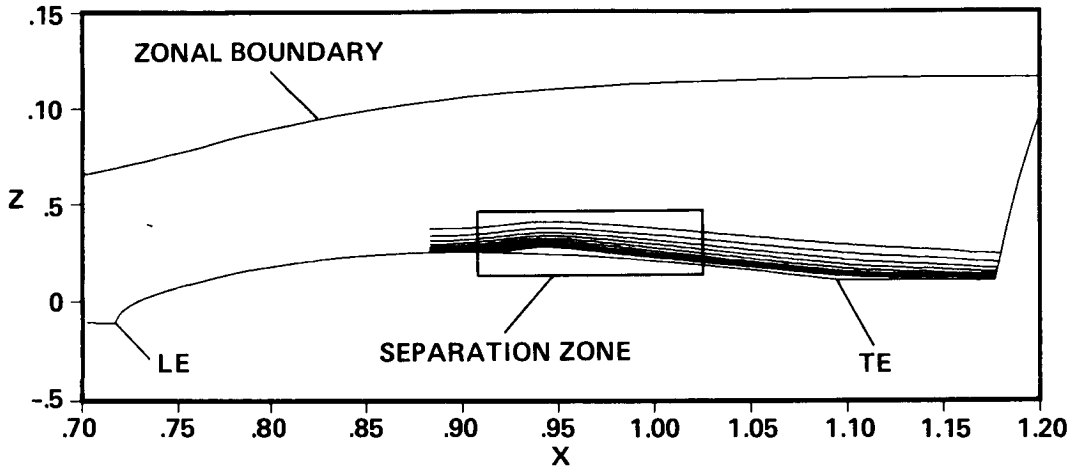

Fig. 53. Sectional streamlines at the K=17 (cross-sectional) computational plane obtained by "releasing" particles at different levels from a station upstream of separation ($M_\infty = 0.88$).

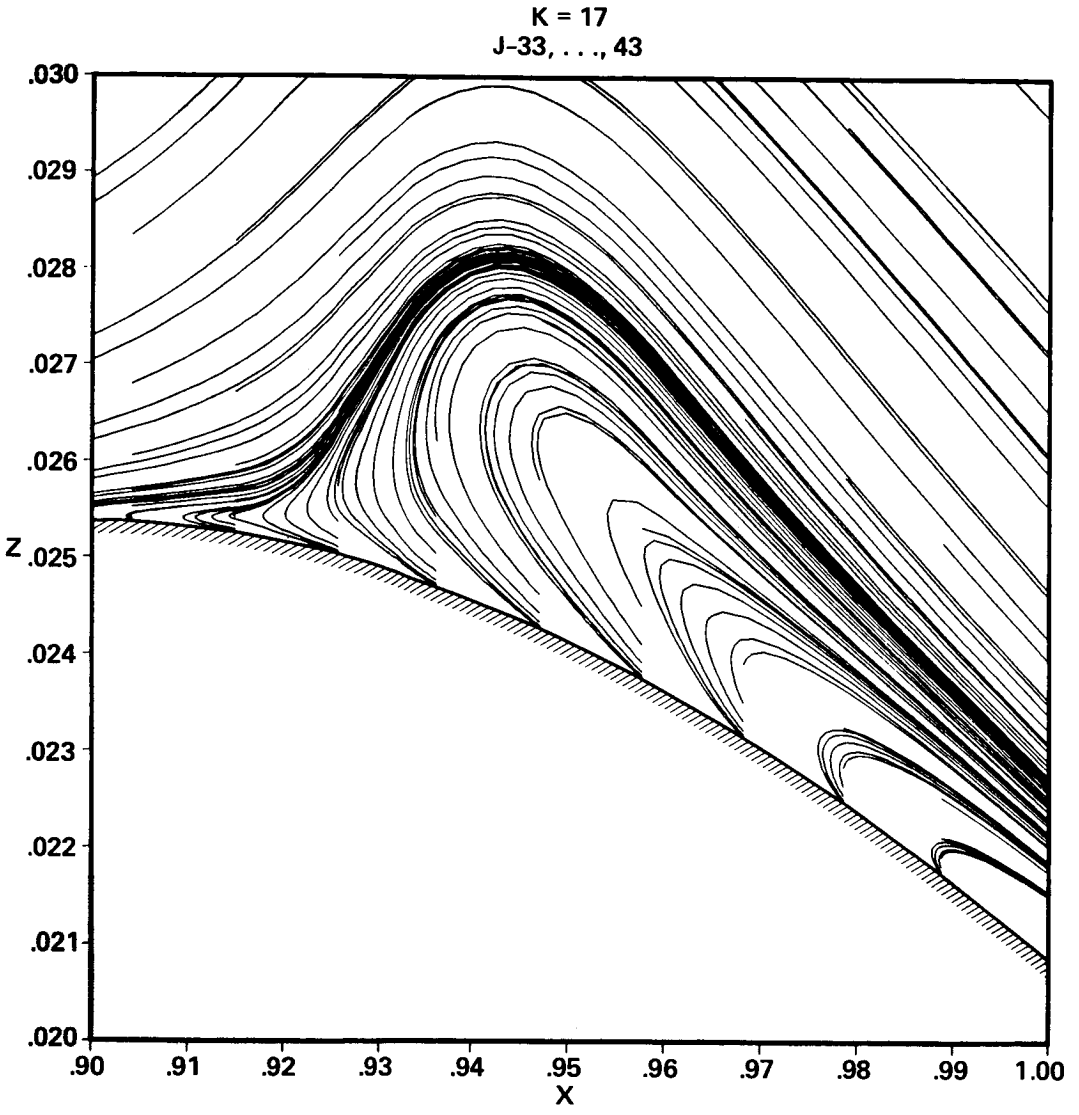

Fig. 54. Expanded view of Fig. 53 near the separation point (z-axis has been expanded 10 times more than the x-axis for better definition of the separation region).

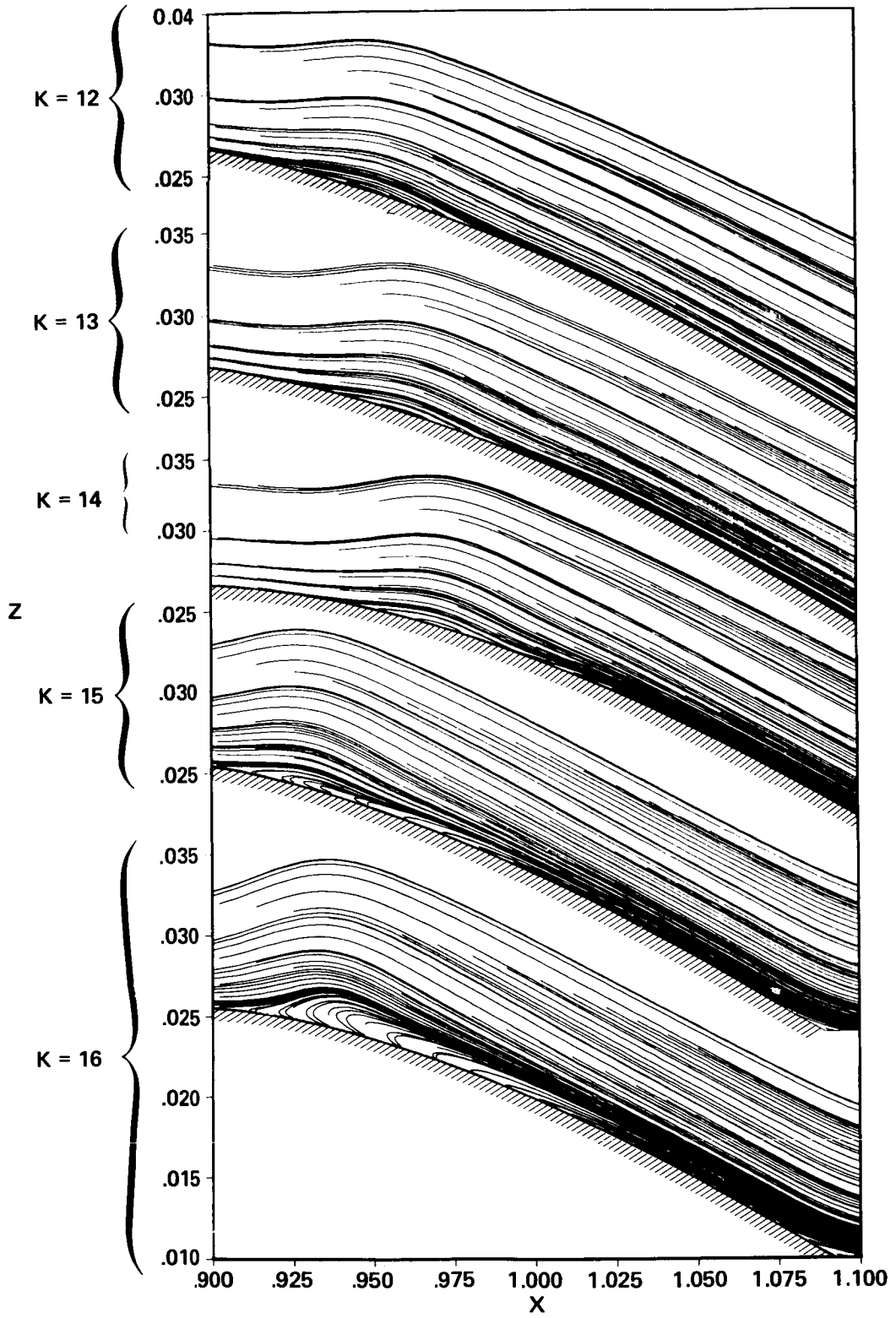

Fig. 55. Sectional streamlines on various JL (cross-sectional) computational planes obtained by "releasing" particles at different levels from stations through the separation zone ($M_\infty = 0.88$). (Note magnification.)

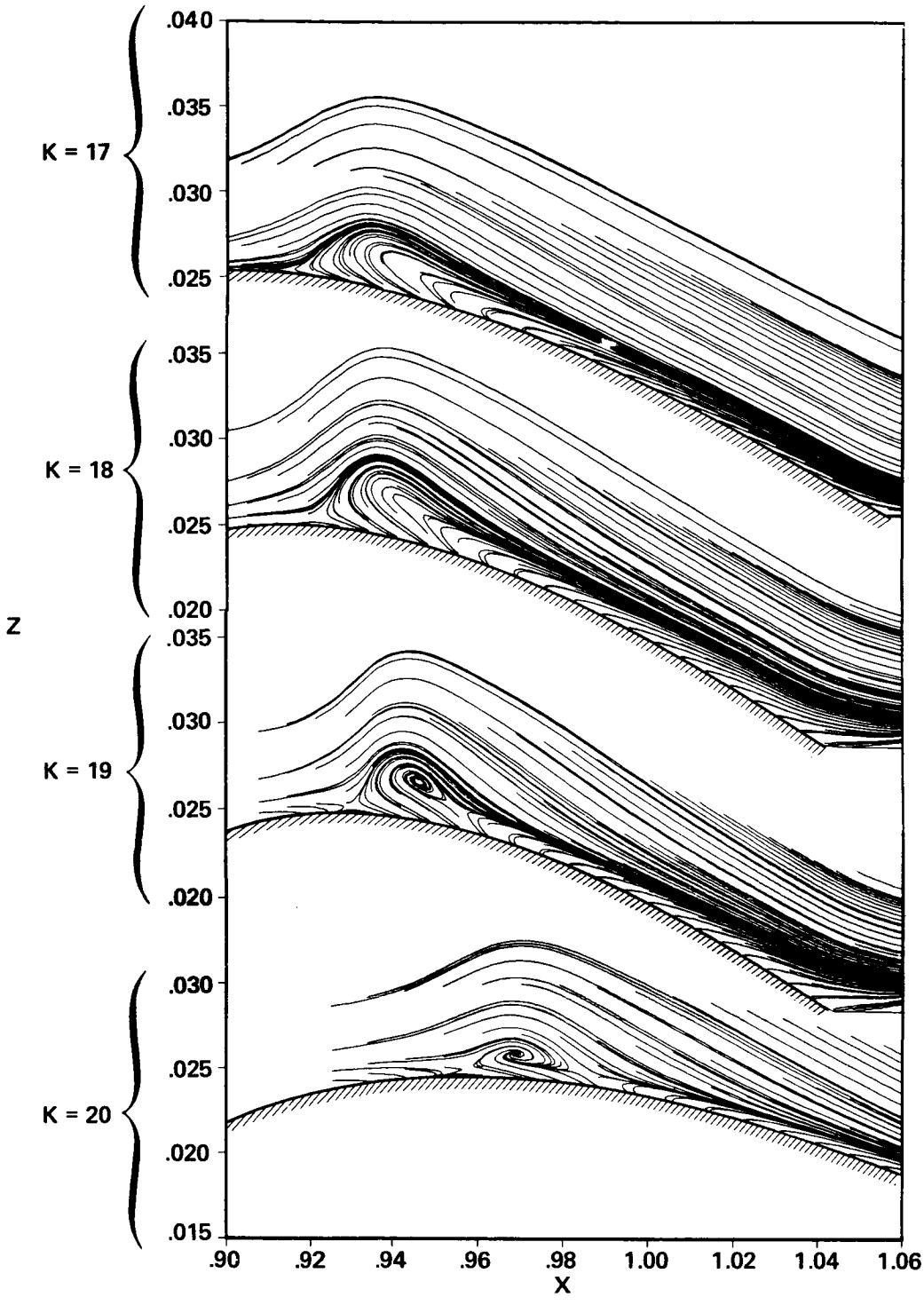

Fig. 55. concluded.

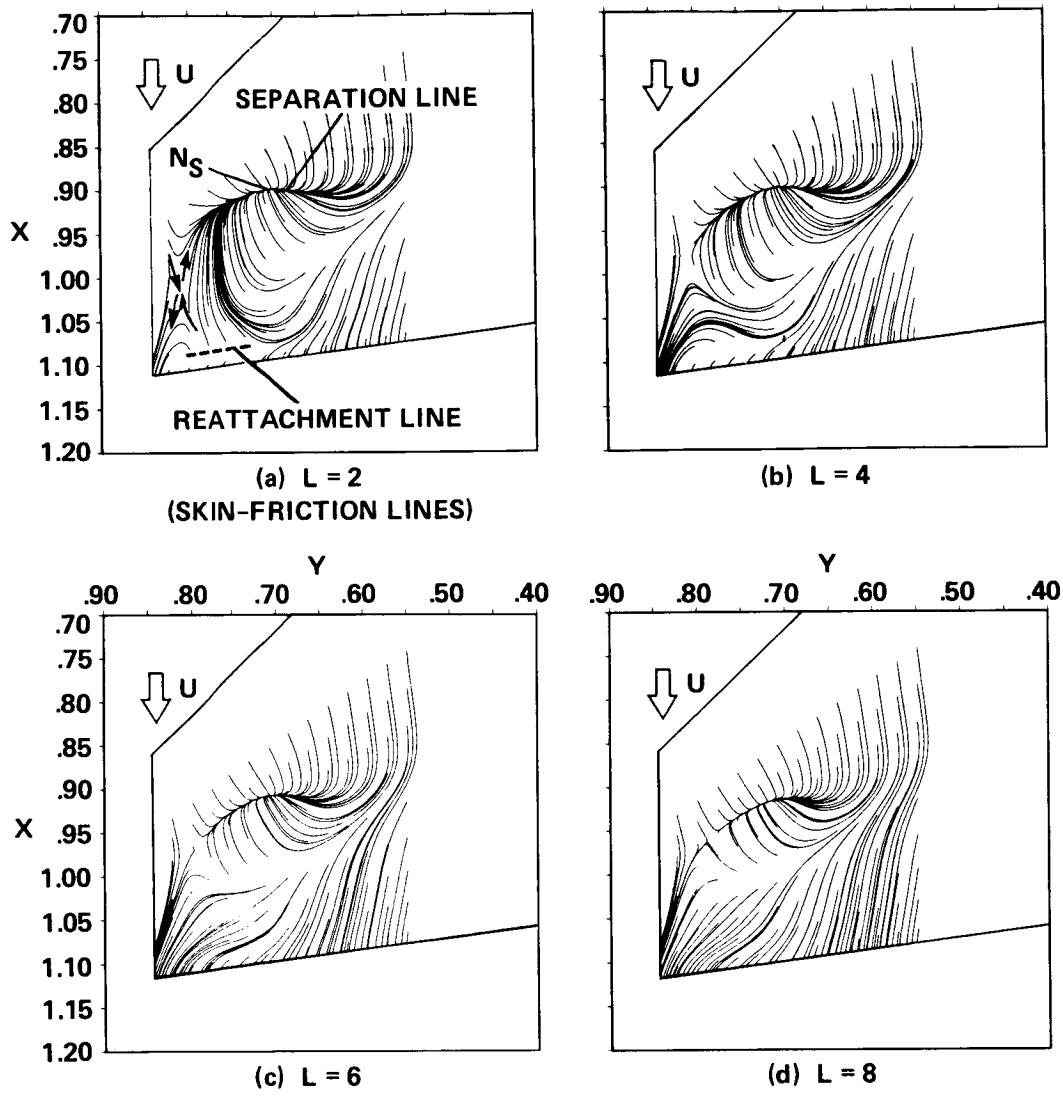

Fig. 56. Sectional streamlines on JK (body-parallel) computational planes. The particles are "released" from a line parallel to the leading-edge ($M_\infty = 0.88$).

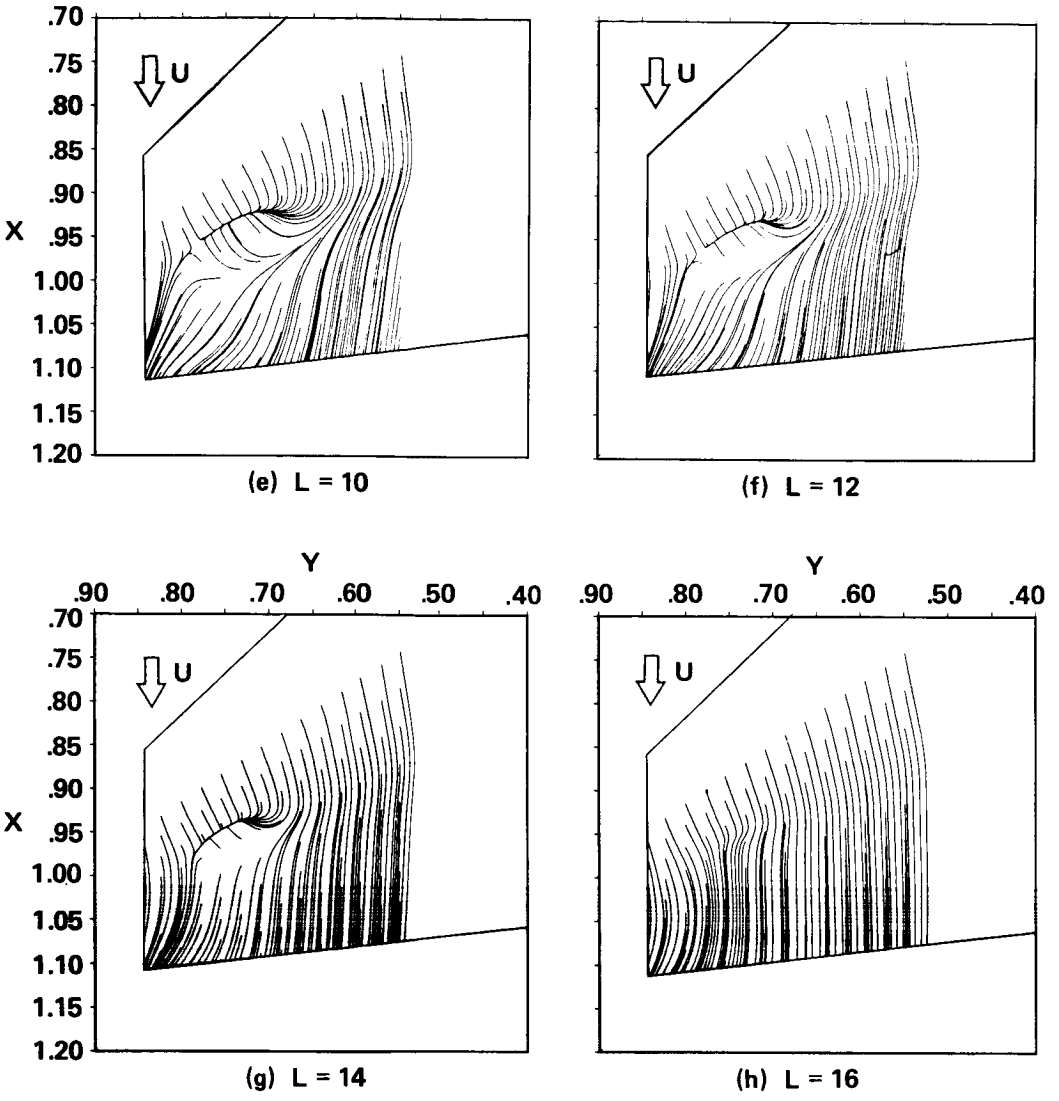

Fig. 56. concluded.

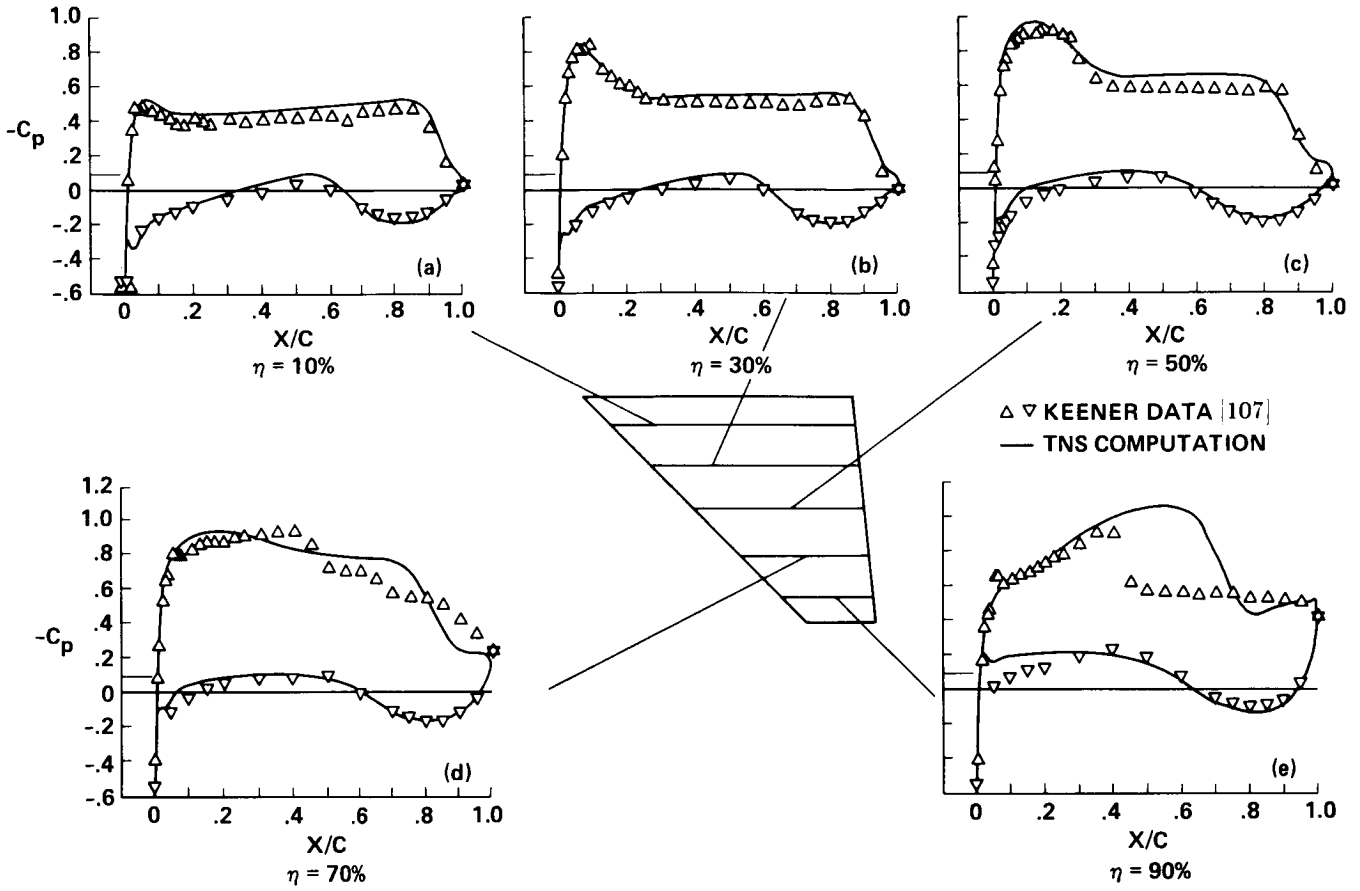

Fig. 57. Comparison of experimental and computed pressure coefficients for WING C: $M_\infty = 0.95$, $\alpha = 5°$, $Re_{m.a.c.} = 6.8 \times 10^6$.

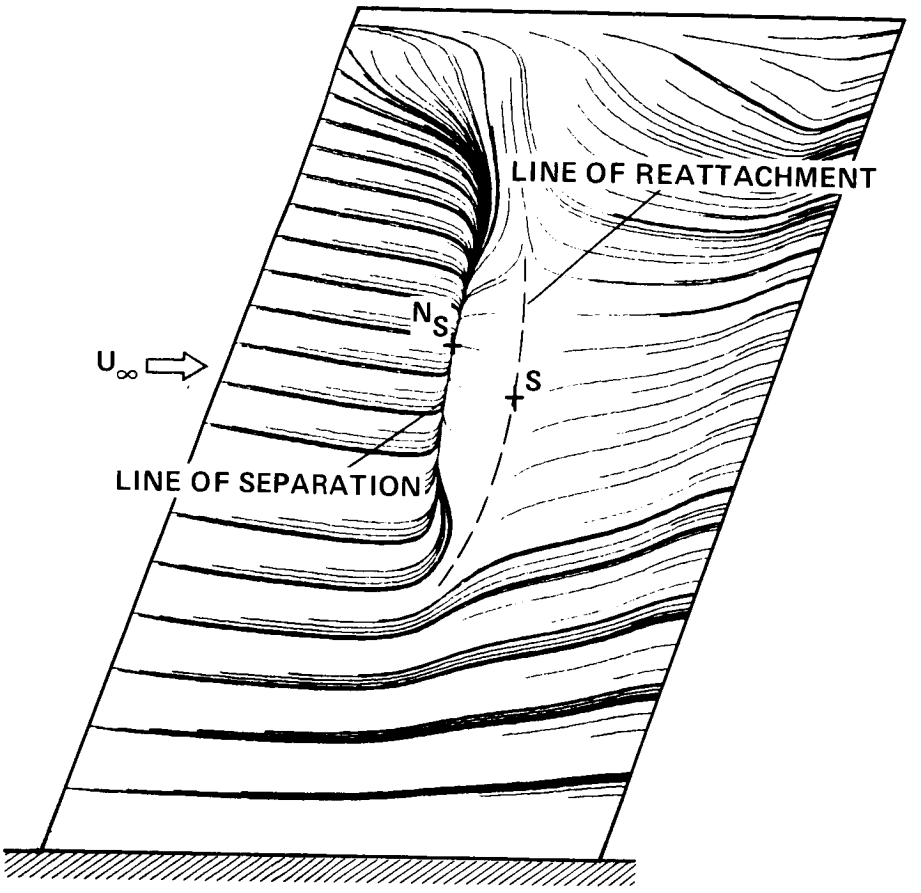

Fig. 58. Computed skin-friction lines for the flow over the NACA 0012 wing; $M_\infty = 0.80$, $\alpha = 5°$, $Re_c = 8 \times 10^6$.

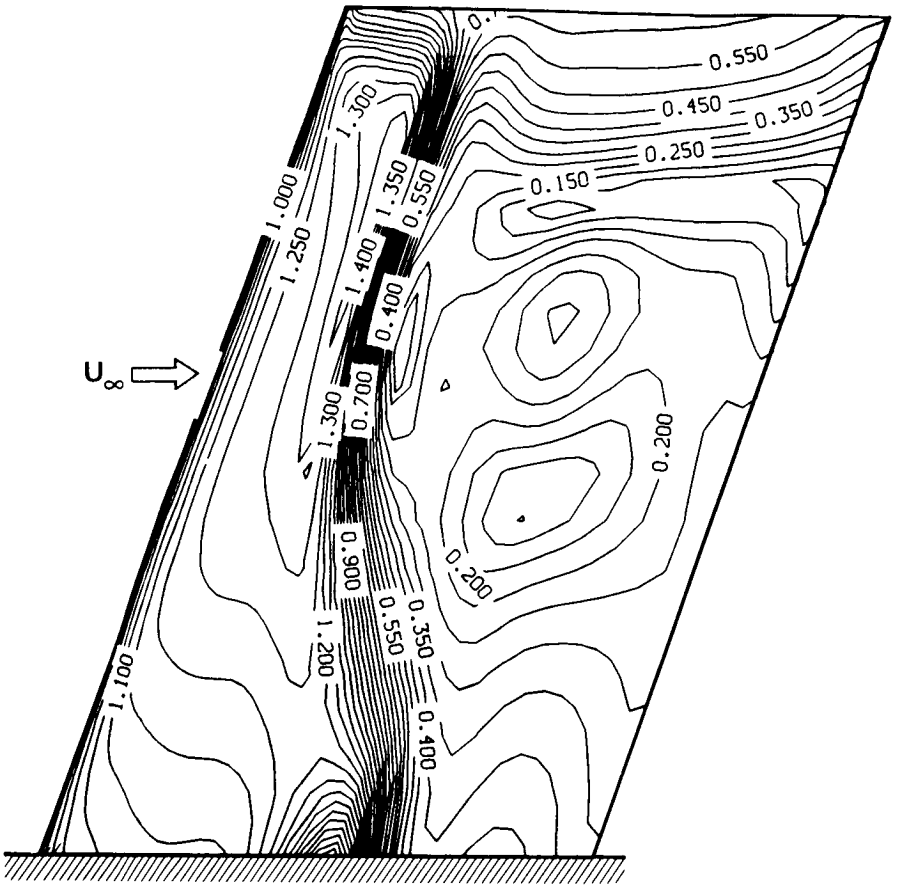

Fig. 59. Mach number contours on the upper surface of NACA 0012 wing; $M_\infty = 0.85$, $\alpha = 5^\circ$, $Re_c = 8 \times 10^6$.

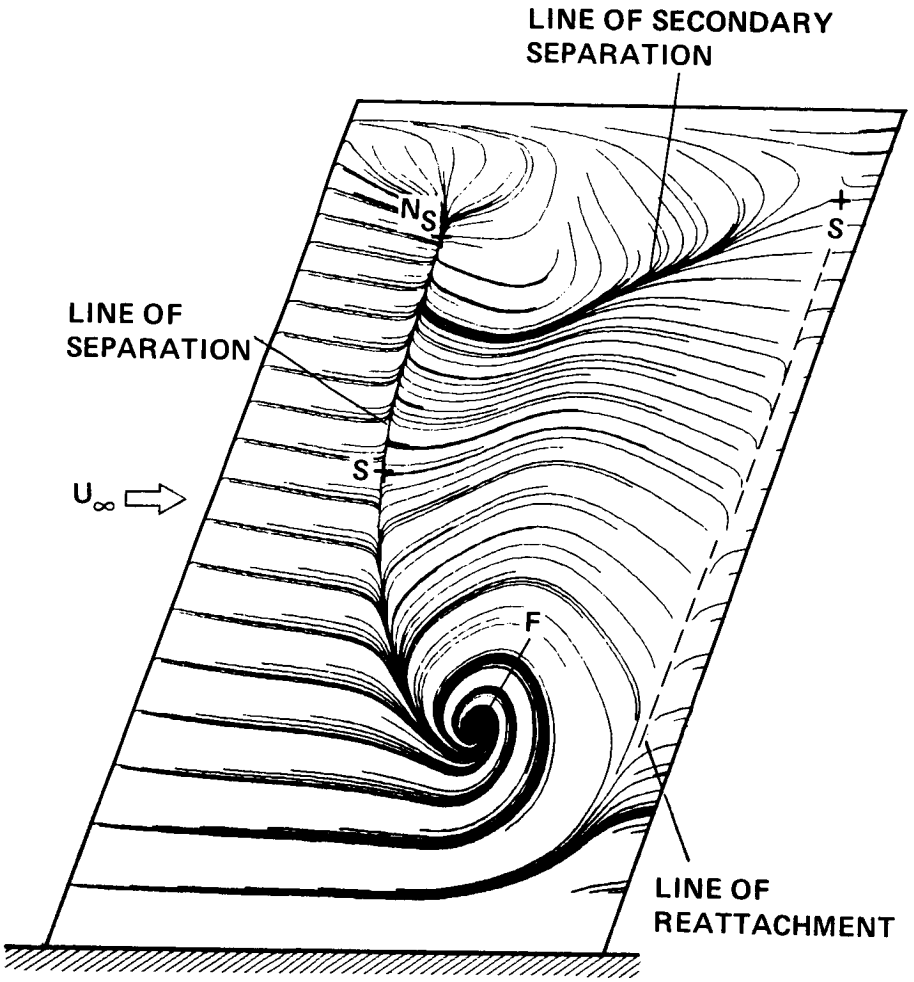

Fig. 60. Computed skin-friction lines for the flow over the NACA 0012 wing; $M_\infty = 0.85$, $\alpha = 5°$, $Re_c = 8 \times 10^6$.

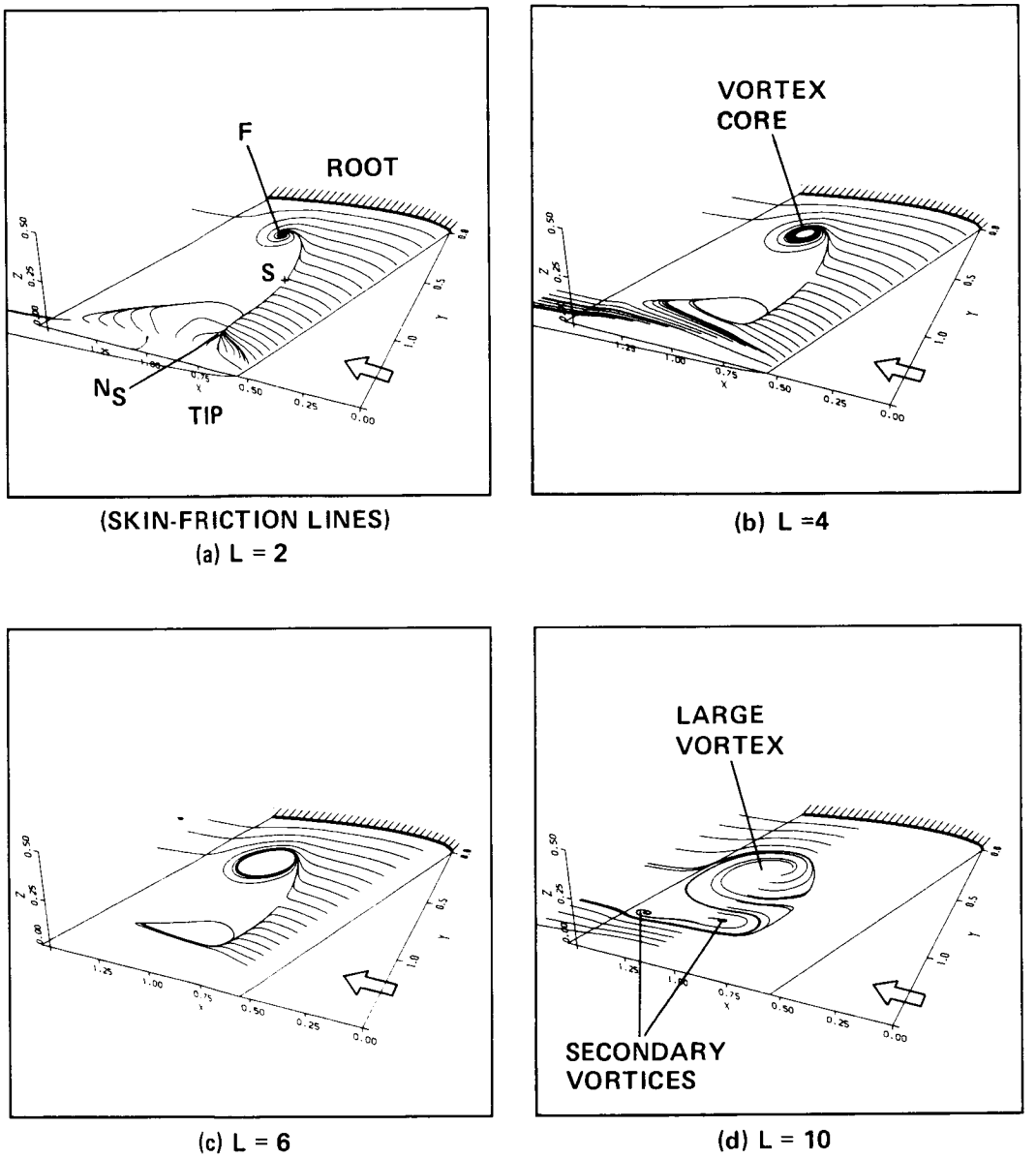

(SKIN-FRICTION LINES)
(a) L = 2

(b) L =4

(c) L = 6

(d) L = 10

Fig. 61. Sectional streamlines on JK (body-parallel) computational planes. Particles are "released" from a line parallel to the leading-edge ($M_\infty = 0.85$).

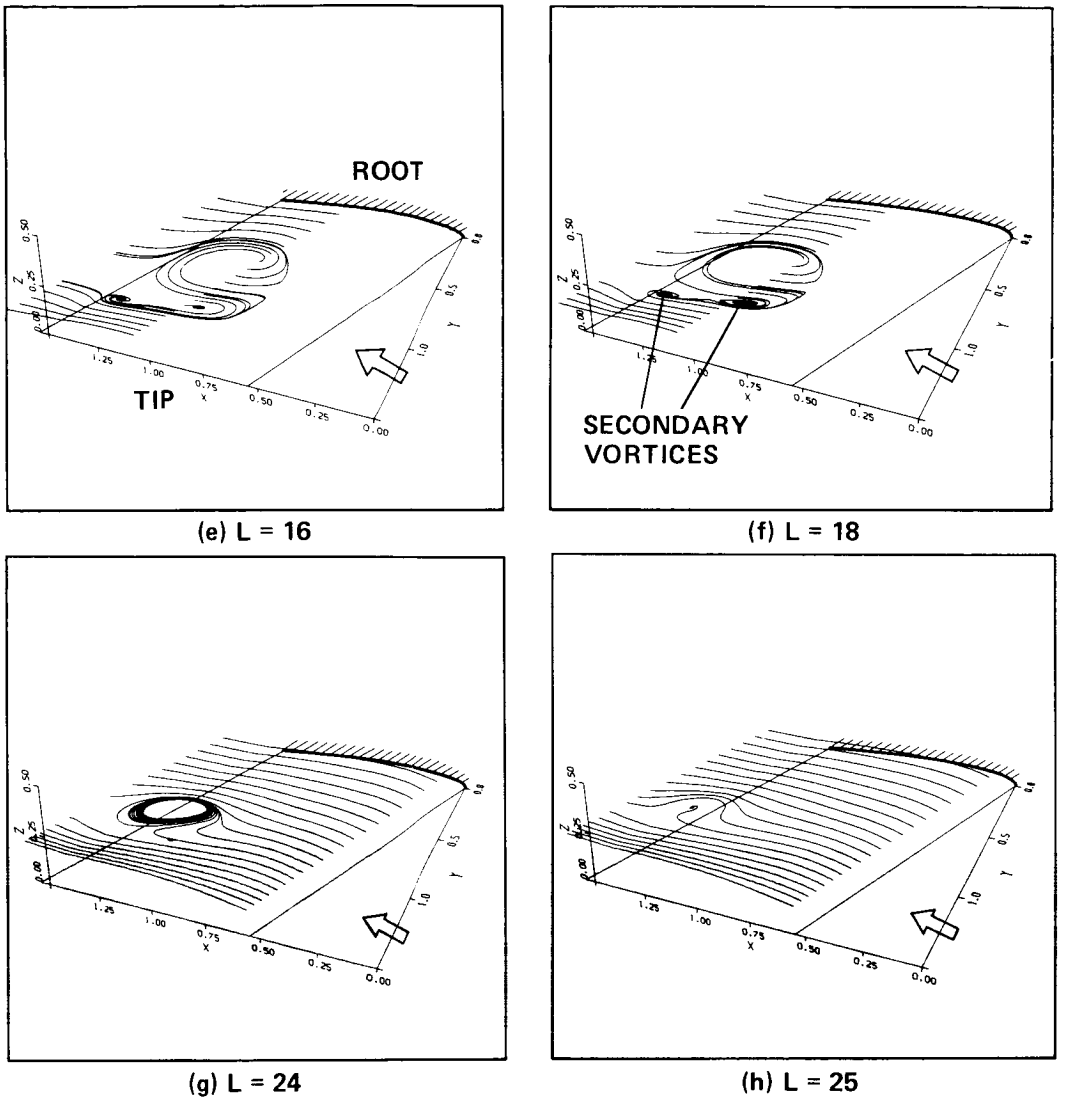

(e) L = 16 (f) L = 18

(g) L = 24 (h) L = 25

Fig. 61. concluded.

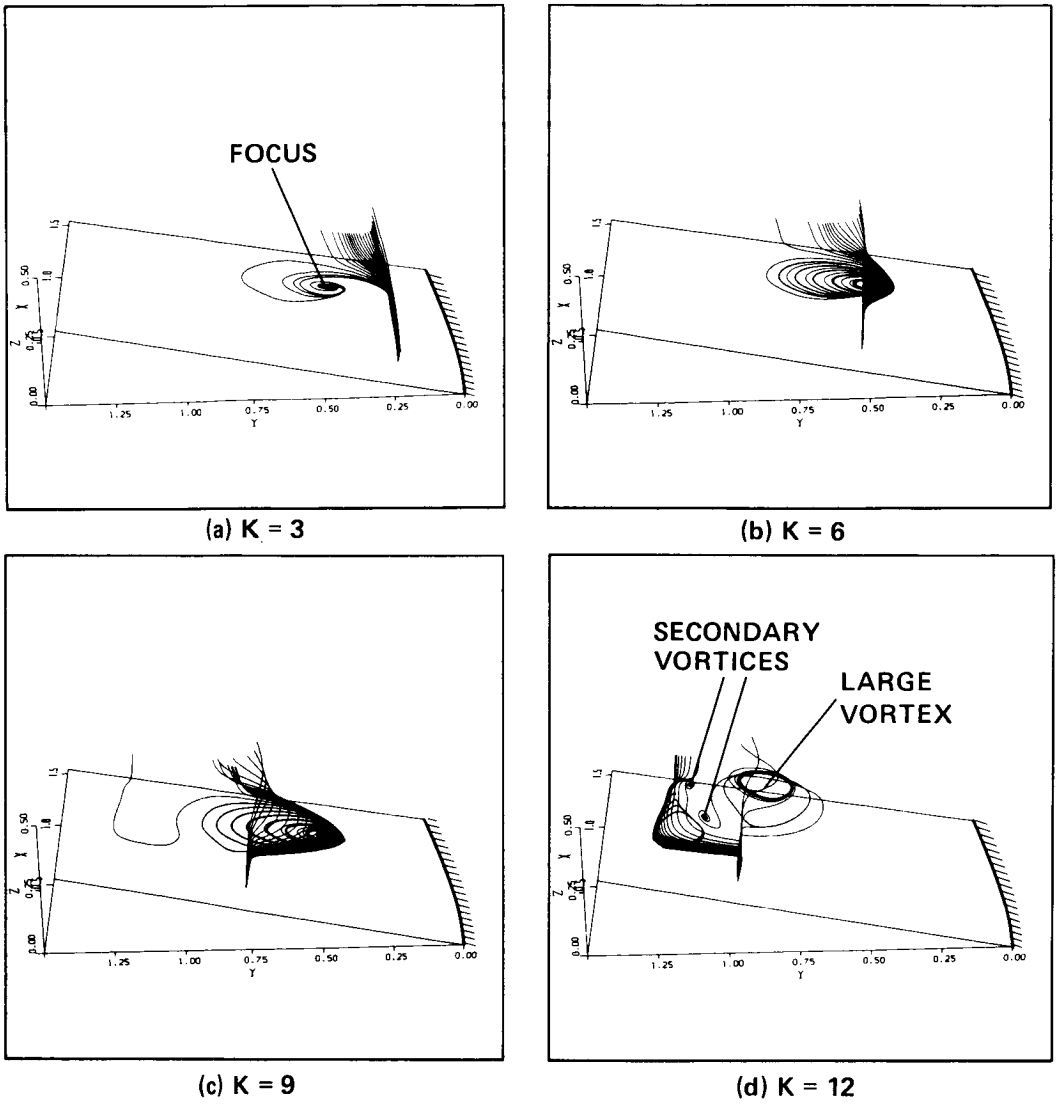

Fig. 62. Sectional streamlines on JK (body-parallel) computational planes obtained by "releasing" particles at different L levels for a fixed value of J ($M_\infty = 0.85$).

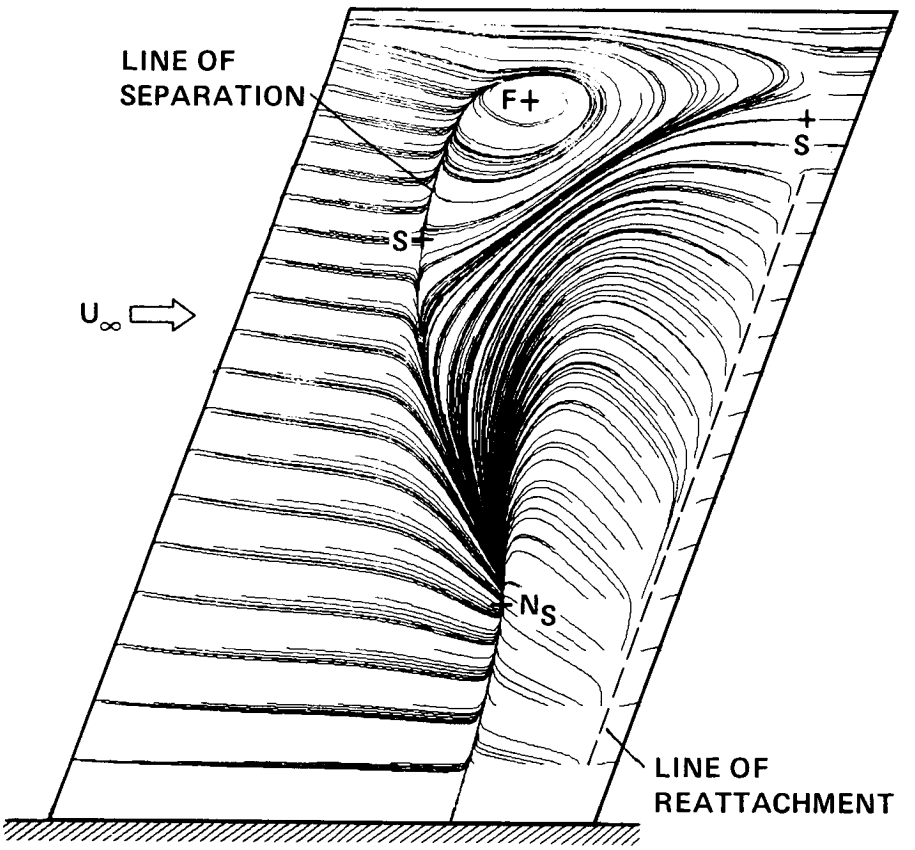

Fig. 63. Computed skin-friction lines for the flow over the NACA 0012 wing; $M_\infty = 0.90$, $\alpha = 5°$, $Re_c = 8 \times 10^6$.

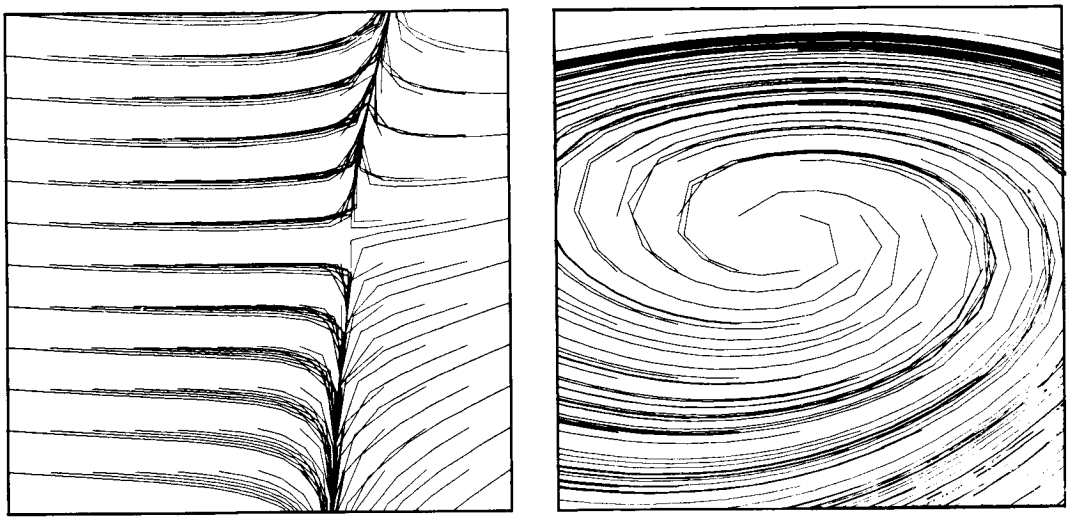

(a) SADDLE POINT (OF SEPARATION)

(b) FOCUS

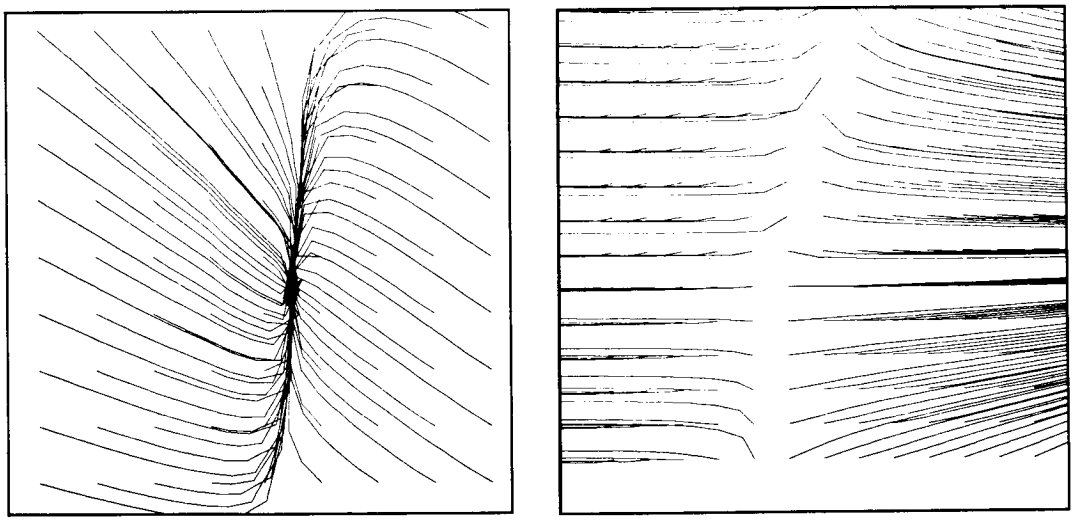

(c) NODAL POINT (OF SEPARATION)

(d) SADDLE POINT (OF REATTACHMENT)

Fig. 64. Expanded views of the critical points of Fig. 63.

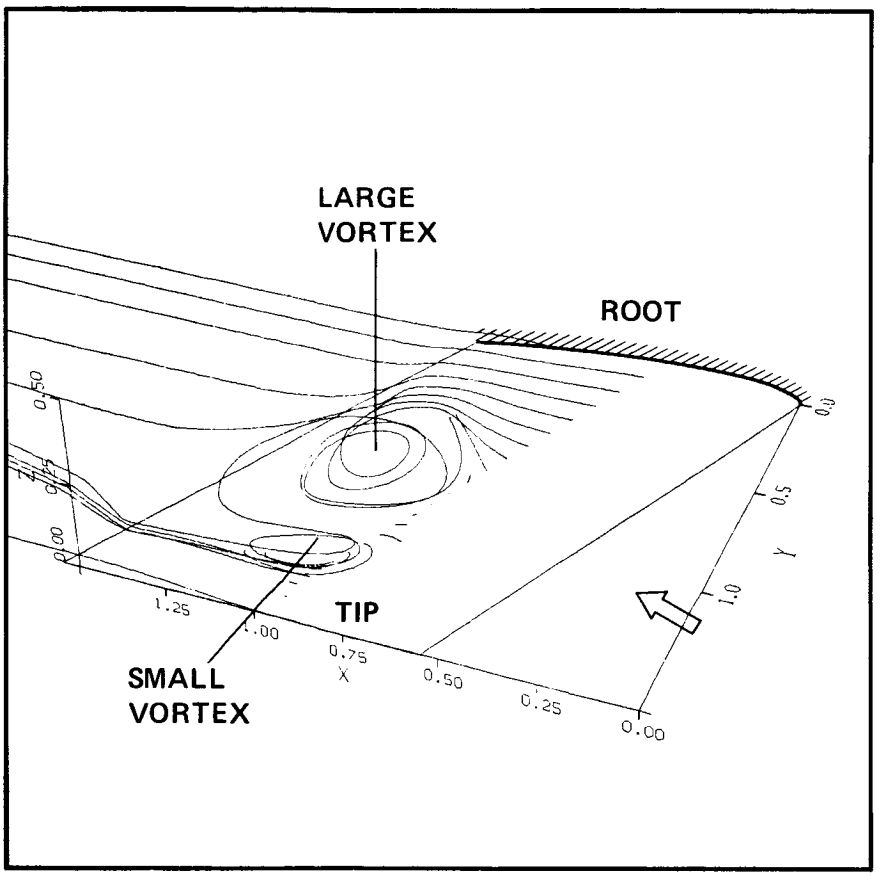

Fig. 65. Three-dimensional streamlines of the flow over the NACA 0012 wing; $M_\infty = 0.90$, $\alpha = 5°$, $Re_c = 8 \times 10^6$.

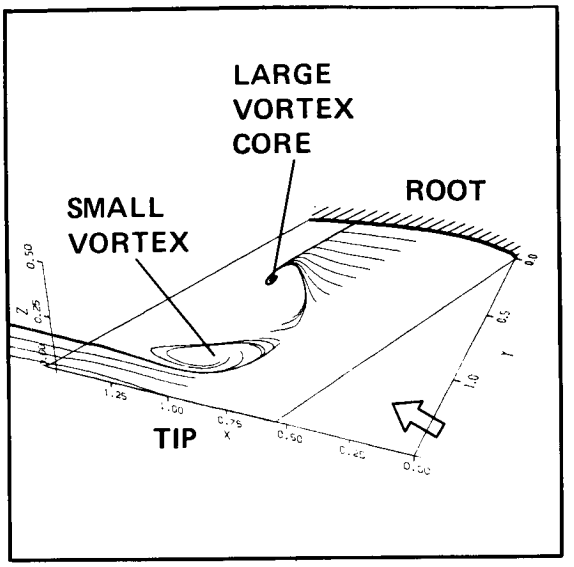

(a) L = 12

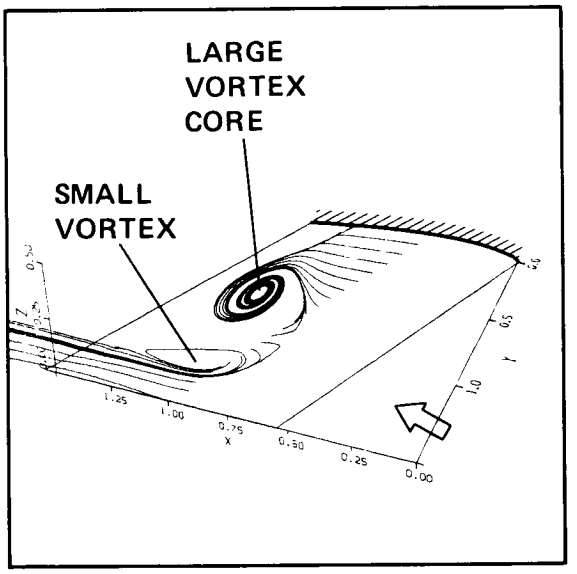

(b) L = 14

Fig. 66. Sectional streamlines on JK (body-parallel) computational planes. Particles are "released" from a line parallel to the leading-edge at 40% chord ($M_\infty = 0.85$).

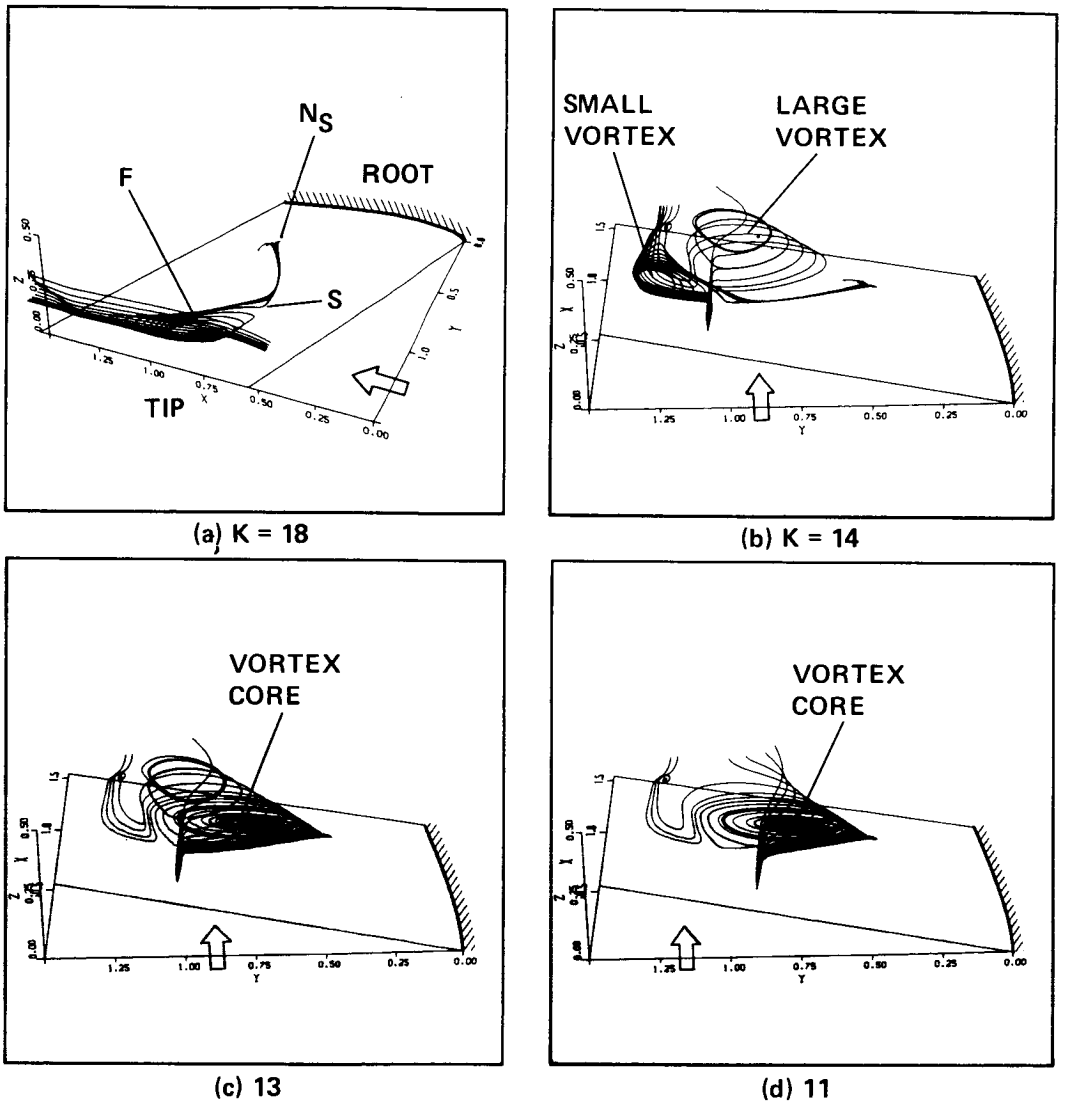

Fig. 67. Sectional streamlines on JK (body-parallel) computational planes obtained by "releasing" particles at different L levels for a fixed value of J ($M_\infty = 0.90$).

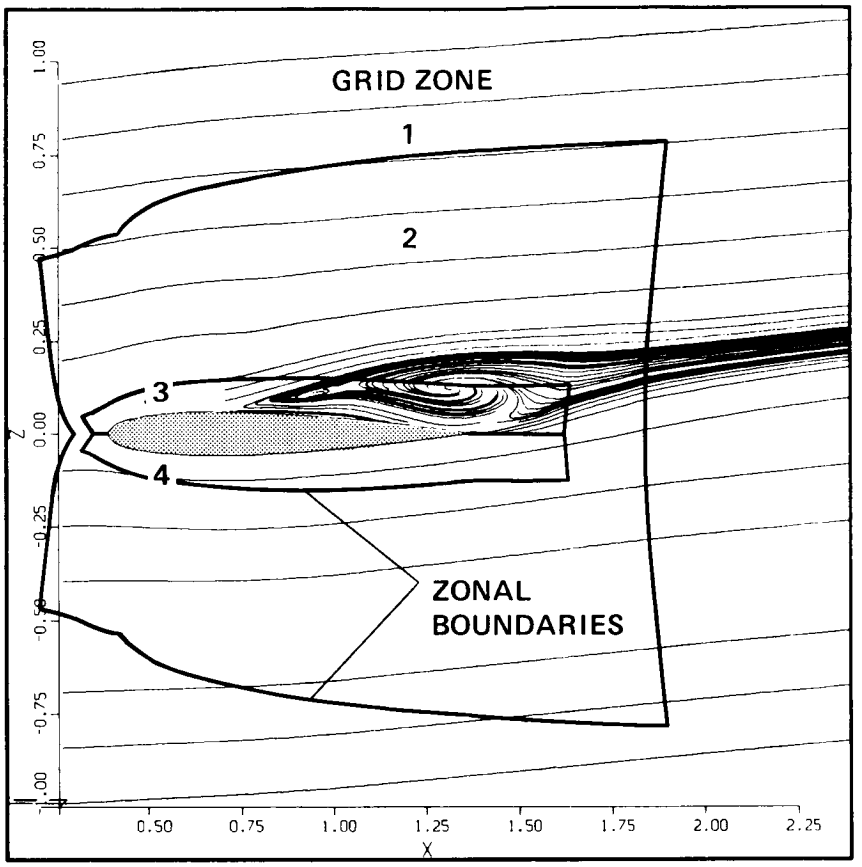

Fig. 68. Sectional streamlines in JL (body-normal) plane at $2y/b = 0.66$.

CHAPTER 5

CONCLUSION

5.1 Summary

The significant achievements in this work are associated with both numerical methods and fluid mechanics. A fast, efficient, and reliable computer program (TNS) was developed, and using this program, numerical solutions of the Euler/Navier-Stokes equations for the transonic flow about wing geometries were obtained. For the first time, computations produced good agreement with experiment for low-aspect-ratio, separated wing flows in the transonic regime. Under experimental guidance, new numerical techniques were developed to improve the computations. Contributions to the understanding of separated flows were made through the extensive use of computer graphics. Familiar as well as new fluid flow phenomena, which should be of interest to experimental and theoretical fluid mechanics, was displayed.

The TNS computer code represents the first three-dimensional Euler/Navier-Stokes zonal algorithm. Using this program, fine grid-resolution flow fields about wing geometries have been achieved. It is a generic program which includes wind-tunnel wall or free air simulation capability, and is suitable, with specific extensions, for computing wing-fuselage or wing-fuselage-tail configurations. The TNS program is more than one order of magnitude faster than comparable Navier-Stokes solvers for wing geometries reported in the literature. It was shown that, instead of using the original block-ADI algorithm, by using a diagonal-ADI algorithm with certain enhancements, a speed-up of 40 was possible.

Also, an efficient data management scheme using SSD (solid state device) resulted in an I/O time of about 1-2% of the CPU time for a typical run. On the other hand, if standard rotating disk had been used, an I/O time of about 1000% of the CPU time would have resulted!

Using the TNS program, good correlation between experiment and computation was achieved for complex flow calculations associated with shock-induced separated flows. First, the effects of different artificial dissipation models incorporated into the block and diagonal algorithms associated with the TNS code were assessed for attached and separated flows. It was found that these algorithms computed correct pressure distributions, but surprisingly predicted different skin-friction fields. Accurate computation of pressure is not the ultimate goal of a Navier-Stokes solver; even a good potential flow solver can give a reasonable answer if the flow conditions are not extreme. A Navier-Stokes code should resolve the boundary layer and reasonably compute the viscous and heat transfer effects.

In this dissertation, a simple scheme modifying the artificial dissipation model associated with the diagonal-ADI algorithm in the TNS code was proposed and successfully implemented for both attached and separated flow cases. As a result of this, for example, C_f was increased roughly 50% for an attached flow case, and showed excellent agreement with the result of another "proven" viscous-inviscid interaction program. Also, using this scheme, improvements have been observed on the skin-friction maps of shock-induced separated flows as compared to oil-flow photographs.

Another aspect of this work has been to prove that a simple idea, such as the relaxation turbulence model, can improve numerical computations. In this respect, certain limitations of the algebraic turbulence model due to Baldwin and Lomax associated with the TNS code were eliminated. As a result, the quite challenging task of obtaining pressure plateaus associated with boundary layer separation was achieved. Also, and perhaps more importantly, the distribution of critical points associated with the skin-friction map of one transonic separated case (NACA 0012 wing, $M_\infty = 0.826$, $\alpha = 2°$) was changed from an incorrect topology into the correct topology as supported by the experimental oil-flow picture.

However, the most important outcome of this work was the beginning of the fulfillment of a long-awaited expectation of seeing agreement between experimental oil-flow pictures and computations for separated flows. This desire was expressed by George Schairer, a retired senior Boeing company engineer, to the first author's research advisor Brian Cantwell in a private communication. In this work, one very good correlation between the computed skin-friction field and experimental oil-flow for a highly swept, tapered, and cambered wing, i.e. the WING C, was obtained for the first time (in the case of $M_\infty = 0.85$, $\alpha = 5°$). Also, two other computed cases (WING C, $M_\infty = 0.88$, $\alpha = 5°$ and NACA 0012, $M_\infty = 0.826$, $\alpha = 2°$) show relatively good correlation. All computed cases are in good agreement with experiment in terms of the pressure distributions.

Investigation of the TNS code's ability to compute massively separated flow cases in the transonic regime for the NACA 0012 wing resulted in some quite fascinating phenomena. The skin-friction maps of these cases produced very well-formed critical points, particulary two surface vortices; one spiraling inward, another spiraling outward! This is the first time computations of this type have been produced. It was learned (by private communication, Tobak and Fairlie, 1985) that the presence of an outward spiraling vortex has been presumed to be less likely by quite a few experimentalists in their work. Also, it is believed that the illustrations of three-dimensional flow fields above the NACA 0012 wing and WING C via computed "streamlines" and "sectional-streamlines" put some light on the nature of three-dimensional vortical flows emanating from separated

turbulent boundary layers. This is an area where the experiments are limited to only surface oil-flow techniques, or again limited dye or smoke flow techniques. It is hoped that a theoretical or experimental fluid mechanics researcher may further benefit from the computed results.

5.2 Recommendations for Future Work

Throughout this work, the lack of sufficient grid resolution has been the single most important limiting item. Without enough grid resolution, it is not possible to give a definitive answer to the question of discrepancy between an experiment and computation. Therefore, the first recommendation is to rerun these cases with higher grid resolution when a faster computer with more memory is available. Another way of refining the grid without waiting for a new computer is to place additional zones in critical regions of the flow; for example, the tip. An H-C or O-C grid topology at the tip would be ideal for this task. However, this necessitates a more sophisticated interpolation program to handle the new situation.

As might be remembered, another important shortcoming was the poor resolution of the viscous wake. The viscous grid zones do not extend downstream far enough to resolve the far wake. Since the coarse Euler grid cannot support the high gradients associated with a wake structure, this causes certain inaccuracies, and can become a very significant factor especially at high angles of attack involving future applications with multiple lifting surfaces. However, it is expected that placing another zone in the wake will solve the problem.

The importance of artificial dissipation was previously emphasized, and a simple correction was suggested which worked quite nicely. However, a better scheme is highly desirable. Probably, the present scheme which uses the sum of the spectral radii of the flux jacobians as a coefficient is not good, because it varies like $O(1/\triangle\varsigma)$ with distance ς through the boundary layer. This scheme was originally designed for the Euler equations where it works well. An improved scheme which is especially designed for Navier-Stokes computations would be appropriate.

Turbulence modeling is, of course, extremely important for high Reynolds number flows and for separated flows. It is known that, with the exception of few cases, the Baldwin-Lomax or Cebeci-Smith algebraic eddy viscosity models cannot properly handle two- or three-dimensional separated flows. Work needs to be done in this area implementing existing or developing new turbulence models. This should be done with sufficiently refined grids so as to eliminate coarse grid effects from affecting the results.

One subject which deserves special attention is wind-tunnel wall simulation. It would be appropriate to model porous wind-tunnel walls and assess their effects. Before this can be successful, detailed measurements at the walls are required. There is plenty of room for improvement with solid wind-tunnel walls as well. As is known quite well from two-dimensional computational work, prescribing wind-tunnel exit pressure as well as upper and lower wall pressures as boundary conditions is extremely important. It is believed that providing these capabilities to the TNS code should improve wind tunnel wall simulations. It should especially lessen the discrepancy between the experimental measurement and computation of the shock strength and location.

All of the separated flow computations in this dissertation belong to shock-induced separations at high Reynolds and Mach numbers. However, it would be interesting to investigate flows for the subcritical or even low subsonic regimes at high angles of attack. Such a study would help in understanding separation due to adverse pressure gradients. The aircraft industry would benefit greatly from this, because such a calculation simulates stall behavior of a wing during take-off or landing.

Appendix A

FLUX JACOBIAN AND VISCOUS COEFFICIENT MATRICES

The flux jacobians $\hat{A}, \hat{B}$, and $\hat{C}$ are given by

$$\begin{bmatrix} K_0 & K_1 & K_2 \\ K_1\phi^2 - u\theta & K_0 + \theta - K_1(\gamma-2)u & K_2u - (\gamma-1)K_1v \\ K_2\phi^2 - v\theta & K_1v - K_2(\gamma-1)u & K_0 + \theta - K_2(\gamma-2)v \\ K_3\phi^2 - w\theta & K_1w - K_3(\gamma-1)u & K_2w - K_3(\gamma-1)v \\ \theta[2\phi^2 - \gamma(e/\rho)] & \{K_1[\gamma(e/\rho) - \phi^2] & \{K_2[\gamma(e/\rho) - \phi^2] \\ & -(\gamma-1)u\theta\} & -(\gamma-1)v\theta\} \end{bmatrix}$$

$$\begin{bmatrix} K_3 & 0 \\ K_3u - (\gamma-1)K_1w & K_1(\gamma-1) \\ K_3v - (\gamma-1)K_2w & K_2(\gamma-1) \\ K_0 + \theta - K_3(\gamma-2)w & K_3(\gamma-1) \\ \{K_3[\gamma(e/\rho) - \phi^2] & K_0 + \gamma\theta \\ -(\gamma-1)w\theta\} & \end{bmatrix} \tag{A.1}$$

where

$$\phi^2 = 0.5(\gamma-1)(u^2 + v^2 + w^2)$$

$$\theta = K_1u + K_2v + K_3w$$

and, for example to obtain $\hat{A}$,

$$K_0 = \xi_t, \quad K_1 = \xi_x, \quad K_2 = \xi_y, \quad K_3 = \xi_z$$

also, the viscous coefficient matrix is given by

$$\hat{M}^n = \begin{bmatrix} 0 & 0 & 0 & 0 & 0 \\ m_{21} & \alpha_1\delta_\varsigma(\rho^{-1}) & \alpha_2\delta_\varsigma(\rho^{-1}) & \alpha_3\delta_\varsigma(\rho^{-1}) & 0 \\ m_{31} & \alpha_2\delta_\varsigma(\rho^{-1}) & \alpha_4\delta_\varsigma(\rho^{-1}) & \alpha_5\delta_\varsigma(\rho^{-1}) & 0 \\ m_{41} & \alpha_3\delta_\varsigma(\rho^{-1}) & \alpha_5\delta_\varsigma(\rho^{-1}) & \alpha_6\delta_\varsigma(\rho^{-1}) & 0 \\ m_{51} & m_{52} & m_{53} & m_{54} & \alpha_0\delta_\varsigma(\rho^{-1}) \end{bmatrix} \tag{A.2}$$

with

$$
\begin{aligned}
m_{21} &= \alpha_1\delta_\varsigma(-u/\rho) + \alpha_2\delta_\varsigma(-v/\rho) + \alpha_3\delta_\varsigma(-w/\rho) \\
m_{31} &= \alpha_2\delta_\varsigma(-u/\rho) + \alpha_4\delta_\varsigma(-v/\rho) + \alpha_5\delta_\varsigma(-w/\rho) \\
m_{41} &= \alpha_3\delta_\varsigma(-u/\rho) + \alpha_5\delta_\varsigma(-v/\rho) + \alpha_6\delta_\varsigma(-w/\rho) \\
m_{51} &= \alpha_1\delta_\varsigma(-u^2/\rho) + \alpha_2\delta_\varsigma(-2uv/\rho) + \alpha_3\delta_\varsigma(-2uw/\rho) \\
&\quad + \alpha_4\delta_\varsigma(-v^2/\rho) + \alpha_6\delta_\varsigma(-w^2/\rho) + \alpha_5\delta_\varsigma(-2vw/\rho) \\
&\quad + \alpha_0\delta_\varsigma(-e/\rho^2) + \alpha_0\delta_\varsigma[(u^2+v^2+w^2)/\rho] \\
m_{52} &= -m_{21} - \alpha_0\delta_\varsigma(u/\rho), \quad m_{53} = -m_{31} - \alpha_0\delta_\varsigma(v/\rho) \\
m_{54} &= -m_{41} - \alpha_0\delta_\varsigma(w/\rho) \\
\alpha_0 &= \gamma\kappa Pr^{-1}(\varsigma_x^2+\varsigma_y^2+\varsigma_z^2), \alpha_1 = \mu[(4/3)\varsigma_x^2+\varsigma_y^2+\varsigma_z^2] \\
\alpha_2 &= (\mu/3)\varsigma_x\varsigma_y, \qquad \alpha_3 = (\mu/3)\varsigma_x\varsigma_z \\
\alpha_4 &= \mu[\varsigma_x^2+(4/3)\varsigma_y^2+\varsigma_z^2], \quad \alpha_5 = (\mu/3)\varsigma_y\varsigma_z \\
\alpha_6 &= \mu[\varsigma_x^2+\varsigma_y^2+(4/3)\varsigma_z^2]
\end{aligned}
\tag{A.3}
$$

Appendix B

SIMILARITY TRANSFORMATION MATRICES

The similarity transformation matrix for the Jacobian matrices $\hat{A}$, $\hat{B}$, and $\hat{C}$ is

$$T_k = \begin{bmatrix} \tilde{k}_x & \tilde{k}_y & \tilde{k}_z \\ \tilde{k}_x u & \tilde{k}_y u - \tilde{k}_z \rho & \tilde{k}_z u + \tilde{k}_y \rho \\ \tilde{k}_x v + \tilde{k}_z \rho & \tilde{k}_y v & \tilde{k}_z v - \tilde{k}_x \rho \\ \tilde{k}_x w - \tilde{k}_y \rho & \tilde{k}_y w + \tilde{k}_x \rho & \tilde{k}_z w \\ [\tilde{k}_x \phi^2/(\gamma-1) & [\tilde{k}_y \phi^2/(\gamma-1) & [\tilde{k}_z \phi^2/(\gamma-1) \\ +\rho(\tilde{k}_z v - \tilde{k}_y w)] & +\rho(\tilde{k}_x w - \tilde{k}_z u)] & +\rho(\tilde{k}_y u - \tilde{k}_x v)] \end{bmatrix}$$

$$\begin{bmatrix} \alpha & \alpha \\ \alpha(u + \tilde{k}_x c) & \alpha(u - \tilde{k}_x c) \\ \alpha(v + \tilde{k}_y c) & \alpha(v - \tilde{k}_y c) \\ \alpha(w + \tilde{k}_z c) & \alpha(w - \tilde{k}_z c) \\ \alpha[(\phi^2 + c^2)/(\gamma-1) + c\tilde{\theta}] & \alpha[(\phi^2 + c^2)/(\gamma-1) - c\tilde{\theta}] \end{bmatrix}, \qquad (B.1)$$

where, $k = \xi$, η, and ς for $\hat{A}$, $\hat{B}$, and $\hat{C}$ respectively. Also, the inverse transformation matrix is given by

$$T_k^{-1} = \begin{bmatrix} [\tilde{k}_x(1 - \phi^2/c^2) & \tilde{k}_x(\gamma-1)uc^{-2} & [\tilde{k}_z\rho^{-1} \\ -\rho^{-1}(\tilde{k}_z v - \tilde{k}_y w)] & & +\tilde{k}_x(\gamma-1)vc^{-2}] \\ [\tilde{k}_y(1 - \phi^2/c^2) & [-\tilde{k}_z\rho^{-1} & \tilde{k}_y(\gamma-1)vc^{-2} \\ -\rho^{-1}(\tilde{k}_x w - \tilde{k}_z u)] & +\tilde{k}_y(\gamma-1)uc^{-2}] & \\ [\tilde{k}_z(1 - \phi^2/c^2) & [-\tilde{k}_y\rho^{-1} & [\tilde{k}_x\rho^{-1} \\ -\rho^{-1}(\tilde{k}_y u - \tilde{k}_x v)] & +\tilde{k}_z(\gamma-1)uc^{-2}] & +\tilde{k}_z(\gamma-1)vc^{-2}] \\ \beta(\phi^2 - c\tilde{\theta}) & \beta[\tilde{k}_x c - (\gamma-1)u] & \beta[\tilde{k}_y c - (\gamma-1)v] \\ \beta(\phi^2 + c\tilde{\theta}) & -\beta[\tilde{k}_x c + (\gamma+1)u] & -\beta[\tilde{k}_y c + (\gamma-1)v] \end{bmatrix}$$

$$\begin{bmatrix} [-\tilde{k}_y\rho^{-1} + \tilde{k}_x(\gamma-1)wc^{-2}] & -\tilde{k}_x(\gamma-1)c^{-2} \\ [\tilde{k}_x\rho^{-1} + \tilde{k}_y(\gamma-1)wc^{-2}] & -\tilde{k}_y(\gamma-1)c^{-2} \\ \tilde{k}_z(\gamma-1)wc^{-2} & -\tilde{k}_z(\gamma-1)c^{-2} \\ \beta[\tilde{k}_z c - (\gamma-1)w] & \beta(\gamma-1) \\ -\beta[\tilde{k}_z c + (\gamma-1)w] & \beta(\gamma-1) \end{bmatrix}, \qquad (B.2)$$

where, $\tilde{\theta} = \tilde{k}_x u + \tilde{k}_y v + \tilde{k}_z w$ and, for example, $\tilde{k}_x = k_x/(k_x^2 + k_y^2 + k_z^2)^{1/2}$, etc.

Also, $\phi^2 = 0.5(\gamma - 1)(u^2 + v^2 + w^2)$, $\alpha = \rho/\sqrt{2}c$ and $\beta = 1/\sqrt{2}\rho c$.

REFERENCES

[1] Navier, M.,"Memoires sur les lois du mouvement des Fluids," Mem. Acad. Sci., Vol.6, pp. 389-416 (1823)

[2] Stokes, G. G.,"On the Theories of Internal Friction of Fluids in Motion," Trans. Camb. Philos. Soc. Vol.8, pp. 287-305 (1845)

[3] Prandtl, L.,"Über Flüssigkeitsbewegung bei sehr kleiner Reibung," Proc. 3rd Int. Math. Congr., Heidelberg, 1904.

[4] Chapman, D. R."Computational Aerodynamics Development and Outlook," AIAA Journal, Vol.17, pp. 1293-1313, Dec.1979.

[5] Da Costa, A. L.,"Application of Computational Aerodynamic Methods to the Design and Analysis of Transport Aircraft," ICAS Paper, Eleventh Congress of the International Council of the Aeronautical Sciences, Lisbon, Portugal, Sept. 10-16, 1978.

[6] Peyret, R. and Viviand, H.,"Computation of Viscous Compressible Flows Based on the Navier-Stokes Equations," AGARDograph No. 212, 1975.

[7] Mac Cormack, R. W.,"Numerical Solutions of the Interaction of a Shock Wave with a Laminar Boundary Layer," Lecture Notes in Physics, Vol. 8, Springer-Verlag, New York, pp. 151-163, 1971.

[8] Carter, J. E.,"Numerical Solutions of the Navier-Stokes Equations for Supersonic Laminar Flow Over a Two-dimensional Compression Corner," NASA TR R-385, July 1972.

[9] Jain, A. C. and Adimurty, V.,"Hypersonic Merged Stagnation Shock Layers, Part I: Adiabatic Wall Case," AIAA Journal, Vol.12, pp. 342-347, March 1974.

[10] Thompson, J. F., Thames, F. C., Walker, R. L. and Shanks, S. P., "Numerical Solution of the Unsteady Navier-Stokes Equations for Arbitrary Bodies Using Boundary-Fitted Curvilinear Coordinates," Unsteady Aerodynamics, R. B. Kinney, ed., University of Arizona, Tucson, pp. 453-485, 1975.

[11] Hodge, J. K. and Stone, A. L.,"Numerical Solution for Airfoils Near Stall in Optimized Boundary-Fitted Curvilinear Coordinates," AIAA Paper No. 78-284, Jan. 1978.

[12] Tannehill, J. C., Holst, T. L. and Rakich, J. V.,"Numerical Computation of Two-Dimensional Viscous Blunt Body Flows with an Impinging Shock," AIAA Journal, Vol.14, Feb. 1976, pp. 204-211.

[13] Li, C. P.,"A Numerical Study of Laminar Flow Separation on Blunt Flared Cones at Angle of Attack," AIAA Paper No. 74-585, June 1974.

[14] Shang, J. S. and Hankey, W. L.,"Numerical Solution of the Navier-Stokes Equations for a Three-Dimensional Corner," AIAA Journal, Vol.15, pp. 1575-1582, Nov. 1977.

[15] Hung, C. M. and Mac Cormack, R. W.,"Numerical Solution of Supersonic Laminar Flow over a Three-Dimensional Compression Corner," AIAA Paper No. 77-694, June 1977.

[16] Wilcox, D. C.,"Calculation of Turbulent Boundary Layer Shock Wave Interaction," AIAA Journal, Vol.11, pp. 1592-1594, Nov. 1973.

[17] Baldwin, B. S. and Mac Cormack, R. W.,"Numerical Solution of the Interaction of a Strong Shock Wave with a Hypersonic Turbulent Boundary Layer," AIAA Paper No. 74-558, June 1974.

[18] Deiwert, G. S.,"Numerical Simulation of High Reynolds Number Transonic Flow," AIAA Paper No. 74-603, June 1974.

[19] Wilcox, D. C.,"Numerical Study of Separated Turbulent Flows," AIAA Paper No.74-584, June 1974.

[20] Shang, J. S. and Hankey, W. L.,"Numerical Simulation for Supersonic and Hypersonic Turbulent Flow Over a Compression Ramp," AIAA Journal, Vol.13, pp. 1368-1374, Oct. 1975.

[21] Hung, C. M. and Mac Cormack, R. W.,"Numerical Simulation of Supersonic and Hypersonic Turbulent Compression Corner Flows," AIAA Journal, Vol.15, pp.410-416, March 1977.

[22] Holst, T. L.,"Numerical Simulation of Axisymetric Boattail Flowfield with Plume Simulators," AIAA Paper No.77-224, Jan. 1977.

[23] Levy, L. L. Jr.,"An Experimental and Computational Investigation of the Steady and Unsteady Transonic Flow Field About an Airfoil in a Solid Wall Test Channel," AIAA Paper No.77-678, June 1977.

[24] Deiwert, G. S. and Bailey, H. E.,"Prospects for Computing Airfoil Aerodynamics with Reynolds Averaged Navier-Stokes Codes," NASA CP 2045, 1978

[25] Steger, J. L. and Bailey, H. E.,"Calculation of Transonic Aileron Buzz," AIAA Paper No.79-0134, Jan.1979.

[26] Hung, C. M. and Mac Cormack, R. W.,"Numerical Solution of Three-Dimensional Shock Wave and Turbulent Boundary Layer Interaction," AIAA Paper No.78-161, Jan 1978.

[27] Shang, J. S., Hankey, W. L. and Petty, J. S.,"Three-Dimensional Supersonic Interacting Turbulent Flow Along a Corner," AIAA Paper No.78-1210, July 1978.

[28] Pulliam, T. H. and Steger, J. L., "Implicit Finite-Difference Simulations of Three-Dimensional Compressible Flow," AIAA Paper 78-10, Jan. 1978. Also AIAA Journal, Vol. 18, No. 2, Feb. 1980, pp. 159-167.

[29] Baldwin, B. S. and Lomax, H., "Thin-Layer Approximation and Algebraic Model for Separated Turbulent Flows," AIAA Paper No.78-257, Jan. 1978.

[30] Cosner, R. R., "Relaxation Solution for Viscous Transonic Flow about Fighter Type Forebodies and Afterbodies," AIAA Paper 82-0252, Jan. 1982.

[31] Shang, J. S., "Numerical Simulation of Wing-Fuselage Aerodynamic Interaction," AIAA Paper 83-0225, Jan.1983.

[32] Hung, C. M. and Kordulla, W., "A Time-Split Finite-Volume Algorithm for Three-Dimensional Flow-Field Simulation," AIAA Paper 83-1957, July

1983.

[33] Purohit, S. C., Shang, J. S., and Hankey, W. L., "Effect of Suction on the Wake Structure of a Three-Dimensional Turret," AIAA Paper 83-1738, July 1983.

[34] Mansour, N. N., "Numerical Simulation of the Tip Vortex Off a Low-Aspect Ratio Wing at Transonic Speed," AIAA Paper 84-0522, Jan. 1984.

[35] Deiwert, G. S. and Rothmund, H., "Three-Dimensional Flow Over a Conical Afterbody Containing a Centered Propulsive Jet: A Numerical Simulation," AIAA Paper 83-1709, July 1983.

[36] Deiwert, G. S., Andrews, A. E., and Nakahashi, K., "Theoretical Analysis of Aircraft Afterbody Flow," AIAA Paper 84-1524, June 1984.

[37] Agarwal, R. K. and Deese, J. E., "Computation of Transonic Viscous Airfoil, Inlet, and Wing Flowfields," MDRL Report No. 84-29, June 1984, Also AIAA Paper 84-1551, June 1984.

[38] Chaussee, D. S., Buning, P. G., and Kirk, D. B., "Convair 990 Transonic Flow-Field Simulation About the Forward Fuselage," AIAA Paper 83-1785, July 1983.

[39] Fujii, K. and Kutler, P., "Numerical Simulation of the Viscous Flow Fields Over Three-Dimensional Complicated Geometries," AIAA Paper 84-1550, June 1984.

[40] Mehta, U. and Lomax, H.,"Reynolds Averaged Navier-Stokes computations of Transonic Flows, the-state-of-the-art," Chapter 6. Transonic Aerodynamics, Vol.81 of Progress in Astronautics and Aeronautics, D. Nixon ed., AIAA Inc., New York, 1982.

[41] Melnik, R. E.,"Turbulent Interactions on Airfoils at Transonic Speeds Recent Developments," AGARD CP-291, 1980.

[42] Steger, J. L. and Van Dalsem, W. R.,"Developments in the Simulation of Separated Flows Using Finite Difference Methods," Third Symposium on Numerical and Physical Aspects of Aerodynamic Flows, Long Beach, Jan. 1985.

[43] Wigton, L. and Yoshiara, H.,"Viscous-Inviscid Interactions with a Three-Dimensional Inverse Boundary Layer Code," Second Symposium on Numerical and Physical Aspects of Aerodynamic Flows, Long Beach, Jan.1983.

[44] Swafford, T. W.,"Time-Dependent Inverse Solution of Three-Dimensional, Compressible, Turbulent Integral Boundary Layer Equations in Nonorthogonal Curvilinear Coordinates," Ninth International Conference on Numerical Methods in Fluid Dynamics, Saclay, France, June 1984.

[45] Holst, T. L., Kaynak, U., Gundy, K. L., Thomas, S. D., Flores, J. and Chaderjian, N.,"Numerical Solution of Transonic Wing Flows Using an Euler /Navier-Stokes Zonal Approach," AIAA Paper No 85-1640 July 1985.

[46] Kline, S. J., Cantwell, B. J., and Lilley, G. M., eds., Proceedings, 1980-81 AFOSR-HTTM-Stanford Conference on Complex Turbulent Flows, Stanford, CA, 1982.

[47] Boppe, C. W.,"Computational Transonic Flow About Realistic Aircraft Configuration," AIAA Paper No.78-104, Jan.1978.

[48] Lee, K. D.,"3-D Transonic Flow Computations Using Grid Systems with Block Structure," AIAA Fifth Comp. Fluid Dyn. Conf.(1981)

[49] Lee, K. D. and Ruppert, P. E.,"Transonic Flow Computations Using Grid Sysytems with Block Structure," 7th International Conference on Numerical Methods in Fluid Dynamics. pp.266-271.

[50] Atta, E. H., "Component Adaptive Grid Interfacing," AIAA Paper No.81-0382, Jan. 1981.

[51] Atta, E. H. and Vadyak, J. A., "Grid Interfacing Zonal Algorithm for Three-Dimensional Transonic Flows about Aircraft Configurations," AIAA Paper No.82-1017, 1982.

[52] Benek, J. A., Steger, J. L., and Dougherty, F. C., "A Flexible Grid Embedding Technique with Application to the Euler Equations," AIAA Paper No.83-1944, July 1983.

[53] Hessenius, K. A. and Pulliam, T. H., "A Zonal Approach to Solution of the Euler Equations," AIAA Paper No.82-0969, June 1982.

[54] Rai, M. M., "A Conservative Treatment of Zonal Boundaries for Euler Equation Calculations," AIAA Paper No.84-0164, Jan. 1984.

[55] Hessenius, K. A. and Rai, M. M., "Applications of a Conservative Zonal Scheme to Transient and Geometrically Complex Problems," AIAA Paper No.84-1532, June 1984.

[56] Ruppert, P. E. and Lee, K. D.,"Patched Coordinate Sysytems," from Numerical Grid Generation, Joe Thompson ed., Elsevier Science Publishing Co., Inc., 1982, pp.235-294.

[57] Holst, T. L. and Thomas, S. D., "Numerical Solution of Transonic Wing Flowfields," AIAA Journal, Vol. 21, No. 6, June 1983, pp. 863-870.

[58] Rizzi, A., "Damped Euler-Equation Method to Compute Transonic Flow Around Wing-Body Combinations," AIAA Journal, Vol. 20, No. 10, Oct. 1982, pp. 1321-1328.

[59] Sorenson, R. L. and Steger, J. L., "Grid Generation in Three Dimensions by Poisson Equations with Control of Cell Size and Skewness at Boundary Surfaces," in Advances in Grid Generation-FED-Vol. 5, ed. K. N. Ghia.

[60] Edwards, T. A., "Noniterative Three-Dimensional Grid Generation Using Parabolic Partial Differential Equations," AIAA Paper No. 85-0485, Jan. 1985.

[61] Lockman, W. K. and Seegmiller, H. L., "An Experimental Investigation of the Subcritical and Supercritical Flow About a Swept Semispan Wing," NASA TM-84367, June 1983.

[62] Pulliam, T. H., "Euler and Thin-Layer Navier-Stokes Codes: ARC2D, and ARC3D," Notes for the Computational Fluid Dynamics Users' Workshop,

The University of Tennessee Space Institute, Tullahoma, Tenn., Mar. 12-16, 1984.

[63] Beam, R. and Warming, R. F., "An Implicit Finite-Difference Algorithm for Hyperbolic Systems in Conservation-Law Form," Journal of Comp. Physics, Vol.22, Sept. 1976, pp. 87-110.

[64] Pulliam, T. H. and Chaussee, D. S., "A Diagonal Form of an Implicit Approximate-Factorization Algorithm," Journal of Comp. Physics, Vol. 39, No. 2, Feb. 1981, pp. 347-363.

[65] Flores, J., "Convergence Acceleration for a Three-Dimensional Euler/Navier -Stokes Zonal Approach," AIAA Paper 85-1495, July 1985.

[66] Peyret, R, and Viviand, H.,"Computation of Viscous Compressible Flows Based on the Navier-Stokes Equations," AGARD-AG-212 ,1975.

[67] Steger, J. L. and Warming, R. F.,"Flux-Vector Splitting of the Inviscid Gas Dynamic Equations with Applications to Finite Difference Methods," Journal of Comp. Physics, 40(1981), pp. 263-293.

[68] Roe, P. L.,"The Use of Riemann Problem in Finite Difference Schemes," Presented at the Seventh International Conference on Numerical Methods in Fluid Dynamics," Stanford, CA, 1980.

[69] Van Leer, B.,"Flux-Vector Splitting for the Euler Equations," Eight International Conference on Numerical Methods in Fluid Dynamics, Lecture Notes in Physics, No.170, E. Krause ed., 1983.

[70] Osher, S. and Chakravarty, S.,"Upwind Schemes and Boundary Conditions with Applications to Euler Equations in General Geometries," Journal of Comp. Physics, 50(1983), 447-481.

[71] Harten, A.,"A High Resolution Scheme for the Computation of Weak Solutions of Hyperbolic Conservation Laws," Journal of Comp. Physics, 49(1983) pp.357-393.

[72] Pulliam, T. H."Artificial Dissipation Models for the Euler Equations," AIAA Paper No. 85-0438, Jan. 1985.

[73] Pulliam, T. H. and Steger, J. L.,"Recent Improvements in Efficiency, Accuracy and Convergence for Implicit Approximate Factorization Algorithms," AIAA Paper No. 85-0360, Jan. 1985.

[74] Anderson, D. A., Tannehill, J. C. and Pletcher, R. H.,"Computational Fluid Mechanics and Heat Transfer," Hemisphere Pub. Corp., 1985.

[75] Holst, T. L., Thomas, S. D., Kaynak, U., Gundy, K. L., Flores, J. and Chaderjian, N.,"Computational Aspects of Zonal Algorithms for Solving the Compressible Navier-Stokes Equations in Three Dimensions," International Symposium on Computational Fluid Dynamics, Tokyo, Japan, Sep. 9-12, 1985.

[76] Levin, D, and Katz, J., "Vortex-Lattice Method for the Calculation of the Nonsteady Separated Flows over Delta Wings," Journal of Aircraft, Vol.18, No. 12, Dec. 1981, pp. 1032-1037.

[77] Johnson, F. T., Tinocco, E. N., Lu, P., and Epton, M. A., "Recent Advances in the Solution of Three-Dimensional Flows over Wings with Leading Edge Separation," AIAA Paper No. 79-0282, Jan. 1979.

[78] Ericsson, L. E., and Rizzi, A., "Computation of Vortex Flow around Wings Using Euler Equations," Proceedings of the 4th GAMM Conference on Numerical Methods in Fluid Mechanics, Vieweg-Verlag, Paris, 1981.

[79] Hitzel, S. M. and Schmidt, W., "Slender Wings with Leading-Edge Vortex Separation - A Challange for Panel-Methods and Euler-Codes," AIAA Paper No. 83-0562, Jan. 1983.

[80] Krause, E., Shi, X. G., and Hartwich, P. W., "Computation of Leadind-Edge Vortices," AIAA Paper No. 83-1907, July 1983.

[81] Raj, P. and Sikore, J, S., "Free-Vortex Flows: Recent Encounters with an Euler Code," AIAA Paper No. 84-0135, Jan. 1984.

[82] Rizzi, A., "Mesh Influence on Vortex Shedding in Inviscid Flow Computations," Recent Contributions to Fluid Mechanics. W. Haase ed., Springer-Verlag, Berlin, 1982.

[83] Vigneron, Y. C., Rakich, J. V., and Tannehill, J. C., "Calculation of Supersonic Viscous Flow over Delta Wings with Sharp Subsonic Leading Edges," AIAA Paper No. 78-1137, July 1978.

[84] Vadyak. J., "Simulation of Wing, Fuselage, and Wing/Fuselage Flowfields Using a 3D Euler/Navier-Stokes Algorithm," AIAA Paper No. 85-1693, Cincinnati, Ohio, July 1985.

[85] Lighthill, M. J., "Attachment and Separation in Three-Dimensional Flow," Laminar Boundary Layers, ed. L. Rosenhead, pp. 72-82, Oxford University Press, 1963.

[86] Tobak, M. and Peake, D. J., "Topological Structures of Three-Dimensional Separated Flows," AIAA Paper No. 81-1260, Palo Alto, CA, June 1981.

[87] Maskell, E. C., "Flow Separation in Three Dimensions," RAE Aero. Rep. 2565, 1955.

[88] Legendre, R., "Séparation de l'Écoulement Laminaire Tridimensional," Recherche Aérospatiale, Vol. 54, 1956, pp. 3-8.

[89] Oswatitsch, K., "Die Ablönsungsbedindung von Grenzschichten, Grenzschicht Forschung" (H. Goertler, ed.), pp. 357-367 Springer-Verlag, Berlin and New York, 1958.

[90] Perry, A. E. and Fairlie, B. D., "Critical Points in Flow Patterns," Advances in Geophysics, Vol. 18B, pp. 299-315, Academic Press, 1974.

[91] Hornung, H. and Perry, A. E., "Some Aspects of Three-Dimensional Separation, Part I: Streamsurface Bifurcations", Z. Flugwiss. Weltraumforsch. 8(1984), Heft 2.

[92] Ladyzhenskaya, O. A., "Mathematical Analysis of Navier-Stokes Equations for Incompressible Liquids," Annual Review of Fluid Mechanics, 7(1975),

pp. 249-272.

[93] Kaplan, W., "Ordinary Differential Equations. Addison-Vesley, London, 1958.

[94] Dallmann, U. "Topological Structures of Three-Dimensional Vortex Flow Separation," AIAA Paper No 83-1735, July 1983, Danvers, Massachusetts.

[95] Thibert, J. J., Grandjacques, M., and Ohman, L. H., "NACA 0012 Airfoil, An Experimental Data Base for Computer Program Assessment," AGARD-AR-138, May 1979, pp. A1-1 to A1-19.

[96] Van Dalsem, W. R. and Steger, J. L., "Finite-Difference Simulation of Transonic Separated Flow Using a Full-Potential Boundary-Layer Interaction Approach," AIAA Paper 83-1689, July 1983.

[97] Jameson, A., Schmit, W. and Turkel, E., "Numerical Solutions of the Euler Equations by Finite Volume Methods Using Runge-Kutta Time-Stepping Schemes," AIAA Paper No. 81-1259, Palo Alto, CA, 1981.

[98] Andronov, A. A., Leontovich, E. A., Gordon, I. I., and Maier, A. G., "Theory of Bifurcations of Dynamic Systems on a Plane," NASA TT F-556, 1971.

[99] Hung., C. M., "Development of Relaxation Turbulence Models," NASA CR-2783, Dec. 1976.

[100] Rotta, J. C., "Turbulent Boundary Layers in Incompressible Flow," Progress in Aerospace Sciences, Vol. 2, p. 1, 1962.

[101] Shang, J. S. and Hankey, W. L., "Numerical Solution of the Navier-Stokes Equations for Compression Ramp," AIAA Paper No. 75-4, Pasadena, CA, Jan. 1975.

[102] Jameson, A. and Caughey, E. A., "Numerical Calculation of the Transonic Flow Past a Swept Wing," COO-3077-140, ERDA Nath. % Comput. Lab., New York U., June 1977(also, NASA CR-153297).

[103] Vanderplaats, Garret N., "CONMIN-A Fortran Program for Constrained Function Minimization," NASA TM X-626282, 1973.

[104] Hinson, B. L. and Burdges, K. P., "Acquisition and Application of Transonic Wing and Far-Field Test Data for Three-Dimensional Computational Method Evaluation, Vol. II. Appendix B, Experimental Data," Lockheed Georgia Company, AFOSR-TR-80-0422, 1980.

[105] Hinson, B. L. and Burdges, K. P.,"Acquisition and Application of Transonic Wing and Far-Field Test Data for Three-Dimensional Computational Method Evaluation,"Lockheed Georgia Company,AFOSR-TR-80-0421,1980.

[106] Hinson, B. L. and Burdges, K. P., "An evaluation of Three-Dimensional Transonic Codes Using New Correlation Test Data," AIAA Paper 80-0003, 1980.

[107] Keener, E. R., "Computational-Experimental Pressure Distributions on a Transonic, Low-Aspect-Ratio Wing," AIAA Paper No 84-2092, Aug. 1984, Seattle, Washington.

[108] Buning, G. P. and Steger, J. L. "Graphics and Flow Visualization in Computational Fluid Dynamics," AIAA Paper No 85-1507, July 1985, Cincinnati, Ohio.

1. Report No. NASA TM-88311	2. Government Accession No.	3. Recipient's Catalog No.
4. Title and Subtitle COMPUTATION OF TRANSONIC SEPARATED WING FLOWS USING AN EULER/NAVIER-STOKES ZONAL APPROACH		5. Report Date July 1986 6. Performing Organization Code
7. Author(s) Ünver Kaynak (Sterling Software, Palo Alto, CA), Terry L. Holst, and Brian J. Cantwell (Stanford University, Stanford, CA)		8. Performing Organization Report No. A-86271 10. Work Unit No.
9. Performing Organization Name and Address Ames Research Center Moffett Field, CA 94035		11. Contract or Grant No. 13. Type of Report and Period Covered Technical Memorandum
12. Sponsoring Agency Name and Address National Aeronautics and Space Administration Washington, D.C. 20546		14. Sponsoring Agency Code 505-60

15. Supplementary Notes

Point of Contact: Terry L. Holst, Ames Research Center, M/S 202A-14, Moffett Field, CA 94035 (415) 694-6032 or FTS 464-6032

16. Abstract

A computer program called Transonic Navier Stokes (TNS) has been developed which solves the Euler/Navier-Stokes equations around wings using a zonal grid approach. In the present zonal scheme, the physical domain of interest is divided into several subdomains called "zones" and the governing equations are solved interactively. The advantages of the Zonal Grid approach are as follows: 1) the grid for any subdomain can be generated easily, 2) grids can be, in a sense, adapted to the solution, 3) different equation sets can be used in different zones, and 4) this approach allows for a convenient data base organization scheme. Using this code, separated flows on a NACA 0012 section wing and on the NASA Ames WING C have been computed. First, the effects of turbulence and artificial dissipation models incorporated into the code are assessed by comparing the TNS results with other CFD codes and experiments. Then a series of flow cases are described where data are available. The computed results, including cases with shock-induced separation, are in good agreement with experimental data. Finally, some "futuristic" cases are presented to demonstrate the abilities of the code for massively separated cases which do not have experimental data.

17. Key Words (Suggested by Author(s))	18. Distribution Statement
Three-dimensional separated flows Flow topology Zonal methods Relaxation turbulence models	Unlimited Subject Category - 34

19. Security Classif. (of this report)	20. Security Classif. (of this page)	21. No. of Pages	22. Price*
Unclassified	Unclassified	153	A08

*For sale by the National Technical Information Service, Springfield, Virginia 22161